Traveltime Computation and Migration in Anisotropic Media

Dissertation
zur Erlangung des Doktorgrades
der Naturwissenschaften im Fachbereich
Geowissenschaften
der Universität Hamburg

vorgelegt von

Tina Kaschwich

aus
Rendsburg

Hamburg
2006

Als Dissertation angenommen vom Fachbereich Geowissenschaften der Universität
Hamburg

aufgrund der Gutachten von Professor Dr. Dirk Gajewski

und Dr. Ekkehart Tessmer

Hamburg, den 30. Januar 2007

Professor Dr. Kay-Christian Emeis
(Leiter des Departments Geowissenschaften)

Abstract

For seismic imaging of complex 3-D structures by e.g. prestack Kirchhoff depth migration large amounts of traveltime tables are required. This work provides a wavefront-oriented ray tracing technique for multi-valued traveltimes in smooth 3-D heterogeneous anisotropic media. In this method, wavefronts are propagated stepwise through the model and output quantities are interpolate (e.g., traveltimes, slowness) from rays to gridpoints. In contrast to isotropic media, where the input is a velocity model, the model for an anisotropic medium is defined by 21 elastic parameters at each gridpoint. To provide an efficient, accurate and fast algorithm for the interpolation of the elastic parameters to arbitrary points, the Cardinal Spline interpolation has been used, which produces an interpolated function that is continuous through the second derivative. The insertion of a new ray is performed by tracing it directly from the source (Coman, 2003). To calculate traveltimes at gridpoints a distance-weighted averaging method is used.

To demonstrate the accuracy of the method the traveltimes computed for a homogeneous anisotropic model with elliptical symmetry are compared to exact traveltimes available for this medium. Since it exists no analytical solution for an inhomogeneous anisotropic model, I compare the results with an alternative method for traveltime computation, the FD perturbation method (Soukina and Kashtan, 2001). To describe the subsurface models elastic parameters have been chosen that are related to real rocks.

Kirchhoff migration is an inversion technique that images the structure of the subsurface from seismic reflection data. Even if newer migration methods exist that can in some cases provide better images, Kirchhoff migration is still a standard technique. However, to obtain a high quality image even illumination of the subsurface is essential. Conventional Kirchhoff migration, however, does not provide the desired angular coverage at the image point, especially when complex media are considered. In this work I suggest a new strategy for migration with angular parametrisation in anisotropic media. The method, which guarantees even illumination, combines the conventional ray shooting with a hyperbolic traveltime interpolation. This makes the technique very efficient. For the application to the migration in the angular domain the hyperbolic traveltime interpolation is extended to an irregular grid.

To confirm the high potential of the new strategy, I present two synthetic data examples. First I apply the migration technique to a simple anisotropic model where elliptical symmetry is assumed. To show that the method can be applied to realistic data sets I also present a more complex isotropic model.

Zusammenfassung

Die vorliegende Dissertation ist mit Ausnahme dieser Zusammenfassung in englischer Sprache verfasst. Da die geophysikalische Fachterminolgie zu weiten Teilen aus dem Englischen kommt und zumeist nur schwer ein deutsches Äquivalent gefunden werden kann, wurde auf eine Übersetzung der Fachbegriffe verzichtet. Solche Begriffe sind im Folgenden durch "Hochkommata" hervorgehoben.

Einleitung

Im Bereich der Erdöl- und Erdgas Exploration ist das Prinzip der Migration ein weitverbreitetes und etabliertes Werkzeug, um ein realistisches Abbild vom Untergrund zu erhalten. Die Durchführung einer Migration verlangt zunächst ein Untergrundmodell, definiert durch seine elastischen Parameter. Wird ein Medium als isotrop angenommen, so reichen zur Beschreibung die Geschwindigkeiten der sich in diesem Medium ausbreitenden Wellen, Kompressionswelle und Scherwelle, und die Dichte des zugrundegelegten Materials aus. Im einfachsten Fall, dem homogenen Modell, sind die Geschwindigkeiten für alle Untergrundpunkte gleich. Weitaus realistischer ist allerdings die Annahme eines inhomogenen Untergrundes, d.h. von ortsabhängigen elastischen Parametern. Sobald die Ausbreitungsgeschwindigkeit der Welle richtungsabhängig ist, steigt die Anzahl der Parameter, die zur Beschreibung der elastischen Eigenschaften eines Untergrundpunktes notwendig sind. Das Medium wird dann als anisotrop bezeichnet und wird im allgemeinsten Fall mit 21 Parametern und der Dichte definiert.
Sowohl die Industrie als auch die Forschung hat sich lange Zeit auf isotrope Medien beschränkt, da neben der mathematischen Vereinfachung der Beschreibung der Wellenausbreitung auch der rechenzeitliche Aufwand und der damit verbundene Speicherbedarf in einem überschaubaren Rahmen blieben. Obwohl die Erde überwiegend anisotrop ist, konnten aufgrund der isotropen Modelle weite Teile der Erde befriedigend abgebildet werden, so dass die Lokalisierung grosser Rohstoffvorräte ausreichend genau gelang. Heutzutage sind die gesuchten "Targets" wesentlich kleinräumiger und die Anforderungen an die Genauigkeit der Modelle gestiegen. Eine wesentlich Rolle spielt in diesem Zusammenhang auch die stetig steigende Leistungsfähigkeit der Computer, die eine Berücksichtigung unterschiedlicher Komplexitäten möglich machen. Ein grundliegender Bestandteil der Migration ist die Bestimmung der "Green's" Funktionen, im Allgemeinen sind damit Laufzeiten

und Amplituden gemeint.
Die vorliegende Arbeit gliedert sich im Wesentlichen in zwei Teile: Im ersten Teil wird eine Methode, basierend auf dem Konzept der Wellenfrontenkonstruktion, zur Bestimmung von Laufzeiten in beliebig inhomogenen, anisotropen Medien präsentiert. Kernpunkt des zweiten Teils ist die Strategie einer winkelabhängigen, laufzeitbasierten Migration.

"Wavefront-oriented ray tracing"

Ausschliesslich für einfache Modelle gelingt es eine analytische Lösung der Wellengleichung zu bestimmen, und somit wurden im Laufe der Zeit zahlreiche mathematische Ansätze entwickelt. Zur Lösung der Wellengleichung unterscheidet man hauptsächlich "Finite Difference" und strahlen-basierte Methoden. Alle in dieser Arbeit verwendeten mathematischen Grundlagen beruhen auf dem zweiten Ansatz. Die Strahltheorie basiert auf einer sogenannten Hochfrequenz-Approximation der Wellengleichung. Wie jede Approximation unterliegt ihre Anwendbarkeit bestimmten Einschränkungen. Die einleitenden Kapitel dieser Arbeit beinhalten somit die Beschreibung der verwendeten mathematischen Formalismen und deren Gültigkeitsbereich. Neben dem theoretischem Aspekt gibt es für jedes Problem unterschiedliche praktische Strategien. In diesem Zusammenhang haben sich die sogenannten Wellenfrontenkonstruktionsmethoden als durchaus vorteilhaft erwiesen. Bei diesem Vorgehen werden die nach jedem diskreten Zeitschritt erreichten Strahlendpunkte bestimmt und definieren somit eine Wellenfront, sie beinhaltet also alle Punkte gleicher Laufzeit (siehe Abbildung 1).

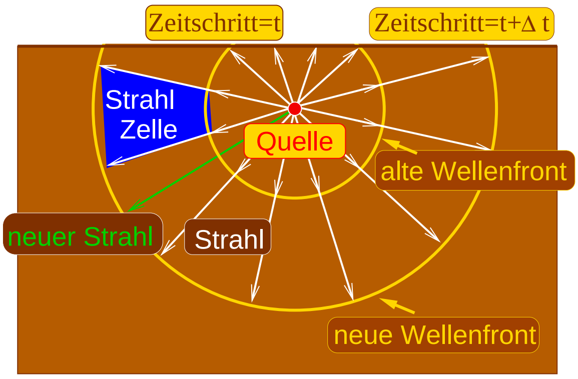

Figure 1: Das Wellenfrontenkonstruktions-Prinzip. Anstelle einzelner Strahlen, werden Wellenfronten mit einem bestimmten Zeitschritt durch das Medium propagiert. Hierbei wird nach jedem Zeitschritt die Laufzeit von der Wellenfront interpoliert. Falls die Strahldichte in dem Modell zu gering sein sollte, wird ein neuer Strahl eingefügt.

Ist die Strahldichte in einem Teil des Modelles nicht hoch genug, werden neue Strahlen eingefügt. Dies geschieht indem direkt an der Quelle ein neuer Strahl eingefügt und

propagiert wird.
Nach jedem Laufzeitschritt werden alle bestimmten Grössen auf das diskrete Untergrundmodellgitter mit Hilfe einer Interpolation übertragen. Ein solches Vorgehen hat eine Vielzahl an Vorteilen bezüglich der Rechenzeit und der Handhabung innerhalb der Implementation. Die Genauigkeit der vorgestellten Laufzeitberechnung wird durch eine Vielzahl von numerischen Beispielen, beginnend mit einfachen Modellen, bis hin zu komplexen inhomogenen Modellen demonstriert. Dabei werden zumeist aus Laborexperimenten bestimmte elastische Parameter natürlich vorkommender Stoffe verwendet.

Winkelabhängige, laufzeitbasierte Migration

Wie bereits oben angeführt werden Laufzeiten unter anderem während einer Migration benötigt. Auch in diesem Bereich gibt es die unterschiedlichsten Ansätze ein möglichst realistisches Abbild des Untergrundes zu bekommen. Der zweite Teil der Arbeit beinhaltet die grundlegenden Arbeiten zu einer winkelabhängigen Migration die mit Hilfe einer hyperbolischen Laufzeitinterpolation umgesetzt wurde.
Bei einer Migration betrachtet man jeden Untergrundpunkt als einen Diffraktionspunkt, die zugehörige Laufzeitkurven überlagern sich, folglich ergibt sich bei einer Stapelung an einigen Stellen eine konstruktive, an anderen eine destruktive Überlagerung. Üblicherweise wird hierbei eine gleichabständige Schuss- Empfängerkonfiguration auf der Oberfläche angenommen. Wie Abbildung 2 zeigt, kann dieses Vorgehen für komplexe Untergrundmodelle einen entscheidenden Nachteil haben: Eine gleichmässige Abdeckung an den Empfängern muss nicht zwangsläufig eine optimale Abdeckung am Untergrundpunkt bedeuten. Die gleichmässige Beleuchtung aller Untergrundpunkte ist allerdings für bestimmte Anwendungen, wie z.B. AVO Studien unerlässlich.

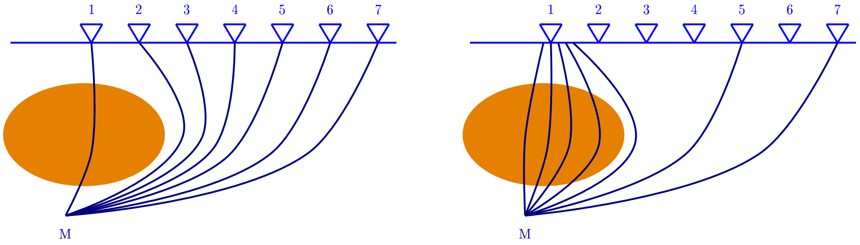

Figure 2: Beide Abbildungen zeigen ein homogenes Hintergrundmodell mit einer negativen Geschwindigkeitsanomalie im Zentrum. Die linke Seite zeigt die Situation für die klassische Kirchhoff Migration, die eine gleichmässige Abdeckung der an der Oberfläche positionierten Quell- Empfängerauslage bewirkt. Im Gegensatz dazu ist auf der rechte Seite das Prinzip der winkelabhängigen Migration dargestellt ist. Hier ist der einzelne Untergrundpunkt gleichmässig beleuchtet. (Adaptiert von Vanelle (2002a).)

Bei der in dieser Arbeit vorgestellten Strategie werden die Strahlen mit variierendem Winkelschritt am Untergrundpunkt startend durch das Medium propagiert. Um die Laufzeiten zu bestimmen, wurde die effektive und schnelle Methode des "ray shootings" verwendet. Bei einer solchen Vorgehensweise wird man in den wenigsten Fällen genau einen Empfänger an der Oberfläche treffen. Um nun die Laufzeit direkt am Geophone zu bestimmen, habe ich die hyperbolische Laufzeitformel im Hinblick auf diese Anwendung erweitert. Die Berechnung aller zugehörigen Koeffizienten ermöglicht zusätzlich die Interpolation neuer Untergrundpunkte und somit die Verdichtung des Migrationsgitters. Wird ein Empfänger von einem Untergrundpunkt nach erreichen des vorab definiertem minimalem Winkelinkrements nicht erreicht, wird dies Spur bei dem Aufstapelprozeß nicht berücksichtigt. Die abschliessenden synthetischen Datenbeispiele demonstrieren die Anwendbarkeit und das Potential dieser Strategie.

Contents

Acknowledgments

List of Figures

Notation

Variable[1]	**Meaning**
INDICES	
$i,\ j,\ k,\ l$	$= 1, 2, 3$
$I,\ J,\ K$	$= 1, 2, 3$
$p,\ q$	$= 1, 2$
m	index define type of wave
p	p-wave
s	s-wave
G	Geophone
S	Source
LATIN LOWERCASE	
a_{ijkl}	density-normalised elastic tensor
c_{ijkl}	elastic tensor
f_i	body force
$\vec{g}_m$	eigenvector of Christoffel matrix, polarisation vector
i_0	take-off angle
$\mathbf{i}$	
$\vec{n}$	normal vector
$\vec{p}$	slowness vector
$\vec{u}$	displacement
$\vec{v}$	ray velocity
$\vec{v}_p$	p-wave velocity
$\vec{v}_s$	s-wave velocity
$x,\ y,\ z$	Cartesian coordinates

---

[1] Names of variables are the same for all chapters. As far as possible, I tried to avoid using the same symbol with different meanings; in the few cases I failed to do so, the meaning of the variable is clear from the context.

LATIN UPPERCASE

A_{qp}	density-normalised elastic matrix
C_{qp}	elastic matrix
D_{ij}	
D	
G_m	eigenvalue of Christoffel matrix
$H_m(x_i, p_i)$	Hamilton function
K_i,L_i, M_i	Vector operator
U	amplitude vector
V_{ph}	phase velocity

GREEK

δ_{ij}	Kronecker's symbol
Γ_{kl}	Chrsitoffel matrix (Červený, 2001)
λ, μ	Lamé parameters
Λ_{ik}	Chrsitoffel matrix (Helbig, K. and Treitel, S., 1994)
ε_{kl}	strain
ε, δ and γ	Thomsen parameters
π	Ludolph's constant
ω	frequency
ρ	density
σ_{ij}	stress
ϕ_0	take-off angle
τ	traveltime

MISCELLANEOUS

$\bigtriangledown$	Laplacian operator
∂	partial derivative
$\frac{d}{dt}$	total differential

ABBREVIATIONS

AVA	amplitude variations with angle
AVO	amplitude variations with offset
FAM	factorised anisotropic medium
FD	finite-difference (method)
HF	high frequency (method)
KRT	Kinematic ray-tracing system

MVA	migration velocity analysis
PsDM	prestack depth migration
qP	quasi-compressional
qS	quasi-shear
TI	transversely isotropic

Chapter 1

Introduction

For seismic imaging of complex 3-D structures by e.g. prestack Kirchhoff depth migration large amounts of traveltime tables are required. This work provides an efficient technique for multi-valued traveltimes in smooth 3-D heterogeneous anisotropic media.
In a typical seismic experiment, the registration surface has an equidistant sampling. This line-up has, however, a vital disadvantage especially for complex subsurface structures: the usually equidistant spacing of source and receivers leads to high illumination in some angular regions, and poor illumination in others (see Figure 1.1).

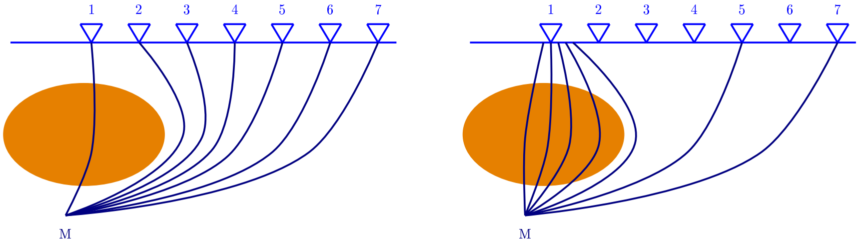

Figure 1.1: Both figures demonstrate a model with a negative velocity lens structure. The left hand side figure shows the principle of the conventional Kirchhoff migration, where the registration surface has an equidistant sampling, but there is no guarantee that this is also the case at the image point; the right figure shows the situation for the migration with angular parametrisation, where even illumination at the image point is ensured. (Adapted from Vanelle (2002a).)

In comparison to the standard Kirchhoff migration the migration in the angle domain has some relevant advantages, e.g. for AVO studies. For Kirchhoff migration, general ray shooting (two-point ray tracing) has to be performed for each source-receiver combination which leads to high computational effort. This large amount of traveltimes can be accomplished by the combination of the classical ray shooting with the hyperbolic traveltime interpolation (Vanelle, 2002a).

Three-dimensional prestack depth migration (PsDM) is certainly the most accurate approach for imaging laterally heterogeneous media. Because of the extensive CPU and memory requirements for 3-D seismic applications, most of the present 3-D PsDM algorithms are based on the ray theory (Kirchhoff migration). In fact, the ray theory provides an excellent compromise between precision and computational efficiency in 3-D heterogeneous media.

The main difficulty of ray-based migration is the computation of traveltimes in the target zone for all shot and receiver combinations. In this perspective, the "first arrival" methods such as the finite-differences solution of the eikonal equation (e.g. Reshef and Kosloff, 1986; Vidale, 1988) or shortest-path methods using graph theory (e.g. Saito, 1989; Moser, 1991) have been introduced. These methods provide extremely fast algorithms for kinematic migration (Reshef, 1991; Mufti et al., 1991). By using these methods traveltimes for a large number of source-receiver combinations can be calculated, but they are not able to compute later arrivals or to determine reliable amplitude coefficients. Since no reliable amplitude information is incorporated in this kinematic approach, migration-based amplitude variation with offset (AVO) analysis cannot be performed (Beydoun et al., 1993; Tura et al., 1997). Moreover, complex structure imaging is often unsuccessful when based only on first-arrival traveltimes. Traditionally, traveltime and amplitude calculations have been performed by ray tracing. Shooting or bending techniques may be used to find the ray path from a source point to a receiver (Julian and Gubbins, 1977). Červený (1985) proposed to shoot a fan of rays from the source and use paraxial extrapolation to estimate values at the receiver point.

Another family of ray-calculation techniques is ray-field propagation, where the whole wavefield is propagated rather than a single ray. These methods allow the insertion of new rays, when the ray field diverges at certain check positions. The ray field may be examined at constant depth (Lambaré et al., 1992), at interfaces (Åstebøl, 1994) or at wavefronts (Vinje et al., 1993a,b). These approaches are called wavefront construction and they are based on the classical ray theory as described by (Červený and Hron, 1980; Červený, 1985). Vinje et al. (1996) extend the wavefront construction to 3-D models with explicitly defined smooth interfaces (see Figure 1.2) .

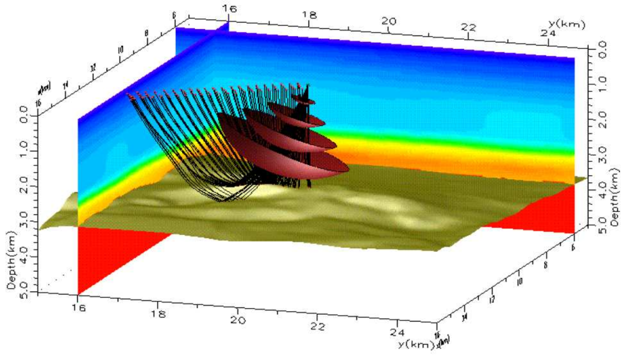

Figure 1.2: In the NORSAR-3D software, seismic ray modelling is done by the wavefront construction method. (Adapted from Laurain et al. (2003).)

Lambaré et al. (1996) have also postulated a new strategy to the wavefront construction. Coman (2003) introduced a new idea for the insertion of new rays and a distance-weighted traveltime interpolation. However, these implementations are mainly used for isotropic media.

In seismic imaging, much effort is spent on estimating the elastic parameters (P- and S-wave velocities) of an assumed isotropic subsurface for the construction of seismic images. Thomsen (1986) points out the inconsistency of these efforts when the subsurface is potentially anisotropic. Exploration geophysicists have studied velocity anisotropy for decades (e.g. Helbig, 1956), but within the past few years the relevance of the subjects for hydrocarbon exploration and development has become much more widely recognised. An understanding of anisotropy is important for hydrocarbon exploration because shales, which make up 75 % of the sedimentary cover of the hydrocarbon reservoirs, are in the majority of cases anisotropic. Hawkins et al. (2002) have confirmed the benefits of anisotropic prestack depth migration instead of using the isotropic case. They have presented a comparison between a reservoir imaged with isotropic and anisotropic depth imaging (see Figure 1.3). The reservoir is under an overburden that has been made complex by salt tectonics. On the anisotropic image, the Top and the Base Salt markers posted on the intersecting well bore show a salt thickness of just 21.4 metres, in good agreement with the seismic image. Those same markers are approximately 300 metres above the top of the isotropic image. Some vertical lines drawn at a fault close to the well illustrate that there is also lateral movement of about 75 metres between the two images. The effects of anisotropy on the kinematics of P-wave propagation and hence their effects on conventional seismic processing are summarised in Larner and Tsvankin (1995). In seismic shear wave data, anisotropy effects also have a significant influence on data interpretation

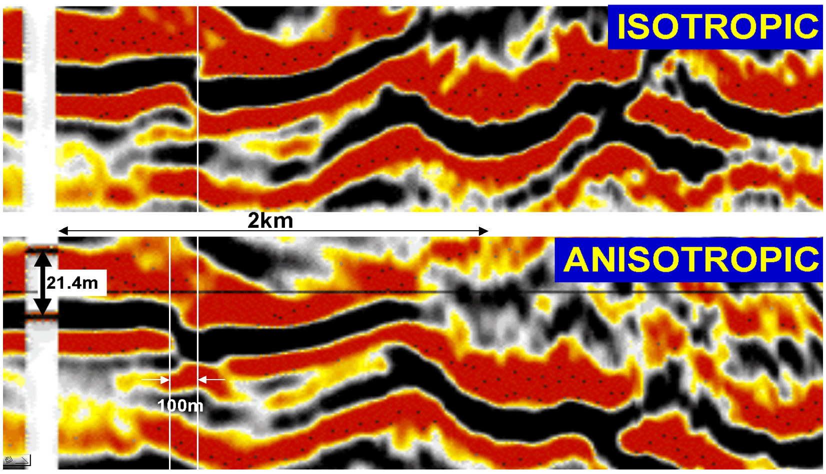

Figure 1.3: A reservoir comparison at a well location between isotropic and anisotropic depth imaging. The depth of Top and Base Salt is posted on the well bore on the anisotropic image illustrating a good tie. The depth of the two seismic depth images differ by approximately 300 metres while fault position appear to differ of about 75 metres. (Adapted from Hawkins et al. (2002).)

nearly everywhere (Winterstein, 1986). Therefore, an imaging algorithm, where also an anisotropic subsurface can be assumed, can significantly improve the image quality. One of the key issues is a sufficiently good technique for the traveltime calculation in such media. Gajewski and Pšenčik (1987) presented an algorithm for the computation of traveltimes, ray amplitudes and ray synthetic seismograms in 3-D laterally inhomogeneous media composed of isotropic or anisotropic layers. Alternative concepts of traveltime computation for anisotropic media have been developed, e.g. Ettrich and Gajewski (1998) presented a method by perturbation with FD-eikonal solver in weakly anisotropic media.

Common image gathers (CIGs) in the offset domain are used extensively in velocity analysis and AVO studies (Castagna and Backus, 1993). If the geology is complex and the ray field becomes multipathed, the quality of the CIGs deteriorates and hence makes it difficult to perform any form of AVO or velocity analysis. Such situations arise typically in seismic imaging beneath gas clouds, salt, and basalt. To overcome these problems, Brandsberg-Dahl et al. (2003) suggest to generate the CIGs as a function of the scattering angle and azimuth at the image point. Xu et al. (1998) propose a strategy providing individual common angle image gathers for complex media. In this work I suggest a traveltime-based migration in the angle domain. To get the traveltimes which are needed for the migration algorithm ray shooting is performed and then hyperbolic traveltime interpolation (Vanelle and Gajewski, 2002a) is used for the interpolation to the real receiver positions. Migration requires traveltimes on finely gridded traveltime tables. To reduces the effort in computational time as well as in data storage this approach is also used for the interpolation of sources.

Both concepts that I present in this work are based on the ray method. Therefore the opening Chapter 2 summarises the basic principles of the wave propagation in the high frequency limit, the asymptotic ray theory. All given mathematic formulas are valid for the anisotropic case. The chapter is mainly intended to recollect those foundations that are crucial for traveltime calculation but also for the presented migration algorithm.

Any medium can be described by the elastic parameters, which are related to the elastic behaviour of the material, and to the stratification of the subsurface. The types of anisotropy which are related to the number of independent elastic parameters are described in Chapter 3. Also the differences between a heterogeneous medium and an anisotropic medium will be clarified.

Chapter 4 is the key chapter of the first part that describes the wavefront-oriented ray tracing for anisotropic media. The interpolation of the input model is performed by using Cardinal splines, which is one of the main differences to the already implemented version for the isotropic case (Coman, 2003). This chapter describes also some accuracy tests of individual parts of the algorithm.

Some numerical examples are presented in Chapter 5. For the anisotropic case only a few materials can be used to calculate exact traveltimes. The elliptically anisotropic medium is used as a validation test and it follows a comparison of traveltimes calculated by the wavefront-oriented ray tracing and an alternative traveltime calculation method, i.e. a combination of finite differences eikonal solver with perturbation method (Soukina, 2004).

Chapter 6 is addressed to the introduction of the idea to combine the migration in the angle domain and the hyperbolic traveltime interpolation.

One of the key issues to any migration is an efficient method to calculate the traveltimes for a finely gridded subsurface. To accomplish this demand the hyperbolic traveltime interpolation is used. Therefore, Chapter 7 summarises the basic idea and the verification of the application of this method.

Numerical investigations are presented in Chapter 8, and it includes the comparison of conventional Kirchhoff migration and traveltime-based migration in the angle domain, but also the comparison of a standard traveltime calculation and the wavefront-oriented ray tracing method.

Finally, the results of the work are summarised in Chapter 9. The outlook in this final chapter is addressed to the extension of the traveltime-based migration in the angle domain to true amplitudes.

Appendix A comprises the introduction of the Hermite and the Cubic spline interpolation, which are the fundament of the Cardinal splines used for the interpolation of the elastic parameters for the wavefront-oriented ray tracing. To simplify the handling with the input quantities for the wavefront construction a graphical interface was developed (Appendix B). Appendix C summarises expressions for elliptical anisotropy for accuracy tests. All coefficients which are part of the hyperbolic traveltime equation for irregular grids are given in Appendix D.

Chapter 2

Ray theory

Seismic traveltimes are used in many processing techniques, such as Kirchhoff migration and traveltime tomography. There are two major approaches for the computation of traveltimes in anisotropic media: ray-tracing methods which are based on the ray theory (see e.g. Červený, 1972; Gajewski and Pšenčik, 1987) and methods which use a numerical solution of the eikonal equation by applying finite differences and perturbation (see e.g. Ettrich and Gajewski, 1998; Lecomte, 1993). The main criteria to compare these methods are the accuracy and the efficiency (Leidenfrost et al., 1999).

In this work we will concentrate on high-frequency asymptotic methods, such as ray methods. The high-frequency (HF) asymptotic methods are based on an asymptotic solution of the elastodynamic equation.

The aim of this chapter is to introduce the basic idea and the fundamental equations of the ray theory. For a detailed treatment of the ray theory see for example Červený (2001). Here, I only introduce the necessary terminology and those equations which are needed in this thesis. The Einstein summation convention is used throughout this work. Partial derivatives with respect to Cartesian coordinates or time are specified by a comma followed by the index of the coordinate or time, respectively.

Beginning with the stress-strain relation the mathematical background will shortly be introduced. In section 2.2 the eikonal equation will be derived assuming the high-frequency approximation of the elastodynamic equation. Solving the eikonal equation by the method of characteristics leads to the kinematic ray-tracing system which is introduced in section 2.3. Using the ray-tracing system the propagation of rays within a predefined model can be determined (see Figure 2.1).

Section 2.6 employs the initial condition for the ray-tracing system for an inhomogeneous anisotropic medium. A general description of the phenomenon of anisotropy will be given in chapter 3.

The given formulas are valid for anisotropic media. This includes isotropic models which are only a simplified case. Thus, also the mathematics for the isotropic case, like e.g. the formula of the kinematic ray-tracing system, are simplified (see section 2.4).

In section 2.5 the phase and the group velocities are explained by their physical meaning for the ray theory.

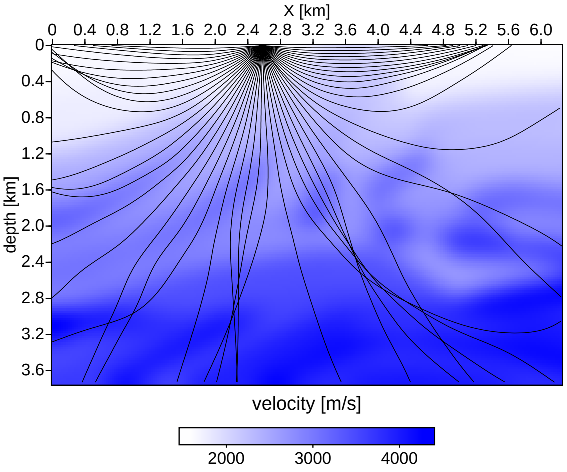

Figure 2.1: Principle of ray tracing: to propagate a single ray the kinematic ray-tracing system must be solved for this ray, thus the initial conditions at the source must be known.

2.1 Stress-strain relation

Consider an anisotropic perfectly elastic inhomogeneous medium described by the elastic tensor c_{ijkl}, the constitutive stress-strain relation is given by the generalised Hooke's law,

$$\sigma_{ij} = c_{ijkl}\epsilon_{kl}. \tag{2.1}$$

Here, σ_{ij} are the Cartesian components of the stress tensor and the strain tensor is denoted by ϵ_{kl}. Both tensors are symmetric:

$$\sigma_{ij} = \sigma_{ji} \qquad \epsilon_{kl} = \epsilon_{lk}. \tag{2.2}$$

These symmetries reduce the number of significant components of the elastic tensor c_{ijkl} to a maximum of 36,

$$c_{ijkl} = c_{jikl} \quad c_{ijkl} = c_{ijlk}, \tag{2.3}$$

in accordance with the fact that both stress and strain tensor have only six significant components. The symmetries of the tensors on both sides of Hooke's law (2.1) additionally reduce the number of independent parameters to 21. The components of the elastic tensor are also called elastic constants, elastic moduli, elastic parameters, or stiffnesses. The strain tensor ϵ_{kl} is defined in terms of the displacement vector $\vec{u}$:

$$\epsilon_{kl} = \frac{1}{2}(u_{k,l} + u_{l,k}). \tag{2.4}$$

The symmetry relations (2.3) lead to the following expression of Hook's law (2.1):

$$\sigma_{ij} = c_{ijkl}u_{k,l}. \tag{2.5}$$

The eikonal equation is the basis of calculating traveltimes with a high frequency approximation. The basic concepts and equations of linear elastodynamics have been explained in many textbooks and papers. Therefore, in the next section we introduce only certain important equations.

2.2 Elastodynamic and eikonal equation

The elastodynamic equation relates the spatial variations of the stress tensor with the time variations of the displacement vector $\vec{u}$:

$$\sigma_{ij,j} + f_i = \rho u_{i,tt}, \qquad i = 1, 2, 3, \tag{2.6}$$

where t is the time, f_i the Cartesian components of the body forces and ρ denotes the density. The insertion of (2.5) in (2.6) leads to

$$(c_{jikl} u_{k,l})_{,j} + f_i = \rho u_{i,tt}, \qquad i = 1, 2, 3. \tag{2.7}$$

The elastodynamic equation (2.7) represents a system of three coupled partial differential equations of second order for the Cartesian components $u_i(x_j, t)$ of the displacement vector $\vec{u}$.

Analytical solutions of the elastodynamic equation exist only for very simple models. Therefore, a high frequency (HF) approximation is applied for 3-D complex models. The zero-order HF solution of the elastodynamic equation in the case of harmonic waves reads (Červený, 2001):

$$\vec{u}(\vec{x}, t) = \vec{U}(\vec{x}) e^{\mathbf{i}\omega(t-\tau(\vec{x}))}, \tag{2.8}$$

where $\vec{U}$ denotes the vectorial amplitude, and the eikonal is defined by τ. Here, $\vec{U}$ and τ are only functions of $\vec{x}$, thus we have a separation of space and time. Synonyms for eikonal are phase function and traveltime. It describes the time which a body wave needs for its propagation from one point to another, e.g. the source and receiver location.

The HF approximation is valid in media in which the characteristic dimensions of all inhomogeneities (e.g. the variations of elastic parameters) are larger than the prevailing wavelength of the propagating wave. Thus, in the isotropic case the velocity model has to be smoothed (see section 4.3). The insertion of (2.8) into the elastodynamic equation (2.7) without body forces ($f_i = 0$) leads to

$$(\mathbf{i}\omega)^2 K_i(\vec{U}) + (\mathbf{i}\omega) M_i(\vec{U}) + L_i(\vec{U}) = 0. \tag{2.9}$$

The operators K_i, M_i and L_i are given by the relations (Červený, 2001):

$$\begin{aligned} K_i(\vec{U}) &= \Gamma_{ik} U_k - U_i, \\ M_i(\vec{U}) &= a_{ijkl} p_j U_{k,l} + \rho^{-1}(\rho a_{ijkl} p_l U_k)_{,j}, \\ L_i(\vec{U}) &= \rho^{-1}(\rho a_{ijkl} U_{k,l})_{,j}, \end{aligned} \tag{2.10}$$

where $a_{ijkl} = c_{ijkl}\rho^{-1}$ is the density normalised elastic tensor and the Christoffel matrix (Červený, 2001) is:

$$\Gamma_{ik} = a_{ijkl} p_j p_l. \tag{2.11}$$

Sometimes, however, the term Christoffel matrix is associated with the matrix $\Lambda_{ik} = c_{ijkl} n_j n_l$ (see e.g. Helbig, K. and Treitel, S., 1994). The matrix (2.11) is symmetrical and positive definite. The slowness vector p_j is defined as:

$$p_j = \tau_{,j}, \tag{2.12}$$

so that the slowness vector is always normal to the wavefront (see also section 2.5). To obtain $\tau(x_i)$ and $U(x_i)$ independent of the frequency, equation (2.9) is solved as follows:

$$K_i(\vec{U}) = 0, \tag{2.13}$$

$$M_i(\vec{U}) = 0. \tag{2.14}$$

This is the basic system of equations of the ray method. By applying high frequencies ($\omega \to \infty$) in equation (2.9) the term $L_i(\vec{U})$ is negligibly small:

$$(\mathbf{i}\omega)^2 K_i(\vec{U}) \gg L_i(\vec{U}) \quad \text{and} \quad (\mathbf{i}\omega) M_i(\vec{U}) \gg L_i(\vec{U}). \tag{2.15}$$

Equation (2.13) will be used to determine the traveltime function $\tau(x_i)$ and the polarisation of the amplitude vector U_i, whereas equation (2.14) can be used to solve the amplitude function. Equation (2.13) is an eigenvalue problem:

$$(\Gamma_{ik} - G_m \delta_{ik}) U_k = 0, \quad m = 1, 2, 3, \tag{2.16}$$

where δ_{ik} is the Kronecker symbol,

$$\delta_{ij} = 1 \;\text{ for }\; i = j, \qquad \delta_{ij} = 0 \;\text{ for }\; i \neq j. \tag{2.17}$$

In an anisotropic homogeneous medium three types of waves can propagate: one quasi-compressional (qP) wave and two quasi-shear (qS1 and qS2) waves. In general, these three types have different properties, particularly different velocities of propagating. The Christoffel equation (2.11) has three eigenvalues $G_m(x_i, p_i)$, $m = 1, 2, 3$, and the associated eigenvectors $\vec{g}^{(m)}(x_i, p_i)$. The eigenvalues correspond to the three seismic body waves (qP, qS1 and qS2) which propagate in an inhomogeneous anisotropic medium in a specified direction. In general, the eigenvalues are different:

$$G_1(x_i, p_i) \neq G_2(x_i, p_i) \neq G_3(x_i, p_i). \tag{2.18}$$

The traveltime field for all three waves satisfies the nonlinear partial differential equation of the first order

$$G_m(x_i, p_i) = 1, \quad m = 1, 2, 3. \tag{2.19}$$

Equation (2.19) is the eikonal equation. Conventionally, $m = 1$ denotes the qS1-wave, $m = 2$ the qS2-wave, and $m = 3$ the qP-wave. The eigenvalues G_m can be expressed in terms of the Christoffel matrix Γ_{ik}:

$$G_m = \Gamma_{ik} g_i^{(m)} g_k^{(m)} = a_{ijkl} p_j p_l g_i^{(m)} g_k^{(m)}, \tag{2.20}$$

(no summation over m). The direction of propagation of the wavefront is defined by the unit normal n_i. Putting

$$p_i = \frac{n_i}{V^{(m)}} \tag{2.21}$$

for the m-th wave ($m = 1$ or 2 or 3) and inserting it into (2.20) yields the phase velocity $V^{(m)}$

$$V^{(m)^2} = G_m(x_i, n_i). \tag{2.22}$$

The eigenvectors $\vec{g}^{(m)}(x_i, p_i)$ determine the polarisation of the individual waves so that they can be referred to as polarisation vectors. The components of the eigenvector $g_i^{(m)}$ can be obtained as the solution of equation

$$(\Gamma_{ik} - G_m \delta_{ik}) g_k^{(m)} = 0, \quad g_k^{(m)} g_k^{(m)} = 1, \tag{2.23}$$

(no summation over m).

2.3 Kinematic ray-tracing system

The ray-tracing system will be derived from the eikonal equation in Hamiltonian form,

$$H_m(x_i, p_i) = \frac{1}{2}(G_m(x_i, p_i) - 1) = 0 \quad m = 1, 2, 3, \tag{2.24}$$

using the method of characteristics. The derived ray-tracing system reads:

$$\frac{\mathrm{d}x_i}{\mathrm{d}\tau} = \frac{1}{2}\frac{\partial G_m}{\partial p_i}, \qquad \frac{\mathrm{d}p_i}{\mathrm{d}\tau} = -\frac{1}{2}\frac{\partial G_m}{\partial x_i}. \tag{2.25}$$

Analytical expressions for $g_i^{(m)}$ and their products are:

$$g_j^{(m)} g_k^{(m)} = D_{jk}^{(m)}/D, \tag{2.26}$$

where D_{jk} and D are given by the relations

$$\begin{aligned}
D_{11} &= (\Gamma_{22} - 1)(\Gamma_{33} - 1) - \Gamma_{23}^2, \\
D_{22} &= (\Gamma_{11} - 1)(\Gamma_{33} - 1) - \Gamma_{13}^2, \\
D_{33} &= (\Gamma_{11} - 1)(\Gamma_{22} - 1) - \Gamma_{12}^2, \\
D_{12} = D_{21} &= \Gamma_{13}\Gamma_{23} - \Gamma_{12}(\Gamma_{33} - 1), \\
D_{13} = D_{31} &= \Gamma_{12}\Gamma_{23} - \Gamma_{13}(\Gamma_{22} - 1), \\
D_{23} = D_{32} &= \Gamma_{12}\Gamma_{13} - \Gamma_{23}(\Gamma_{11} - 1), \\
D &= D_{11} + D_{22} + D_{33}.
\end{aligned} \tag{2.27}$$

For the sake of clarity the index m has been omitted. The insertion of equation (2.26) in the ray-tracing system (2.25) leads to:

$$
\begin{aligned}
\frac{\mathrm{d}x_i}{\mathrm{d}\tau} &= a_{ijkl}p_l D_{jk}/D, \\
\frac{\mathrm{d}p_i}{\mathrm{d}\tau} &= -\frac{1}{2}\frac{\partial a_{jkln}}{\partial x_i}p_k p_n D_{jl}/D.
\end{aligned}
\tag{2.28}
$$

Solving these six ordinary differential equations of first order yields the ray trajectory $x_i + x_i(\Delta\tau)$ and the components of the slowness vector at each point of the ray $p_i + p_i(\Delta\tau)$. If condition (2.18) is not satisfied the ray tracing system (2.25) may fail, because the relevant eigenvectors $\vec{g}^{(1)}$ and $\vec{g}^{(2)}$ cannot be determined. In the same way, the ray tracing system (2.28) fails, as in this case D_{jk}/D is an indefinite expression of the type 0/0. Červený (2001) suggested possible ways to overcome these complications. Techniques to determine the numerical solution of (2.28) are presented in section 4.4.

2.4 The isotropic case

If isotropic media are considered, the formulas given in the previous section are much simpler than in the anisotropic case. Two of the eigenvalues G_m are equal, and we have only two types of waves, one compressional and one shear wave. The corresponding eigenvalues are:

$$
G_1 = G_2 = v_s^2 \tau_{,i}\tau_{,i}, \qquad G_3 = v_p^2 \tau_{,i}\tau_{,i}, \tag{2.29}
$$

where v_s is the shear wave velocity and v_p the velocity of the compressional wave. Because of $G_m = 1$, the eikonal equation for the isotropic case reads:

$$
p_i p_i = \frac{1}{v^2}, \tag{2.30}
$$

where v is either v_p or v_s. The method of characteristics also leads to a ray-tracing system for isotropic media:

$$
\begin{aligned}
\frac{\mathrm{d}x_i}{\mathrm{d}\tau} &= v^2 p_i, \\
\frac{\mathrm{d}p_i}{\mathrm{d}\tau} &= -\frac{v_{,i}}{v}.
\end{aligned}
\tag{2.31}
$$

In the isotropic case the velocity is independent of direction and we have only one velocity value v ($v = v_p$ or $v = v_s$) at the source for each type of wave, so the slowness is defined by the two take-off angles i_0 and ϕ_0:

$$
p_{10} = \frac{1}{v}\sin i_0 \cos\phi_0, \quad p_{20} = \frac{1}{v}\sin i_0 \sin\phi_0, \quad p_{30} = \frac{1}{v}\cos i_0. \tag{2.32}
$$

2.5 Phase and group velocity

For a better understanding of the effects of anisotropy, the different types of velocities will be discussed in this section. The phase velocity V represents the velocity of propagation of the wavefront in the direction perpendicular to it:

$$\text{components of the phase velocity:} \quad V_i = n_i \, V. \tag{2.33}$$

Because of relation

$$V_i = \frac{p_i}{p_k p_k}, \tag{2.34}$$

and the fact that the slowness vector $\vec{p}$ is always perpendicular to the wavefront, the phase velocity vector is orthogonal to the tangent of the wavefront (see also Figure 2.2).

$$\text{phase velocity:} \quad V = \sqrt{V_k V_k} = \frac{1}{\sqrt{p_k p_k}}. \tag{2.35}$$

The velocity vector of the energy flux is called the group velocity vector and is denoted by v_i. It is given by the relation:

$$v_i = \frac{\mathrm{d}x_i}{\mathrm{d}\tau} = a_{ijkl} p_l g_j^{(m)} g_k^{(m)} = a_{ijkl} p_l \frac{D_{jk}^{(m)}}{D}. \tag{2.36}$$

In anisotropic media the direction of the group velocity (also denoted ray velocity) does not coincide with slowness direction, consequently not with the direction of the phase velocity. In other words, in anisotropic media, the energy of waves does not propagate perpendicular to the wavefront.
Figure (2.2) schematically shows a wavefront and the corresponding velocities.

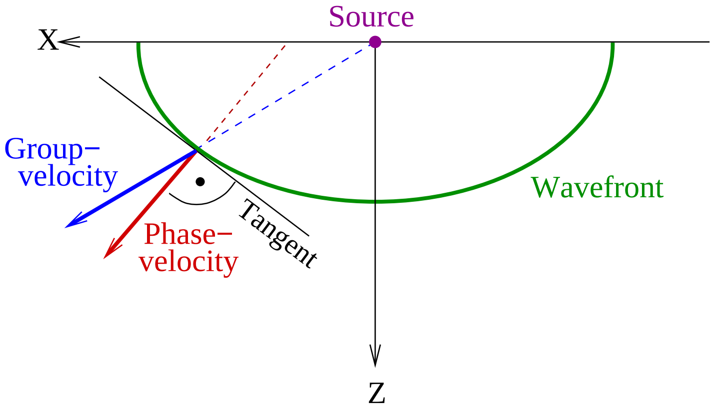

Figure 2.2: Difference between the phase velocity vector V_i and the group velocity vector v_i.

Both the phase and group velocities of plane waves in a homogeneous anisotropic medium depend on the direction of propagation of the wavefront $\vec{n}$. In isotropic media, the phase and group velocities of a propagating wave not only coincide but are independent on the direction of wave propagation.

2.6 Initial conditions

The ray-tracing system (2.28) is identical for all three types of waves. Therefore the type of wave whose ray is to be computed must be specified by initial conditions. The initial conditions in anisotropic media specify not only the initial point and the initial direction of the ray, but also the type of wave that is to be computed. The initial conditions for a single ray of one particular selected wave type passing through a point S can be expressed by defining the initial direction of slowness vector $\vec{p}$ at S, and not the initial direction of the ray (see section 2.5).
The initial conditions for the ray-tracing system (2.28) are

$$\text{at } S: \quad x_i = x_{i0}, \quad p_i = p_{i0}, \tag{2.37}$$

where p_{i0} satisfies the eikonal equation at S,

$$G_m(x_{i0}, p_{i0}) = 1, \tag{2.38}$$

corresponding to the wave type to be computed ($m = 1, 2, 3$).
The components of the phase normal vector $\vec{n_0}$ are defined by the two take-off angles, i_0 and ϕ_0 at the source:

$$n_{10} = \sin i_0 \cos\phi_0, \qquad n_{20} = \sin i_0 \sin\phi_0, \qquad n_{30} = \cos i_0. \tag{2.39}$$

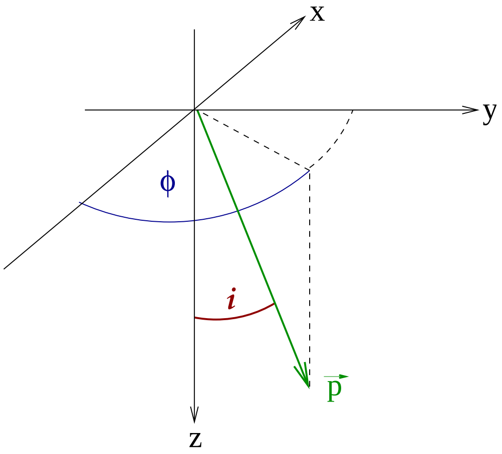

Figure 2.3: Slowness vector and angles in the Cartesian coordinate system. The angle i is the azimuth and ϕ the polar angle.

The components of the slowness vector $\vec{p}^{(m)}$ at S are given by:

$$p_{10} = n_{10}/V_0^{(m)}, \qquad p_{20} = n_{20}/V_0^{(m)}, \qquad p_{30} = n_{30}/V_0^{(m)}. \tag{2.40}$$

Here, V_0 denotes the phase velocity V at the point S for direction $\vec{n}_0$ and for wave type m. Solving the eigenvalue problem leads to the phase velocity at the source $V_0^{(m)}$:

$$V_0^{(m)} = \sqrt{a_{ijkl} n_j n_l g_i^{(m)} g_k^{(m)}} \text{ at S}, \tag{2.41}$$

(no summation over m). Afterwards the components of the slowness vector (2.40) at S can be calculated.

2.7 Caustics

A “caustic point” is defined where the cross-sectional area of the ray tube shrinks to zero. By introducing the ray coordinates γ_1, γ_2 and γ_3, Červený (2001) understands by “ray tube” the family of rays, where the parameters are within $(\gamma_1,\gamma_1+\Delta\gamma_1)$ and $(\gamma_2,\gamma_2+\Delta\gamma_2)$, see Figure 2.4.
The ray approximation to the wavefield undergoes a phase shift when the ray crosses a caustic. The cumulative number of such phase shifts along a ray is called the KMAH index (Červený, 2001). The sign of these phase shifts depends on the sign of the angular frequency in combination with the sign convention used for the Fourier transformation. The phase shift due to caustics along the ray from the source S to the receiver G is

$$T^c(G,S) = \pm\frac{\pi}{2}k(G,S), \tag{2.42}$$

where $k(G,S)$ denotes the KMAH index. Along a ray two types of caustic points can exist. At a caustic point of the first order, a line focus, where the ray tube shrinks to an elementary arc perpendicular to the direction of propagation (see Figure 2.5, left). At a caustic point of second order, also called point focus, the ray tube shrinks to a point (see Figure 2.5, right) .

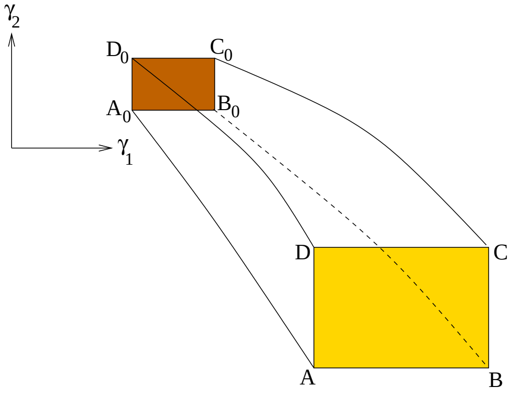

Figure 2.4: Ray tube. Ray A_0A corresponds to the ray parameter γ_1 and γ_2, ray B_0B is associated to $\gamma_1+\Delta\gamma_1$ and γ_2, ray B_0B corresponds to $\gamma_1+\Delta\gamma_1$ and $\gamma_2+\Delta\gamma_2$ and ray D_0D is associated to γ_1 and $\gamma_2+\Delta\gamma_2$.

The KMAH index changes by 1 when a ray passes through a caustic point of the first order (T^c is $\pm\pi/2$) and by 2 when it passes through a caustic point of the second order (T^c is $\pm\pi$).

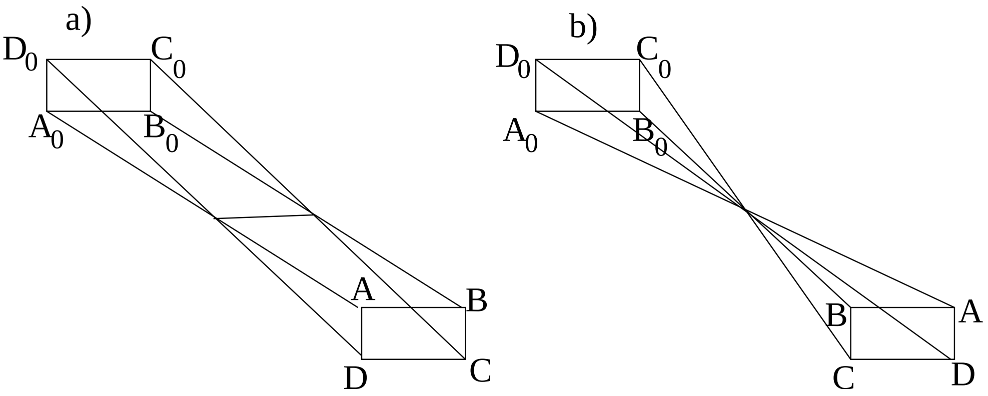

Figure 2.5: Two types of caustic points along a ray. (a) At a caustic point of first order, the ray tube shrinks into an elementary arc, perpendicular to the direction of propagation. (b) At a caustic point of second order the ray tube shrinks to a point.

Chapter 3

Anisotropy and real rocks

This chapter deals with causes for seismic anisotropy and gives an overview over types of symmetry of the elastic parameters. A medium is called anisotropic, when the variation of a physical property at a spatial position is dependent on the direction in which it is measured. If an elastic medium is anisotropic, seismic waves of a given type propagate in different directions with different velocities. By contrast, heterogeneity is defined to be the dependence of physical properties upon position. Both, anisotropy and heterogeneity are matters of scale, and so their usage is related to the wavelengths involved. The same medium may behave heterogeneously for small wavelengths and anisotropically for large wavelengths (Helbig, K. and Treitel, S., 1994).

Elastic anisotropy is a very common phenomenon in the Earth's interior. It is caused by the following mechanisms or a combination of them (see e.g. Thomsen, 2002; Červený, 2001):

- **Preferred orientation of crystals.** Single crystals of rock-forming minerals are intrinsically anisotropic (see left side in Figure 3.1).

- **Anisotropy due to aligned inclusions.** The presence of aligned inclusions (such as cracks, pores, or impurities) can cause effective anisotropy of rocks, if observed at long wavelengths.

- **Anisotropy due to sequences of thin layers.** Sequences of isotropic layers of different properties are very common in the Earth' interior, at least in the upper crust. If the prevailing wavelength of the wave under consideration is larger than the thickness of the individual layer, the sequences of thin layers behave anisotropically (see right picture in Figure 3.1).

It is common to obtain an anisotropy produced by a certain combination of these factors. For example, a system of vertical fractures may have developed in finely layered sediments, or the thin layers themselves may be intrinsically anisotropic. As a result, subsurface formations may possess several types of anisotropy, each with a different character of wave propagation.

Figure 3.1: Examples for anisotropy in real rocks. Left: Olivine, anisotropy caused by preferred orientation of crystals; Right: Thin-bed layered structure.

Section 3.2 introduces the major types of anisotropic symmetries. To determine the elastic parameters from observed seismograms an inversion procedure is necessary. For instance, Soukina (2004) suggests an inversion technique for weak anisotropy by using a perturbation method.

3.1 Representation of the model

The number of independent components of the elastic tensor for an arbitrary anisotropic medium can be reduce from 81 to 21. To take this reduction of components into account an anisotropic medium will in praxis be described by a symmetric 6 × 6 matrix C_{pq} (Voigt notation). The transformation from the i, j, k, l to the contracted p, q is represented according to the following scheme (see e.g. Helbig, K. and Treitel, S., 1994):

$$\begin{array}{rcllllll} ij\ (\text{or}\, kl) & = & 11 & 22 & 33 & 23{,}32 & 13{,}31 & 12{,}21 \\ p\ (\text{or}\, q) & = & 1 & 2 & 3 & 4 & 5 & 6 \end{array}$$

To leave the stress tensor as originally defined, we get the following relations for the stress and the strain tensor:

$$\sigma_p = \sigma_{ij}, \quad \text{but} \quad \epsilon_q = (2 - \delta_{kl})\epsilon_{kl}. \tag{3.1}$$

By using the 6 × 6 matrix C_{pq} instead of the elastic tensor c_{ijkl} Hooke's law (2.1) is expressed by:

$$\begin{pmatrix} \sigma_{11} \\ \sigma_{22} \\ \sigma_{33} \\ \sigma_{23} \\ \sigma_{13} \\ \sigma_{12} \end{pmatrix} = \begin{pmatrix} \sigma_1 \\ \sigma_2 \\ \sigma_3 \\ \sigma_4 \\ \sigma_5 \\ \sigma_6 \end{pmatrix} = \begin{pmatrix} C_{11} & C_{12} & C_{13} & C_{14} & C_{15} & C_{16} \\ C_{21} & C_{22} & C_{23} & C_{24} & C_{25} & C_{26} \\ C_{31} & C_{32} & C_{33} & C_{34} & C_{35} & C_{36} \\ C_{41} & C_{42} & C_{43} & C_{44} & C_{45} & C_{46} \\ C_{51} & C_{52} & C_{53} & C_{54} & C_{55} & C_{56} \\ C_{61} & C_{62} & C_{63} & C_{64} & C_{65} & C_{66} \end{pmatrix} \begin{pmatrix} \epsilon_{11} \\ \epsilon_{22} \\ \epsilon_{33} \\ 2\epsilon_{23} \\ 2\epsilon_{13} \\ 2\epsilon_{12} \end{pmatrix}. \tag{3.2}$$

The 6×6 matrix is not a tensor. This transformation is immensely useful, because it allows the notation of an actual $3 \times 3 \times 3 \times 3$ tensor in a 2-D matrix-form. The elastic matrix C_{pq} is symmetrical, $C_{pq} = C_{qp}$. Therefore in the next section the elements below the diagonal ($p > q$) are not shown. The diagonal elements in the table are always positive for a solid medium, but the off-diagonal elements may be arbitrary (positive, zero or negative).

3.2 Types of symmetry

For an arbitrary anisotropic medium the elastic matrix C_{pq} comprises 21 independent constants. Usually the number is much less than this, because of additional restrictions, e.g. imposed by the microscopic nature of the medium. Each anisotropy symmetry is characterised by a specific structure of the stiffness matrix with the number of independent elements decreasing for higher-symmetry systems. In the following section the different types of symmetry are presented.

3.2.1 Triclinic medium

The most general form of anisotropy is the triclinic medium. It is described by up to 21 independent elastic parameters:

$$C_{pq} = \begin{pmatrix} C_{11} & C_{12} & C_{13} & C_{14} & C_{15} & C_{16} \\ & C_{22} & C_{23} & C_{24} & C_{25} & C_{26} \\ & & C_{33} & C_{34} & C_{35} & C_{36} \\ & & & C_{44} & C_{45} & C_{46} \\ & & & & C_{55} & C_{56} \\ & & & & & C_{66} \end{pmatrix}. \tag{3.3}$$

Mensch and Rasolofosaon (1997) provide the elastic elements for e.g. a triclinic sandstone from core/lab-measurement. But obtaining all 21 elastic parameters by a seismic experiment will continue be difficult.

3.2.2 Monoclinic medium

The lowest-symmetry model identified from seismic measurements is monoclinic (Winterstein and Meadows, 1991) which has 13 independent stiffness coefficients. In contrast to triclinic models, monoclinic media have a plane of mirror symmetry with the spatial orientation defined by the underlying physical model. For instance, Figure 3.2 shows a formation which contains two different non-orthogonal systems of small-scale vertical fractures embedded in an isotropic background. Here, the effective medium becomes monoclinic with a horizontal symmetry plane.

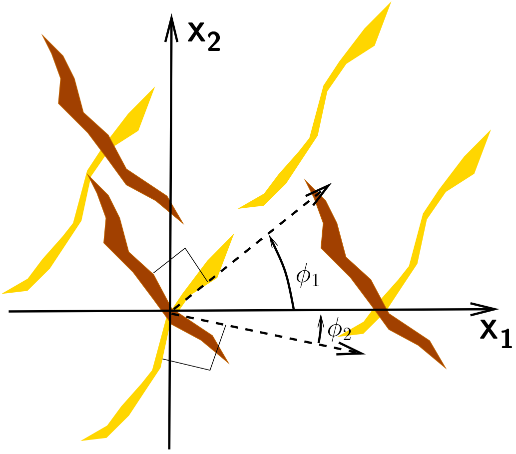

Figure 3.2: Two systems of parallel vertical fractures generally form an effective monoclinic medium with a horizontal symmetry plane. In the special case of two orthogonal ($\phi_1 + \phi_2 = 90°$) or identical systems the symmetry becomes orthorhombic.

If the symmetry plane of a monoclinic medium is orthogonal to the x$_3$-axis, the matrix of elastic parameters has the following form:

$$C_{pq} = \begin{pmatrix} C_{11} & C_{12} & C_{13} & & & C_{16} \\ & C_{22} & C_{23} & & & C_{26} \\ & & C_{33} & & & C_{36} \\ & & & C_{44} & C_{45} & \\ & & & & C_{55} & \\ & & & & & C_{66} \end{pmatrix}. \tag{3.4}$$

A medium with monoclinic symmetry can be described by 13 independent elastic parameters. The number of elastic parameters can be reduced from 13 to 12 by aligning the horizontal coordinate axes with the polarisation vectors of the vertically propagating shear waves, which eliminates the element c_{45}. In the special case of two identical or orthogonal vertical fracture sets, $\phi_1 + \phi_2 = 90°$ (see Figure 3.2), the model has orthorhombic symmetry.

3.2.3 Orthorhombic medium

The more often considered case is the orthorhombic symmetry, the symmetry of a brick. Orthorhombic models are characterised by three mutually orthogonal planes of mirror symmetry (see Figure 3.3). The corresponding cases in real rocks for this type of symmetry are for example (Thomsen, 2002):

- olivine, which has preferred orientation of crystals,
- thin-bed sequence, or a shale, with a set of fractures perpendicular to the layering (see Figure 3.3),

- a horizontally stratified thin-bed sequence, or a shale, or a massive isotropic sandstone, with orthogonal sets of vertical fractures in it.

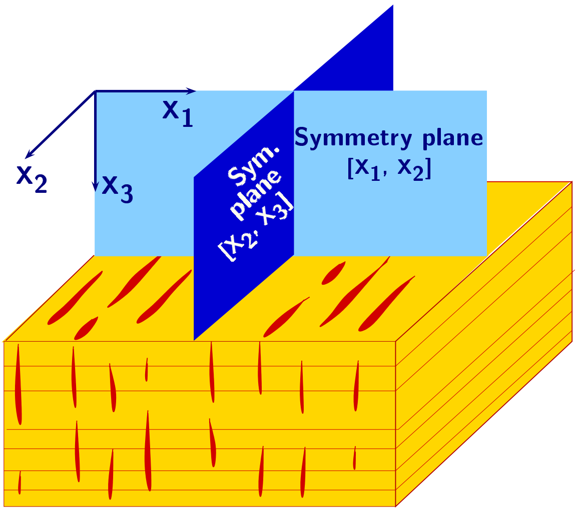

Figure 3.3: Orthorhombic model caused by parallel vertical fractures embedded in a finely layered medium. Here, one of the symmetry planes is horizontal, while the other two are parallel and normal to the fractures.

In the coordinate system associated with the symmetry planes the orthorhombic matrix has nine independent elements:

$$C_{pq} = \begin{pmatrix} C_{11} & C_{12} & C_{13} & & & \\ & C_{22} & C_{23} & & & \\ & & C_{33} & & & \\ & & & C_{44} & & \\ & & & & C_{55} & \\ & & & & & C_{66} \end{pmatrix}. \qquad (3.5)$$

3.2.4 Transversely isotropic medium

The transversely isotropic (TI) model is the most simple realistic case of anisotropy. This case is referred to as hexagonal symmetry in crystallography. The vast majority of existing studies of seismic anisotropy are performed for this type of media, which has a single axis of rotation symmetry. All seismic signatures in a TI model depend only on the angle between the propagation direction and the symmetry axis. Any plane that contains the symmetry axis represents a plane of mirror symmetry. The “isotropic plane” is perpendicular to the symmetry axis and the phase velocities of all three waves in this plane are independent of propagation direction. In this case the angle between the slowness vector and the symmetry axis remains constant (90°).

The TI model resulting from aligned plate-shaped clay particles adequately describes the intrinsic anisotropy of shales (Sayers, 1994). Shale formations comprise about 75% of the clastic fill of sedimentary basins, which makes transverse isotropy the most common anisotropic model. Most shale formations are horizontally layered, yielding a transversely isotropic medium with a vertical symmetry axis (VTI). Another common reason for TI is periodic thin-bed layering on a small scale in comparison to the predominant wavelength (see Figure 3.4).

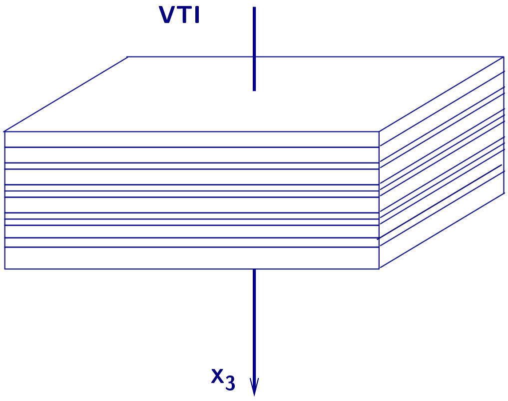

Figure 3.4: VTI model has a vertical axis of rotation symmetry x_3 and may be caused by thin-bed layered structure.

The elastic parameters of a VTI media are given by

$$C_{pq} = \begin{pmatrix} C_{11} & C_{11}-2C_{66} & C_{13} & & & \\ & C_{11} & C_{11}-2C_{66} & & & \\ & & C_{33} & & & \\ & & & C_{44} & & \\ & & & & C_{44} & \\ & & & & & C_{66} \end{pmatrix}. \tag{3.6}$$

This matrix has the same nonzero elements as that for the orthorhombic media, but the relationships between the elastic parameters C_{pq} reduce the number of independent stiffnesses in VTI media from nine to five.

In some areas transversely isotropic layers may be dipping, which leads to a tilt of the symmetry axis with respect to the earth surface (TTI medium). For example, up-tilted shale layers near salt domes are expected to produce an effective TTI model with large inclination of the symmetry axis. To obtain the elastic stiffness of TTI media, the elastic matrix for a VTI media (3.6) has to be rotated in accordance with the orientation of the symmetry axis.

A system of parallel vertical circular (so called "penny-shaped") cracks embedded in an isotropic background can be the reason for horizontal transversely isotropy (HTI). Hence, HTI is the simplest possible model of a formation with vertical fractures. The elastic stiffness can be obtained from the VTI model (for details see Tsvankin, 2001).

3.2.5 Thomsen parameters

To place emphasis on the anisotropy, Thomsen (1986) uses for transversely isotropic (TI) media the expression “polar **an**isotropy”. In such media velocities of seismic waves depend only on the direction of propagation measured against the symmetry axis. Thomsen (1986) has introduced a convenient parametrisation of this dependence, replacing the general notation of elastic anisotropy in terms of elastic constants C_{pq} by more physical parameters. The conventional notation in VTI has various disadvantages, e.g.:

- it is cumbersome to estimate the degree of velocity anisotropy just from inspection of the elastic parameters,
- there is no parameter provided for P-wave velocity near the (vertical) symmetry axis,
- the expression for the normal-moveout velocities in the conventional notation is complicated (Tsvankin, 2001).

Five elastic parameters can be replaced by P- and S-wave velocities along the symmetry axis (V_{P0} and V_{S0}) and the three dimensionless Thomsen parameters ϵ, δ, and γ:

$$\begin{aligned} V_{P0} &\equiv \sqrt{\frac{C_{33}}{\rho}}, & \epsilon &\equiv \frac{C_{11}-C_{33}}{2C_{33}}, \\ & & \delta &\equiv \frac{(C_{13}+C_{44})^2-(C_{33}-C_{44})^2}{2C_{33}(C_{33}-C_{44})}, \\ V_{S0} &\equiv \sqrt{\frac{C_{44}}{\rho}}, & \gamma &\equiv \frac{C_{66}-C_{44}}{2C_{44}}. \end{aligned} \tag{3.7}$$

In this notation P- and SV-wave signatures depend on the parameters V_{P0}, V_{S0}, ϵ and δ, while the SH-wave is fully described by the shear-wave vertical velocity V_{S0} and parameter γ. The dimensionless quantities ϵ, δ and γ approach zero for isotropic media and, therefore characterise the strength of anisotropy. Most rocks are only weakly anisotropic, even though many of their constituent minerals are highly anisotropic. Thomsen (1986) defines materials with small values ($\ll 1$) of “anisotropy” (defined by the three Thomsen parameters) as “weakly” anisotropic.

The parameter ϵ represents the simplistically called “P-wave anisotropy”, likewise the quantity γ means the same measure for SH-waves. For VTI media γ controls the normal-moveout velocity from horizontal reflectors and the small-angle reflection coefficient.

From equation (3.7) the Thomsen parameters are uniquely defined by the elastic parameters. However, the inverse transition is unique for only four coefficients (C_{11}, C_{33}, C_{44} and C_{66}). The remaining coefficient, C_{13}, can only be determined, if the sign of the sum $C_{13}+C_{44}$ is specified (see Tsvankin, 2001).

Elliptical anisotropy is a subset form of VTI anisotropic behaviour and is defined by the condition $\delta = \epsilon$. Soukina and Gajewski (2003) use this type of anisotropy as background media for perturbation methods.

3.2.6 Elliptical anisotropy

Elliptical anisotropy is a special case of transverse isotropic media with an additional constraint that reduces the number of independent elastic parameters to four:

$$(C_{13} + C_{44})^2 = (C_{11} - C_{44})(C_{33} - C_{44}). \tag{3.8}$$

Elliptical anisotropy is rarely found in real rocks. Nevertheless, this type of symmetry has significant advantages for verification purposes (see Helbig, 1983). Elliptical anisotropy allows the analytical calculation of traveltimes for all three types of waves and synthetic seismograms in a homogeneous medium (see appendix C). Figure 3.5 shows the polarisation vectors for all three types of waves (qP, qSV, SH).

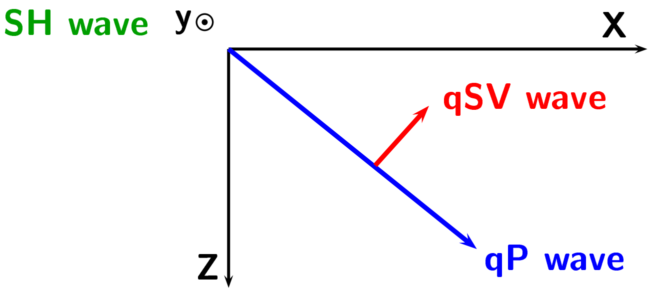

Figure 3.5: Polarisation vectors in a medium with elliptical anisotropy. The qP- and qSV- waves propagate in the x-z-plane, the SH-wave polarisation vector is oriented along the y-axis, pointing to the reader.

The phase velocities for the transversely polarised mode are defined by the elastic parameters and in terms of the phase angle θ with the symmetry axis:

$$V_{SH}(\theta) = \sqrt{\frac{C_{66}\sin^2\theta + C_{44}\cos^2\theta}{\rho}}. \tag{3.9}$$

For vertical propagation ($\theta = 0°$) the SH-velocity is equal to $\sqrt{C_{44}/\rho}$, while in the horizontal direction $V_{SH}(\theta = 90°) = \sqrt{C_{66}/\rho}$. According to equation (3.9), it marks out an ellipse with the axes in the vertical and horizontal directions, if the slowness $1/V_{SH}$ is plotted as the radius-vector in the direction θ. Therefore, the SH-wave anisotropy in TI media is called elliptical.

3.2.7 Isotropic medium

The isotropic model has the highest form of symmetry: an isotropic medium is defined by the two Lamé parameters λ and μ and the density ρ or v_s, v_p. Thus, the elastic matrix for this symmetry the C_{pq} reads:

$$C_{pq} = \frac{1}{\rho} \begin{pmatrix} \lambda+2\mu & \lambda & \lambda & & & \\ & \lambda+2\mu & \lambda & & & \\ & & \lambda+2\mu & & & \\ & & & \mu & & \\ & & & & \mu & \\ & & & & & \mu \end{pmatrix}. \tag{3.10}$$

The velocities v_s, v_p are related to λ and μ as follows:

$$v_p = \sqrt{\frac{\lambda+2\mu}{\rho}}, \qquad v_s = \sqrt{\frac{\mu}{\rho}}. \tag{3.11}$$

Although the earth is usually anisotropic, isotropic models have been successfully applied, because the anisotropy is almost always small. The reason for the long neglect of anisotropy is, of course, that isotropy is simpler to handle. The equations are simpler and the application of physical intuition is more direct. Also, anisotropic techniques are computationally expensive and have therefore only recently gained practical importance. The fast development in computing capacity and storage as well as a better data base and new algorithms for imaging now allow to consider anisotropy in seismic methods.

3.3 Factorised anisotropic inhomogeneous medium

A specification and parametrisation of an arbitrary 3-D anisotropic inhomogeneous media is not simple. In a general case, all 21 density normalized elastic parameters a_{ilkj} may depend on Cartesian coordinates in a different way. Thus, the model has to specified by 21 elastic medium parameters as a function of three coordinates, which requires a high amount of computational time as well as of data storage. For this reason, usually only simpler anisotropic inhomogeneous media are considered in computations. The simplification of the medium usually follows one of the two following approaches (or both of them). In the first approach, the type of anisotropy is simplified. This reduces the number of elastic parameters (see section 3.2). In the other approach, the spatial distributions of individual elastic parameters are approximated by some simple functions. For example, the elastic parameters are assumed to vary linearly with Cartesian coordinates. Most often, both these approaches are combined.

Červený (1989) propose a more general specification of the anisotropic inhomogeneous medium, and calls it factorised anisotropic inhomogeneous (FAI) medium.
In the FAI medium the density normalised elastic parameters a_{ijkl} are defined by the following relations:

$$a_{ijkl}(x_i) = f^2(x_i)a_{ijkl}^{const}, \qquad (3.12)$$

where a_{ijkl}^{const} are constants, independent of the Cartesian coordinates, and $f(x_i)$ is an arbitrary positive continuous function of Cartesian coordinates. Therefore, in a factorised medium the elastic parameters a_{ijkl}^{const} describe the anisotropy of the model, whereas $f(x_i)$ define the heterogeneity, i.e. in a FAI medium the symmetry type is fixed.
It is also assumed that the first partial derivatives of f with respect to the Cartesian coordinates, $\partial f/\partial x_i$, are continuous, and that the second partial derivatives are piecewise continuous functions of the Cartesian coordinates. Therefore, all the density normalised elastic parameters $a_{ijkl}(x_i)$ in the FAI medium depend on Cartesian coordinates in the same way. In Figure 3.6 an example for such a factor function $f^2(x_i)$ is shown. Here, the model is given by a low velocity inclusion in an homogeneous background medium. The figure shows a 2-D slice of a 3-D model.

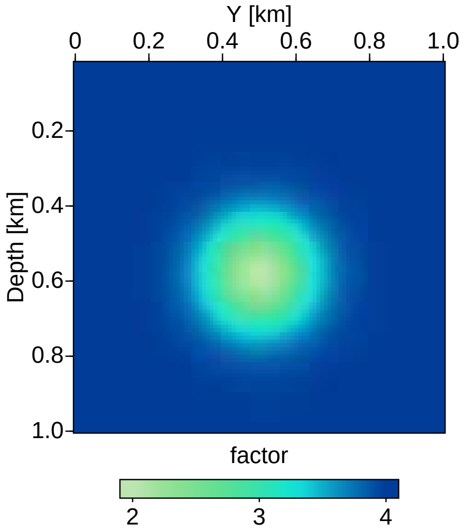

Figure 3.6: Example for a smooth factor-field.

Chapter 4

Wavefront-oriented ray tracing

This chapter provides a basic overview of the concept of wavefront-oriented ray tracing with special focus on the innovations for the anisotropic case.
The traditional, i.e. two-point ray-tracing method is computationally expensive when traveltimes are required for an entire 2-D or 3-D grid. During the last years several authors have introduced new ray-tracing based methods, so-called wavefront construction methods (Vinje et al., 1993b; Lambaré et al., 1996; Lucio et al., 1996). The basic idea of wavefront construction is to propagate a ray field rather than a single ray (see Figure 4.1). Wavefronts are defined as isochron traveltime surfaces (lines in 2-D) from the source.

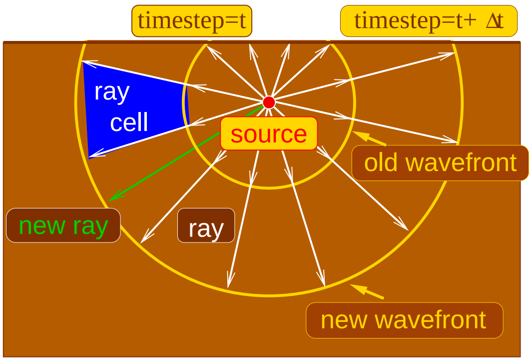

Figure 4.1: Wavefront-construction methods propagate a ray field rather than a single ray. A new wavefront is constructed from the old one by propagating the ray field with a constant traveltime step Δt. In case of insufficient illumination a new ray is inserted between two adjacent rays.

New wavefronts are constructed from previous ones, by ray tracing over a time step Δt. As wavefronts propagate, new rays are interpolated between rays that go further apart than a predefined distance. Figure 4.1 illustrates how wavefronts propagate, by ray tracing from a time t to a time t+Δt.

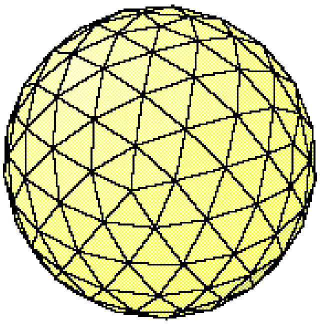

Figure 4.2: Representation of the wavefront by a triangular network.

In general, the representation of a 3-D wavefront is somewhat more complicated than in 2-D, where the rays are situated side-by-side along the 2-D wavefront. The term “neighbouring” or “adjacent” ray is more difficult to define on a 3-D wavefront, where the rays are distributed in two dimensions on the front. Some kind of network connecting the rays on such a 3-D wavefront must be defined.

It was proved in 1925 that every compact surface can be triangulated with a finite number of triangles (Rössl et al., 2000). Triangulation is the division of a surface into a set of triangles, usually with the condition that each triangle side is entirely shared by two adjacent triangles. Triangle meshes are popular representation of surfaces, e.g., in computer graphics.

Vinje et al. (1996) suggest to represent a wavefront by a network of triangles (see Figure 4.2). The vertices of the triangles are the intersection points between rays and wavefronts. The triangular network has a simple topology and the ability to adjust to the stretching and twisting of the wavefront during the propagation through the medium. For instance, Figure 4.3 shows two wavefronts at two sequent time steps for a heterogeneous isotropic model. The wavefronts are computed for a model with an embedded positive velocity lens, where the velocity increases smoothly from the border to the center.

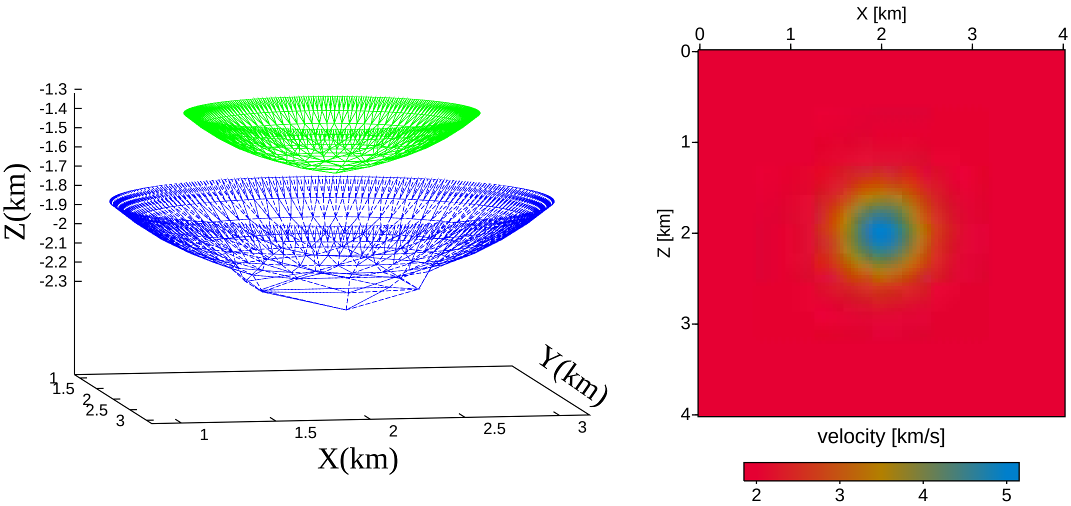

Figure 4.3: The left figure shows wavefronts at two sequent time steps. The model has an embedded positive velocity lens in the center, where the velocity increases from the boundary of the lens ($v = 2\,km/s$) to the center ($v = 5\,km/s$).

In addition, using a set of triangles to represent the wavefront facilitates the integration of new rays into the network (see also section 4.5).

The wavefront-oriented ray-tracing technique can be divided into four main parts, which will be described in more detail in this chapter:

- The definition of the input model on a rectangular grid, including Cardinal-spline interpolation (section 4.2).

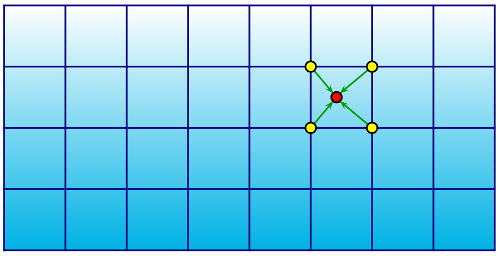

- The initialisation of a wavefront (section 4.1), where
  - the source location, and
  - the slowness of the rays starting at the source have to be defined.

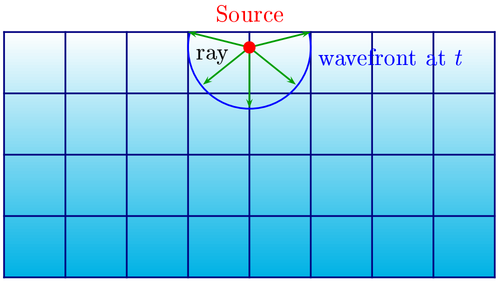

- The propagation of the wavefronts by
  - solving the ray-tracing system (section 4.4), and
  - inserting a new ray, if necessary (section 4.5).

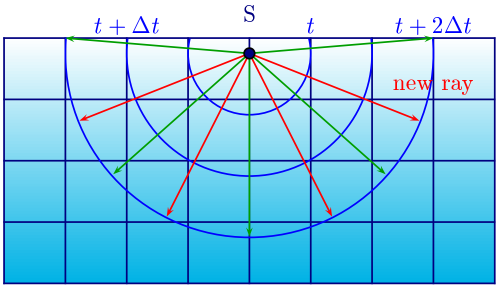

- The interpolation of the traveltimes onto the rectangular grid after each time step (section 4.6).

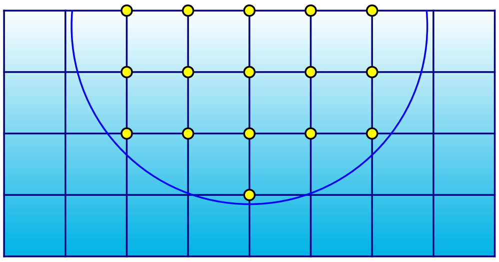

Coman (2003) presented an implementation to compute traveltimes by wavefront-oriented ray tracing in smooth inhomogeneous isotropic media. Based on this efficient and accurate technique for isotropic media, his method was extended in this work to compute traveltimes in smooth 3-D anisotropic inhomogeneous media.

Modifications due to the anisotropy

To apply the wavefront-oriented ray tracing technique to anisotropic media several changes of the implementation have to realised.

Initial conditions

As mentioned above, the initial conditions in anisotropic media specify not only the initial point $\vec{x}^S$ and the initial direction $\vec{p}^S$ of the ray, but also the type of wave (m) that is to be computed. Therefore, after defining the phase normal vector $\vec{n}^S$ by the two take-off angles the phase velocity at the source corresponding to the wave type for direction $\vec{n}_0$ has to be computed. Thus, the slowness at the source is given by:

$$\vec{p}^S = \frac{\vec{n}^S}{V^{(m)}}. \tag{4.1}$$

If the medium is supposed to be isotropic, the phase velocity and the group velocity are identical and equal for each ray at the source. In the anisotropic case, the phase velocity for each ray has to be computed by solving the eigenvalue problem (2.41).

Definition of the model

In comparison to an isotropic medium, which can be described by two elastic parameters, the number of non-vanishing elastic parameters of an anisotropic medium increases up to 21. For instance, if the subsurface structure is supposed to be transversely isotropic, the medium could be described by five independent elastic parameter (see section 3.2). However, the number of non-vanishing elements of the stiffness matrix increases if the crystal symmetry does not coincide with the acquisition coordinate system.
The elastic stiffness matrix of a triclinic anisotropic medium consists of 21 independent elastic parameters in any coordinate frame. To provide an efficient, accurate and fast algorithm for the computation of the elastic parameters, the trilinear interpolation was replaced by the Cardinal splines.

The ray tracing system

Instead of assuming the simplified ray tracing system (4.14) for isotropic media, in the anisotropic case the ray tracing system (2.28) has to be solved. Just as in the isotropic implementation the numerical solution of this system of differential equations is realised by the Runge-Kutta-technique. The only difference is the definition of the right hand sides in the ray tracing system (2.28).

Interpolation of traveltimes to grid points

In general, the interpolation of the traveltimes to grid points in an anisotropic medium works similar to the isotropic case. The traveltime to a grid point will be approximated using a distance-weighted interpolation (Coman, 2003). However, since for this interpolation the velocity within the ray cell is needed, in the anisotropic implementation it has to distinguished between phase and group velocity. To run the program a graphical interface was designed (see appendix B). In the next section the modifications of the implementation of the wavefront-oriented ray tracing for anisotropic media are explained in more detail. The next section explains the definition of the point source by the construction of the first wavefront.

4.1 Construction of a point source

To start the 3-D wavefront-oriented ray tracing an initial wavefront is required. Following Vinje et al. (1996), the wavefronts can be represented by a network of triangles. Thus, an icosahedron (Figure 4.4) with twelve vertices is used to construct the first wavefront. The initial wavefront is defined by twelve rays which start from the source point (center of the icosahedron) and nearly pass through the vertices of the icosahedron. The rays pass exact through the vertices only if the region near the source is homogeneous and isotropic.

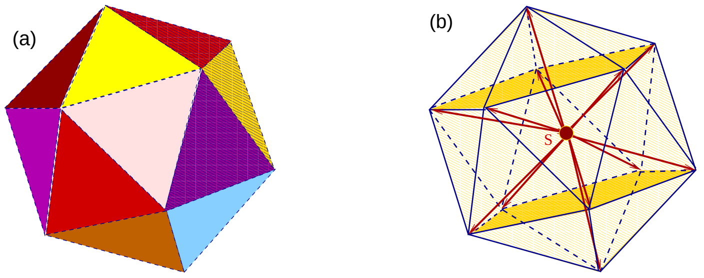

Figure 4.4: (a) The icosahedron describes the basic network of the point source. (b) The twelve rays from the source position in the center pass through the vertices of the icosahedron.

For each wavefront the vertices are the intersection points between rays and wavefronts. The advantage of using the icosahedron lies in the equidistant angle between neighbouring rays. The angle between each ray pair is 63.43 degrees. In order to start with a larger number of rays, a new ray is inserted between each pair of adjacent rays (see also Figure 4.5).

Figure 4.5: Increasing of the number of rays leads to different shapes of the initial wavefront at the source. (a) A polyhedron with 80 triangles is obtained by inserting a new ray between each adjacent rays. (b) After the next iteration the wavefront is constructed by 320 triangles and the third iteration leads to 1280 triangles (c).

In the isotropic case, if the two take-off angles i_0 and ϕ_0 and the velocity v at the source are given, the slowness for all rays at the source can be calculated by equation (2.32).
In an anisotropic model the slowness at the source depends on the take-off angles i_0 and ϕ_0 and the phase velocity V_0 for the corresponding ray. In contrast to the isotropic case the phase velocity V_0 depends on the direction of the ray. Therefore, for each starting ray the components of the normal of the wavefront (2.39) are determined. By applying (2.26) the phase velocity at the source (2.41) can be expressed as follows:

$$V_0^2 = a^S_{ijkl} n_j n_l D^{(m)}_{ik} / D, \tag{4.2}$$

where a^S_{ijkl} represents the density normalised elastic parameters at the source location. This must be solved for each normal vector $\vec{n}$. Then, the slowness vector follows from 4.1 and (m) specifies the wave type.
Even if the angle between each ray pair at the source in an inhomogeneous anisotropic media can diverged, the proceeding to apply a icosahedron as initial wavefront can provide a sufficient coverage at the source

4.2 Interpolation of model parameters

In the isotropic case the velocity v, and in the anisotropic model the elastic parameters C_{pq}, are given on a rectangular grid. During the propagation through the model the kinematic ray-tracing system has to be solved for each time step . It is unlikely that the ray ends on a grid point where the velocities or the elastic parameters are known. As they are required at the end point of the ray, an interpolation of the input quantities becomes necessary (see Figure 4.6).

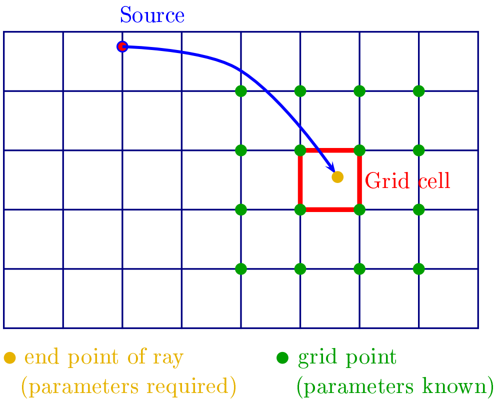

Figure 4.6: Since it is not likely that a propagating ray ends on a grid point an interpolation of v or C_{pq} is necessary.

In this work the following interpolation algorithms were taken into consideration:

- Trilinear interpolation: the simplest and fastest method.

- Cubic spline interpolation: an interpolation with high accuracy, but also high demands on computational storage and time.
- Cardinal Splines: nearly the same accuracy as the Cubic splines, but faster.

Even if in most cases the anisotropic subsurface model is supposed to be transversely isotropic (VTI or HTI), the stiffness matrix may have more than five non-vanishing components. The number of elastic constants given in chapter 3 for the different symmetry systems apply generally only if they are obtained with reference to the acquisition coordinate system (see for instance Figure 4.7).

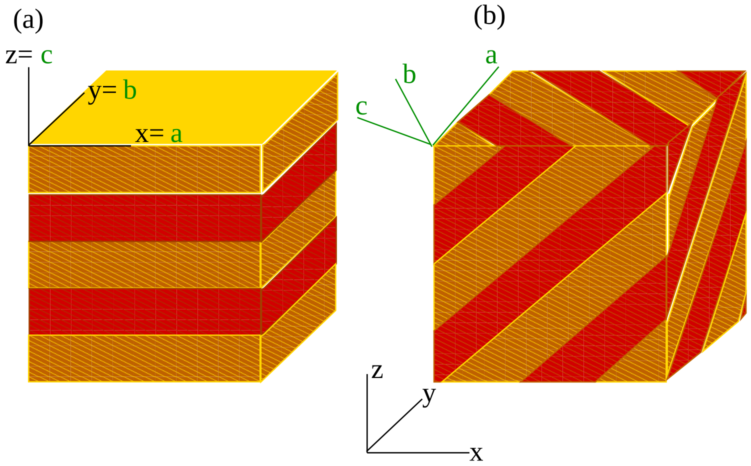

Figure 4.7: Block of foliated rock with no tilt; material a-b-c axes are coincident with geographical x-y-z axes. For transverse isotropy (hexagonal symmetry) the a and b directions have the same behaviour. (b) Here the crystal symmetry axes (a-b-c) is tilted with respect to acquisition coordinate system x-y-z.

There are two obvious exceptions to the rule that an arbitrary change of the coordinate system increases the number of elastic constants: the triclinic system has 21 independent elastic parameters in any coordinate frame (except for at least three frames where there are only 18 non-vanishing stiffnesses, see, e.g., Helbig, K. and Treitel, S. (1994)), and isotropic media are completely invariant against any rotation. Therefore, in an arbitrarily oriented coordinate system any non-isotropic medium may have 21 non-vanishing components of the stiffness tensor. Consequently, besides being accurate the interpolation must be also fast and economical in terms of computational storage and time.

Interpolation within a 3-D regular grid is often based on the trilinear interpolation method, in which the interpolated value at any point is interpolated linearly from values at 8 nodes of a cube that encloses this point. The advantage of trilinear interpolation is its simplicity and in many cases it leads to a good sufficient approximation. The main disadvantage of the trilinear interpolation, which is the fastest method, is the absence of any connection between the interpolated value and its first derivative. Both are interpolated by weighting the values at the neighbouring grid points. Here, the weight does not depend on the function values. Thus, the first derivative at a grid point is calculated by multiplying the derivatives with the weights (in general proportional to the distances to the grid points) and therefore do not consider the function values itself. For instance, Figure 4.8 shows a velocity-depth function, where a non-uniqueness of the derivative at grid point x_k occurs. In situations where continuity of derivatives is a concern, one must use the a more sophisticated interpolation provided by a so-called spline function.

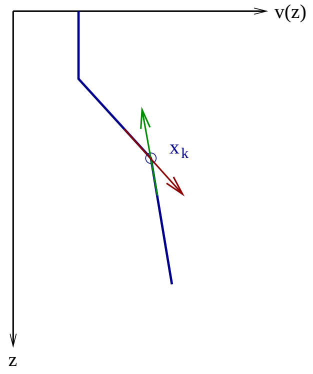

Figure 4.8: Exemplary a 1-D velocity/depth distribution.

A spline is a polynomial between each pair of table points, but one whose coefficients are determined "slightly" non-locally. The non-locality is designed to guarantee global smoothness in the interpolated function up to some order of derivative (Press et al., 1992). Cubic splines are the most popular. They produce an interpolated function that is continuous through the second derivative. The number of points (minus one) used in the interpolation scheme is called the order of the interpolation. Increasing the order does not necessarily increase the accuracy, especially in polynomial interpolation. If the added points are distant from the point of interest, the resulting higher-order polynomial, with its additional constrained points, tends to oscillate between the tabulated values. This oscillation may have no relation to the behaviour of the "true" function (see for example Figure 4.9(b)). As it can be seen in Figure 4.9 a smooth function is more accurately interpolated by a high-order polynomial than by a low-order polynomial. Since for the ray tracing procedure the model has to be smoothed anyway, spline interpolation is preferred.

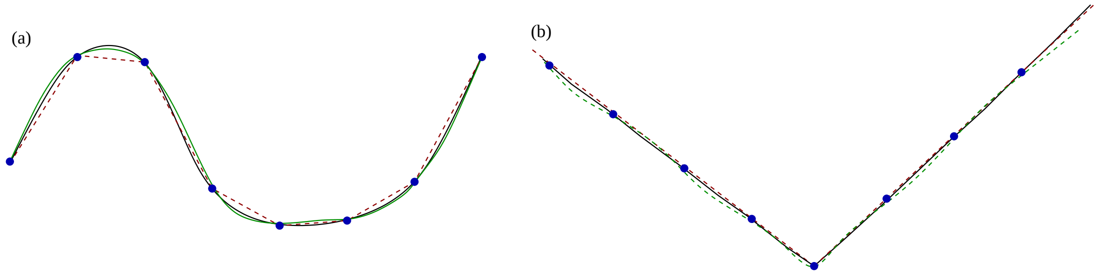

Figure 4.9: (a) A smooth function (solid black line) is more accurately interpolated by high-order polynomial (schematically shown by the green line) than by a low-order (shown as a piecewise linear dashed line). (b) A function with sharp corners or rapidly changing higher derivatives is less accurately approximated by a high-order polynomial (green line) than by a low-order polynomial.

The Cubic spline interpolation calculates individual weights for each grid cell (see Figure 4.6). To get the function value (Figure 4.6 orange dot) in a 2-D model, the 16 surrounding grid points (Figure 4.6 green dots) are used, whereas in 3-D the number of used grid points is 64. Assuming a 3-D model with 100 grid points in each direction for the interpolation of each of the 21 elastic parameters $64 \cdot 10^6$ weights must be calculated and stored. Thus, the Cubic splines are not recommended, because of the demands in computational storage and

CPU time. Instead of Cubic spline interpolation, we have implemented a Cardinal spline interpolation. In the next section the theoretical background and tests of the accuracy of the Cardinal splines are presented.

4.2.1 Cardinal splines

Thomson and Gubbins (1982) have introduced the idea of using Cardinal splines for the computation of 3-D model quantities. The Cardinal spline interpolation is based on the Hermite interpolation (see also appendix A). But instead of using the derivatives of the values at grid points directly, as in the Hermite interpolation, Cardinal splines use only the function values of the surrounding grid points. In contrast to the Cubic splines, where individual spline functions for each grid cell are calculated, the Cardinal splines depend only on the distance between the ray end point and the nearest grid point.

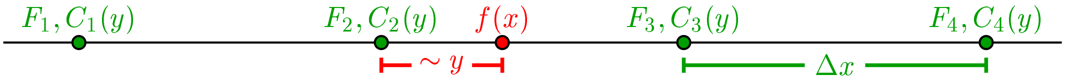

Figure 4.10: To determine $f(x)$ in the one-dimensional case the function values F_l at four points neighbouring x are weighted by the Cardinal spline weights $C_l(y)$.

The contribution of each point to the function value at x is weighted by a precalculated Cardinal spline weight C_l:

$$f(x) = \sum_{l=1}^{4} F_l C_l(y), \tag{4.3}$$

where the F_l are the function values of the four neighbouring grid points (see Figure 4.10). The Cardinal spline weights C_l are independent of the location of x in the model. This is the main difference to the common Cubic splines, where for each grid cell a set of individual weights have to be determined.
The Cardinal splines are calculated by:

$$C_l(y) = H(y-l) + \Delta x \sum_{k=1}^{4} G_{kl} H_1(y-k), \quad l = 1,2,3,4. \tag{4.4}$$

The functions H (A.2) and H_1 (A.3) are linked to the Hermite interpolation. The matrix G_{kl} is defined by

$$G_{kl} = \frac{1}{2\Delta x} \begin{pmatrix} -2 & 1 & 2 & -1 \\ -1 & 0 & 1 & 0 \\ 0 & -1 & 0 & 1 \\ 1 & -2 & -1 & 2 \end{pmatrix}, \tag{4.5}$$

(the derivation is given in appendix A).

Accuracy of the Cardinal Splines

The accuracy of the Cardinal spline interpolation will be demonstrated in this section. A 3-D function defined by:

$$f(x, y, z) = 2\sin(x) + \cos(y) + 0.5\sin(z) + 4 \tag{4.6}$$

is used for the test. The function (4.6) can be interpreted as a velocity model. The velocity values range between 2 km/s and 6 km/s (see Figure 4.11). The velocity range and the distribution of velocity values in the model make high demands on the interpolation algorithm. Thus, this more or less unrealistic model is used for testing the Cardinal spline interpolation. The function values are calculated at two different grids:

	Coarse grid	Fine grid
nx, ny, nz	26	101
dx, dy, dz	0.2 km	0.05 km

The model dimension in each direction is 5 kilometer. To test the Cardinal splines the coarse grid was used as input and the values on the fine grid were interpolated. Figure 4.11 visualises the input model on the left side, defined by relation (4.6), and the right side shows the result after the interpolation onto the fine grid.

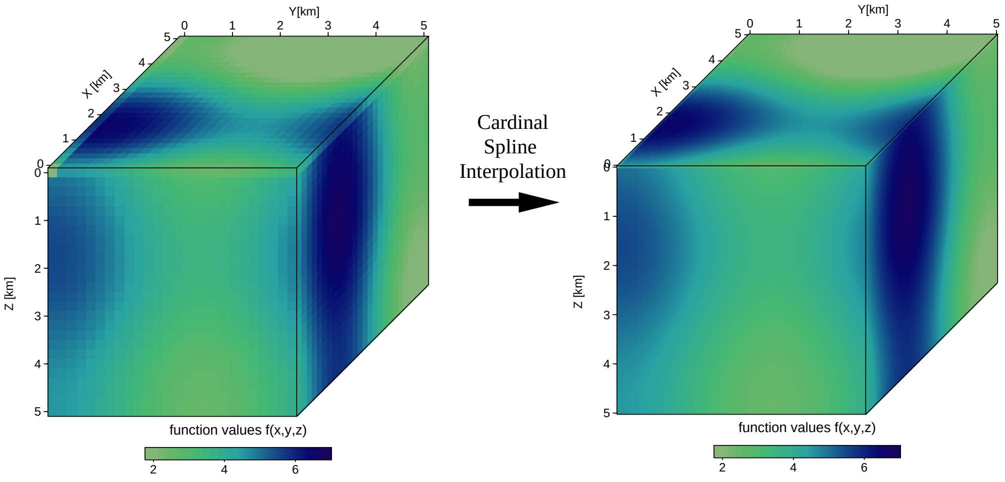

Figure 4.11: Left: the coarsely gridded input model. Right: the result of the interpolation onto the fine grid using the Cardinal spline interpolation.

To evaluate the accuracy of the Cardinal splines, the results are compared with the analytically computed values on the fine grid. The left side in Figure 4.12 displays the analytical values and on the right side the relative errors are shown. The absolute error ranges between -0.001 and 0.001 and reflects the lattice-like pattern of the coarse input-grid. The maximum relative error of 0.06% is located where the function value is smaller than in the remaining part of the model ($x = 3.0 - 5.0$ and $y = 1.0 - 4.0$). However, for the most part of the model the relative error is less than 0.02%. This corresponds to an adequate accuracy for the input quantities. For the solution of the kinematic ray-tracing system, not only the velocities or the elastic parameters, but also the derivatives of the elastic parameters at the ray end points are needed.

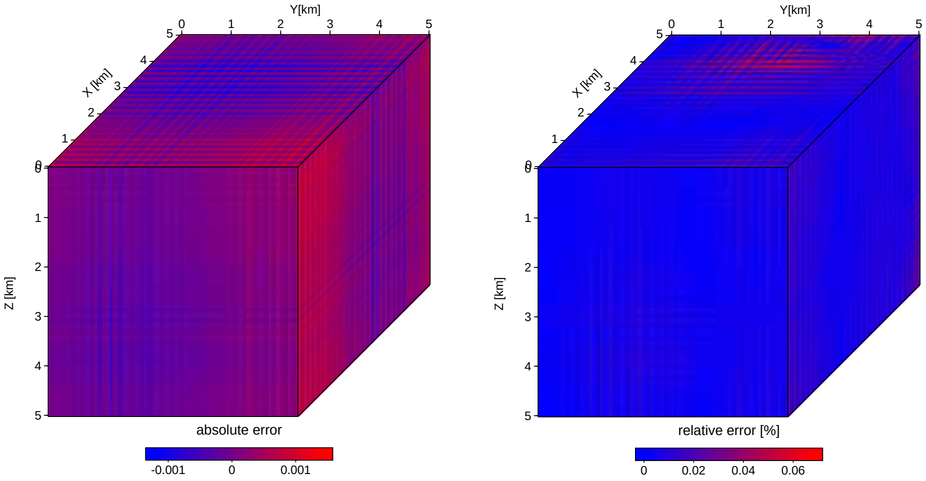

Figure 4.12: Absolute errors (left) and the relative errors (right) of the interpolated values.

The accuracy of the interpolation of the derivatives is also tested on the 3-D function (4.6). The analytical solution is calculated on the coarse grid and on a fine grid, which will be taken as the reference medium. The model dimensions are the same as for the first accuracy test of the function value (see Table 4.2.1). The analytical values for the derivatives are:

$$\frac{df(x,y,z)}{dx} = 2\cos(x), \quad \frac{df(x,y,z)}{dy} = -\sin(y), \quad \frac{df(x,y,z)}{dz} = 0.5\cos(z). \tag{4.7}$$

For the first derivatives the results of the calculation are shown in Figures 4.13-4.15. Figure 4.13(a) shows the analytical values of the first derivatives in x-direction calculated on the fine grid. The absolute errors of the Cardinal spline interpolation are presented by 2-D slices through the center of the model ($x = 2.5$, $y = 2.5$ and $z = 2.5$ (Figure 4.13(b)-(c)). Here, the observed absolute errors range between -0.01 and 0.01, exhibiting a correlation between the maximum errors and the greatest derivative values. In addition, four different 2-D slices in the $y - z$-plane are presented 4.13(e), where the variation of the absolute errors is obviously smaller than in the $x - z$- and $x - y$-plain. The error distribution correlates to the shape of the input function. For each grid point the same derivative value is interpolated by using the surrounding function values (see text above). Accordingly, Figure 4.14 and Figure 4.15 show the absolute errors for the derivative in y- and z-direction. Apart from slightly different error ranges, these results confirm the observations for the first derivative in the x-direction.

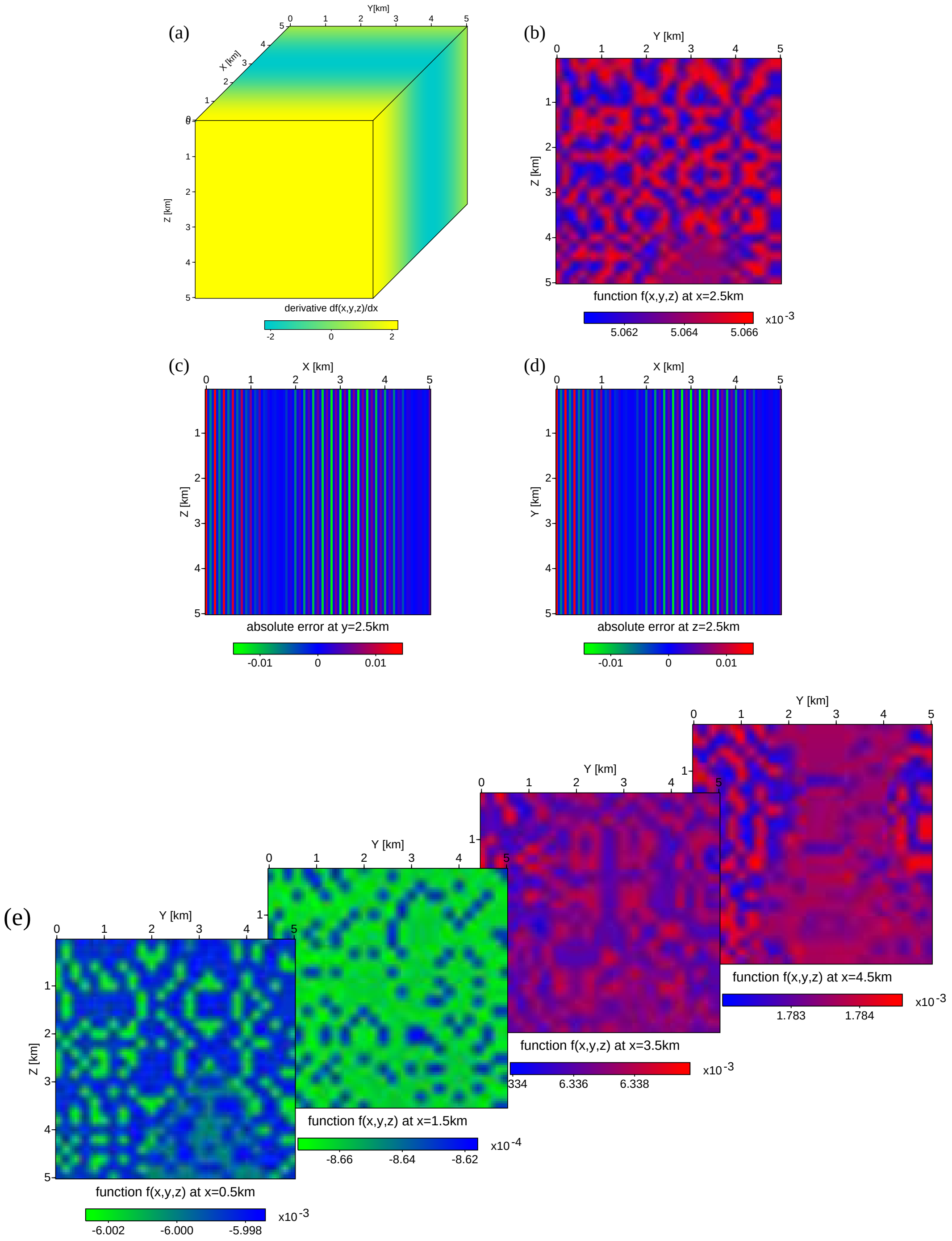

Figure 4.13: (a) Analytical values ($df(x, y, z)/dx$) calculated on the fine grid. (b)-(d) The comparison of the analytical results with the results of the Cardinal Spline interpolation are shown. The figures display 2-D slices through the center of the model ($x = 2.5$, $y = 2.5$ and $z = 2.5$). (e) In addition, four different 2-D slices in the $y - z$-plane are presented ($x = 0.5$, $x = 1.5$, $x = 3.5$ and $x = 4.5$). Please notice the different error scale.

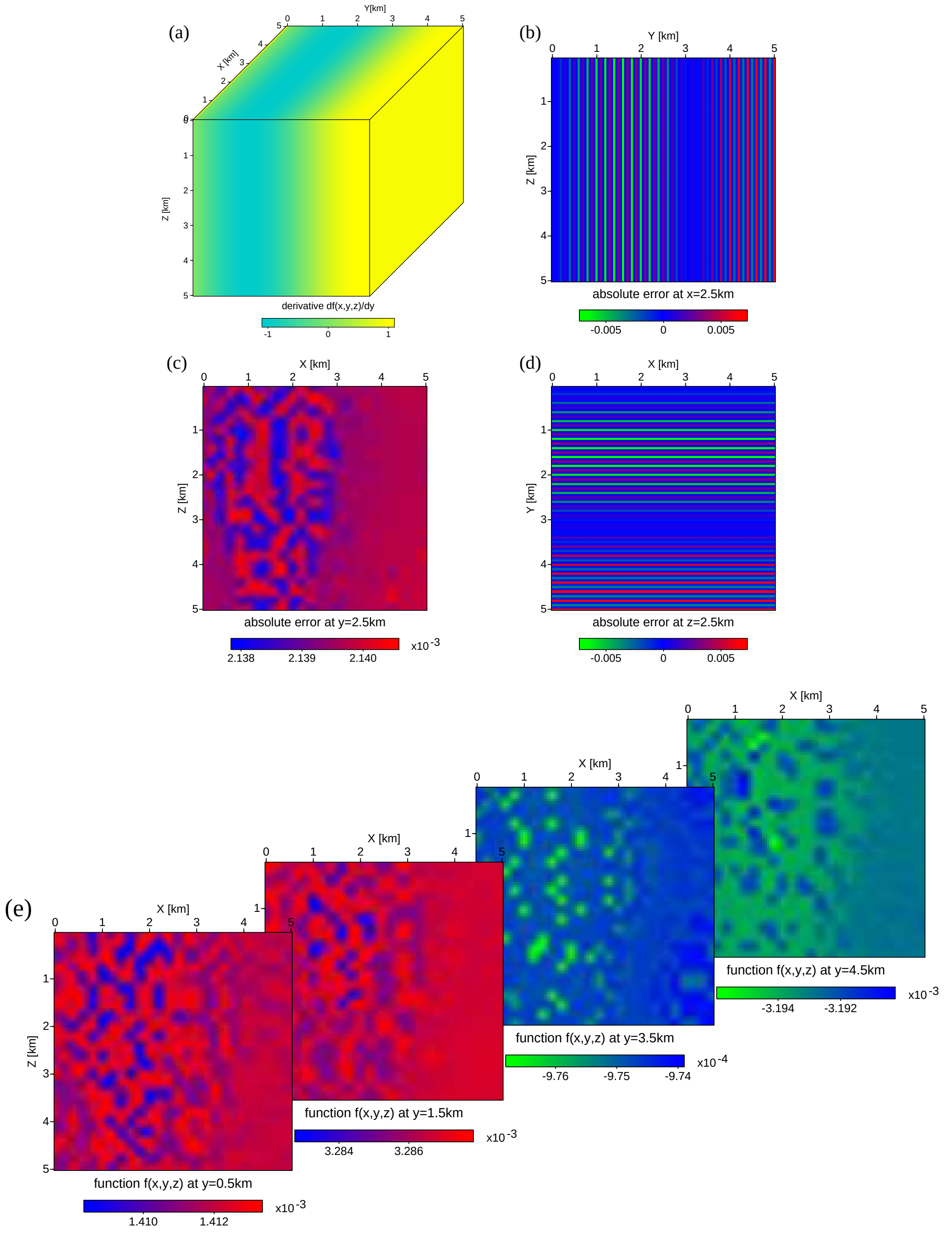

Figure 4.14: (a) Analytical values ($df(x, y, z)/dy$) calculated on the fine grid. (b)-(d) The comparison of the analytical results with the results of the Cardinal Spline interpolation are shown. The figures display 2-D slices through the center of the model ($x = 2.5$, $y = 2.5$ and $z = 2.5$). (e) In addition, four different 2-D slices in the $x - z$-plane are presented ($y = 0.5$, $y = 1.5$, $y = 3.5$ and $y = 4.5$). Please notice the different error scale.

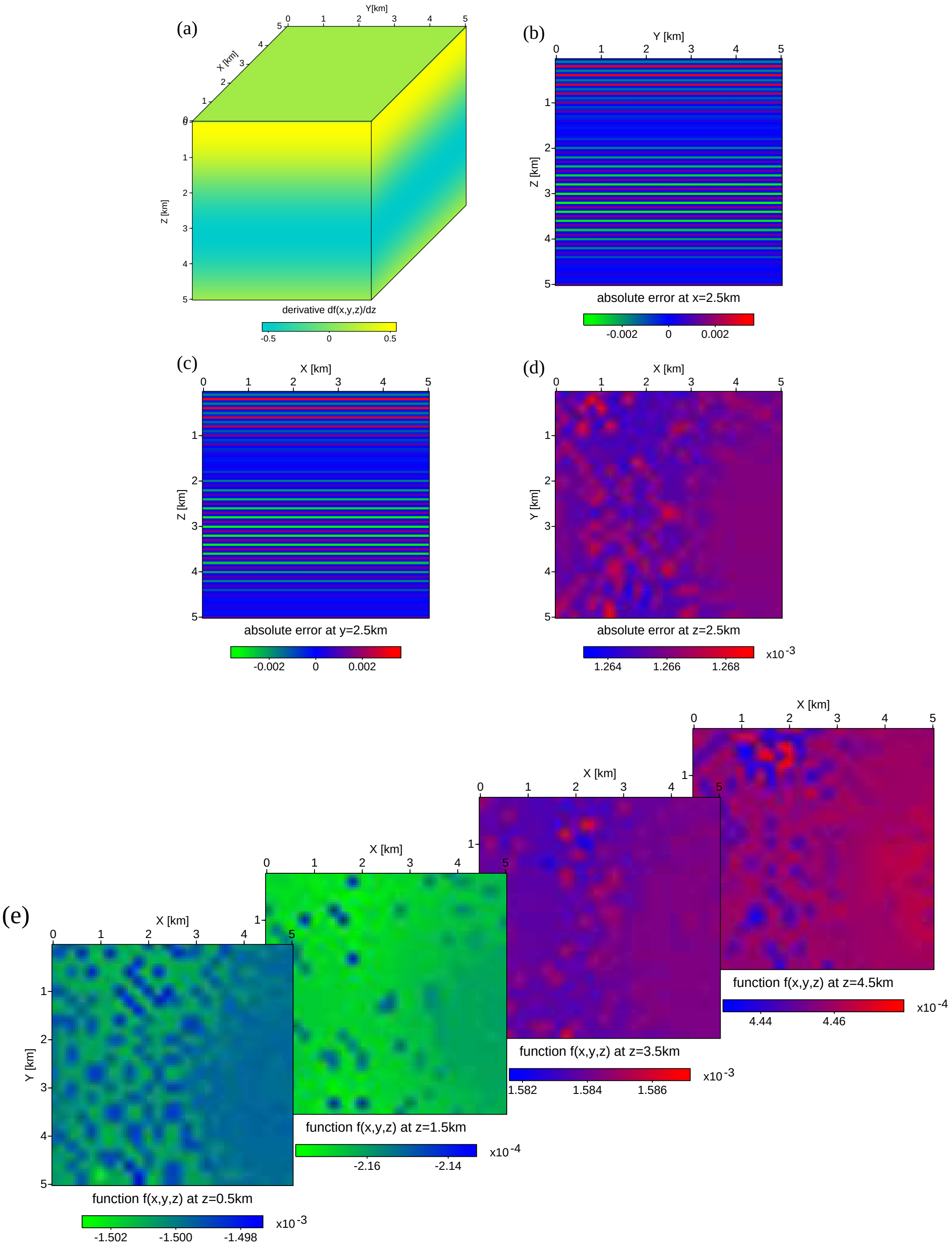

Figure 4.15: (a) Analytical values ($df(x,y,z)/dz$) calculated on the fine grid. (b)-(d) The comparison of the analytical results with the results of the Cardinal Spline interpolation are shown. The figures display 2-D slices through the center of the model ($x = 2.5$, $y = 2.5$ and $z = 2.5$). (e) In addition, four different 2-D slices in the $x - y$-plane are presented ($z = 0.5$, $z = 1.5$, $z = 3.5$ and $z = 4.5$). Please notice the different error scale.

4.3 Smoothing of the model

The ray tracing procedure requires smooth models. Smoothing influences also the quality of migration images, in the way that too much smoothing reduces the image quality. Therefore, the model has to be smooth enough, so that the ray tracing theory is applicable, but the model behaviour should change as little as possible to limit the loss of image quality. Kravtsov and Orlov (1990) formulated: the model parameters, for instance the velocity or the elastic parameters, must vary insignificantly over the wavelength λ in the propagated medium. Mathematically this can be expressed with:

$$\frac{\lambda}{L} \ll 1, \tag{4.8}$$

where L represents the smallest of the characteristic length and λ the wavelength of the medium. Here this characteristic length is taken as the distance over which the increment of a certain variable, for example the velocity:

$$L = \mathrm{Min}\left(\frac{v}{|\vec{\nabla} v|}\right), \tag{4.9}$$

is comparable with it in value (details see Kravtsov and Orlov, 1990).
In this work a low pass filtering process is used to attenuate short period spatial velocity variations. Smoothing the slowness preserves the traveltime better than to smooth the velocity model, because the traveltime is proportional to the slowness (vertical smoothing preserves vertical traveltimes etc.). A common 1-D smoothing operator is

$$A = \left(\frac{1-w}{2}\,, w\,, \frac{1-w}{2}\right), \tag{4.10}$$

to be convolved n-times with the model. In this work the common weight $w = 0.5$ is used. The result is:

$$p_i^{j+1} = \frac{1-w}{2}\, p_{i-1}^j + w\, p_i^j + \frac{1-w}{2}\, p_{i+1}^j \quad i = 1, \ldots, N, \quad j = 1, \ldots, n, \tag{4.11}$$

where N is the number of samples in z- or x-direction and with j being the number of iterations already done. As convolution in the space domain corresponds to multiplication in the wavenumber (k) domain, we use the Fourier transform of

$$A(x) = \frac{\delta(x+\Delta x)}{4} + \frac{\delta(x)}{2} + \frac{\delta(x-\Delta x)}{4},$$

with Δx being the spatial sampling interval. Integration yields

$$A(k) = \cos^2(\pi\, k\, \Delta x) = \cos^2\left(\frac{\pi\, \Delta x}{\lambda}\right).$$

Therefore, the n-times application of the smoothing operator in the space domain equals multiplication with the n-th power of $A(k)$ in the k-domain. The resulting filter curves are displayed for different values of n. The grid spacing is 10m in this example.

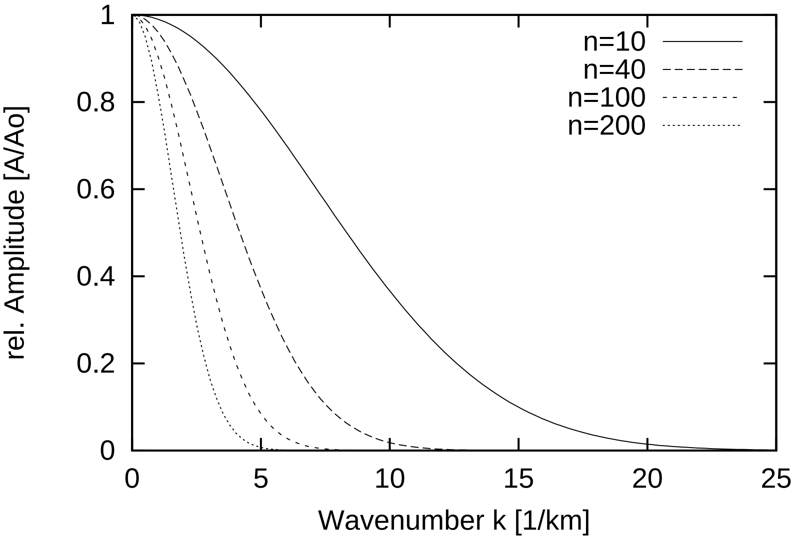

Figure 4.16: Resulting filter curves for different values of n.

Figure 4.17 shows examples for smoothing. The blocky model (Figure 4.17(a)) is smoothed by the three-point operator. Figure 4.17(b) and 4.17(c) show the resulting 10-fold and the 100-fold smoothed model (4.17(c)).

The necessity of smoothing is something that all methods have in common, which are based on the high frequency approximation. Smoothing is a process which occurs in the propagation of real seismic waves. In the far field we observe band limited signals with limited resolution since the Earth serves as a low pass filter during propagation (Gajewski et al., 2002). Thus, suitable smoothing appears to be a natural process.

For an inhomogeneous anisotropic medium we also have to smooth the input quantities, but here it is much more unclear what the smoothing means and what kind of effect it causes. To avoid these complications the anisotropic models in this work are restricted to homogeneous and factorised models, which are introduced in section 3.3, although the implementation works for arbitrary anisotropic media.

4.4 Propagation of wavefronts

The propagation of a wavefront is in fact the propagation of single rays with a constant time step (Figure 4.18). The propagation of rays is computed according to the kinematic ray-tracing system (2.28). The KRT system is a system of six ordinary differential equations. The numerical solution of this system is performed by integration methods.

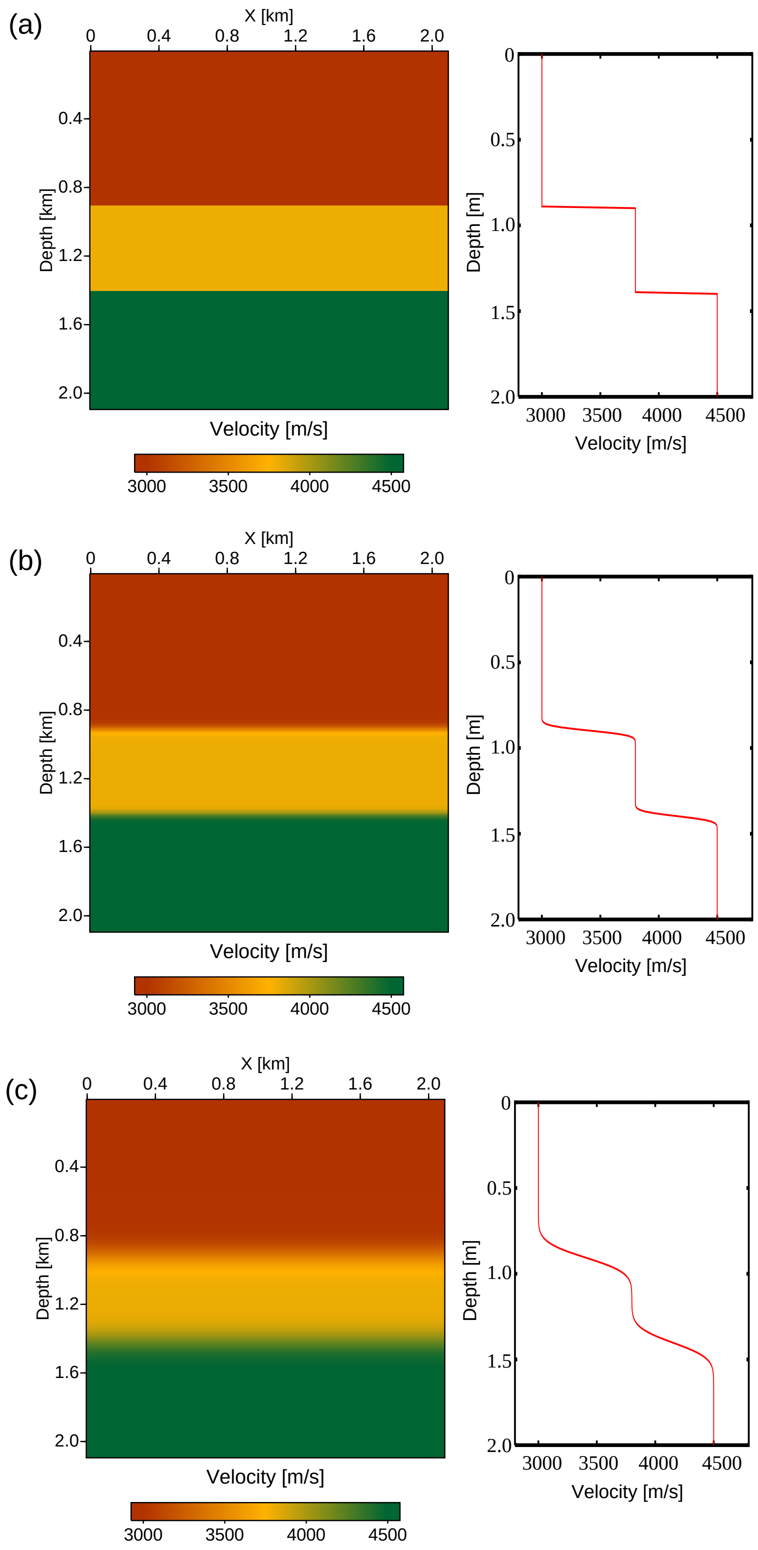

Figure 4.17: (a) Original velocity model; (b) Smoothed model (10-fold); (c) Smoothed model (100-fold).

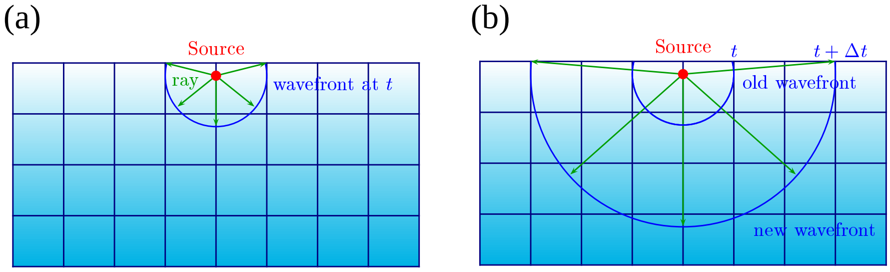

Figure 4.18: The propagation of the wavefront is in fact the propagation of individual rays with a constant traveltime step. A new wavefront (b) is constructed from the old one (a) by propagating the ray field with a constant traveltime step Δt.

By far the most often used method to integrate the ray tracing equation is the classical fourth-order Runge-Kutta formula. Runge-Kutta methods propagate the ray over a traveltime step by combining the information from several smaller Euler-style steps where the derivative at the starting point of each interval is extrapolated to find the next function value. In each step derivatives are calculated four times (see also Figure 4.19): once at the initial point (1), twice at trial midpoints (2,3), and once at a trial endpoint (4).

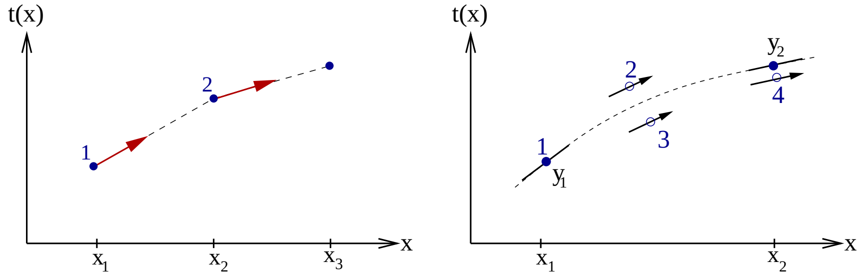

Figure 4.19: Left: Euler's method: the derivative at the starting point of each interval is extrapolated to find the next function value. Right: fourth-order Runge-Kutta method: in each step the derivative is evaluated four times.

From these derivatives the final function value (t) is calculated. Details about integration methods can be found in many books on numerical mathematics (e.g. Press et al., 1992). Each new wavefront is constructed from the old one by propagating the ray field with a constant traveltime step. After each time step the wavefront-oriented ray tracing

- checks the ray density and if necessary inserts a new ray, and
- interpolates the traveltimes from the wavefronts onto the rectangular grid.

4.5 Insertion of a new ray

To guarantee a sufficient illumination by rays along the wavefront, sometimes new rays have to be inserted. The implementation of wavefront-oriented ray tracing follows the insertion criteria proposed by Coman (2003):

1. The distance between two adjacent nodes (intersection points between rays and wavefronts) exceeds a predefined distance Δr.

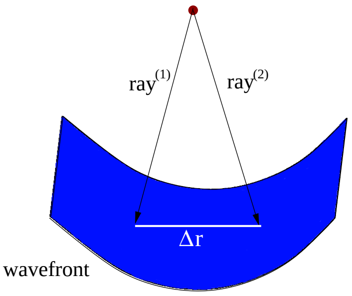

2. The difference in wavefront curvature at adjacent nodes exceeds a predefined value and the distance between the nodes is larger than a predefined distance Δr_1.

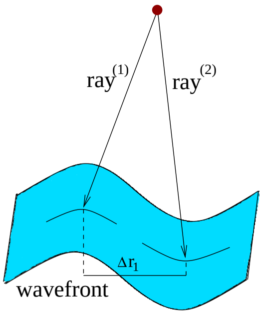

3. One ray in the cell crosses the surface defined by the other two adjacent rays and the distance between the nodes is larger than Δr_1.

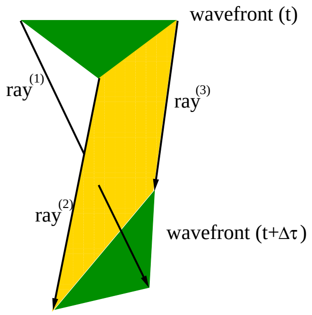

The first criterium is the “traditional” one, where a new ray is inserted, if the distance between neighbouring rays exceeds a predefined distance Δr. This criterium avoids undersampling of small-scale velocity anomalies. The other two criteria are mainly important in caustic regions. To prevent oversampling in these regions a new ray is inserted only if the distance between two rays is larger than Δr_1. For a more detailed explanation of the insertion criteria see Coman (2003).
Usually the coordinates of the new ray are interpolated onto the wavefront. Coman (2003) suggest the insertion of a new ray by tracing the ray directly from the source. The initial conditions of the new ray are given by the known source position and the bisector of the angles between the two “parent rays”. Thus, the accuracy retains unchanged by the insertion of a new ray. In addition this concept allows a lower ray density which applies larger cells.

As already mentioned the 3-D wavefronts are represented by a network of triangles (see figure 4.2). The insertion of new rays increase the number of triangles (see Figure 4.20). Depending on how many new rays are inserted, the “old” triangle might be split into two, three or four new triangles.

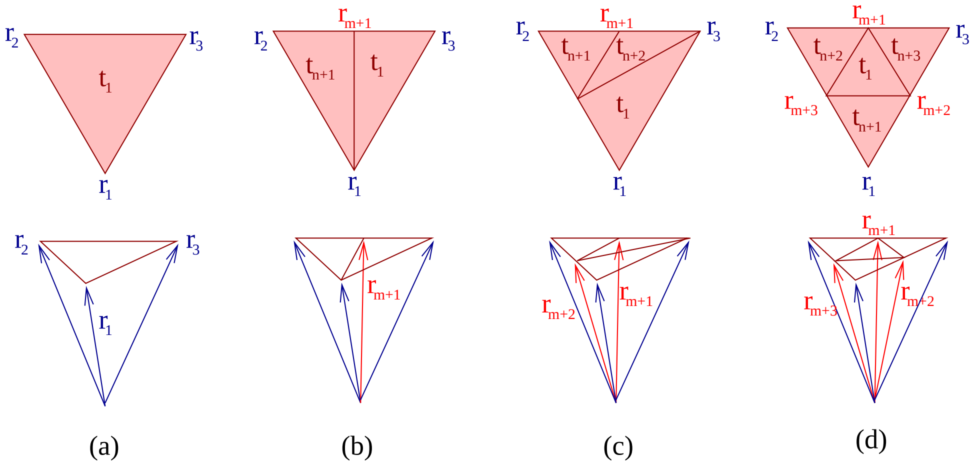

Figure 4.20: The insertion of new rays increase the number of triangles to describe the 3-D wavefront. An “old” triangle might be split into two (b), three (c) or four (d) new triangles.

4.6 Interpolation of traveltimes

The wavefront-oriented ray tracing provides the traveltimes on wavefronts. Because most applications, e.g. migration, need the traveltimes on grids an interpolation to the grid nodes becomes necessary. The traveltimes are interpolated after each time step in the region between the new and the old wavefront (see Figure 4.21). This has the advantage that only the present and the previous wavefront have to be stored.

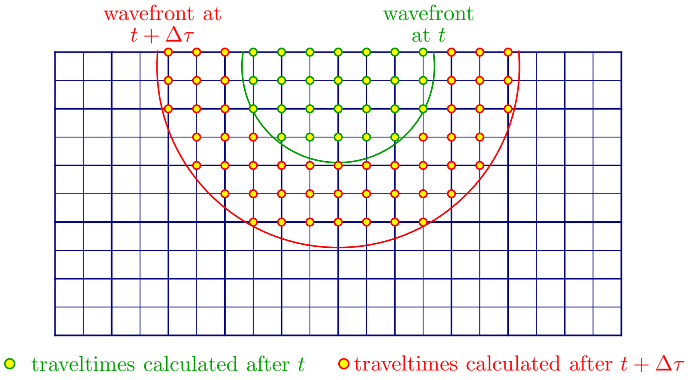

Figure 4.21: After each time step the traveltimes between the new and the old wavefront are interpolated to grid points. The red dots are the positions where the traveltimes are calculated after $t + \Delta\tau$, and the traveltimes at the green dots are already known from the step before.

In Figure 4.21 two wavefronts are shown, the present one (red) and the previous one (green). The traveltimes are interpolated to all grid points which are between these two wavefronts. The wavefront-oriented ray tracing for anisotropic media uses the distance-weighted traveltime interpolation introduced by Coman (2003). The general concept of the traveltime interpolation will be explained the 2-D case, before describing the more complex 3-D situation.

2-D case

The interpolation of traveltimes to grid points is carried out within cells. To define a ray cell, rays and wavefronts will be approximated by straight lines. Thus, the boundaries of a ray cell are two adjacent linearised ray segments and two adjacent linearised wavefront segments (see e.g. Figure 4.22). After defining a ray cell, all grid points have to be detected that are located within this cell. In terms of efficiency the searching area will be limited by a rectangular area around the ray cell (see Figure 4.22(a)).

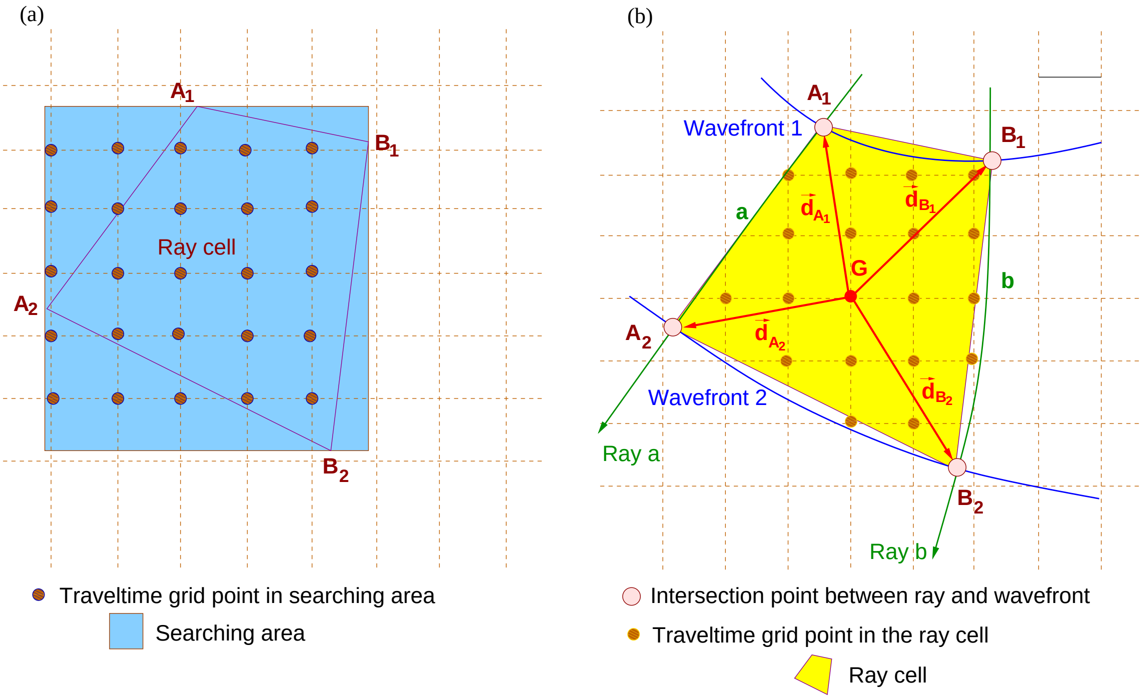

Figure 4.22: Points A_1 and B_1 indicate ray end points on the wavefront with traveltime τ and points A_2 and B_2 correspond to ray end points on the wavefront with traveltime $\tau + \Delta\tau$. (a) To limit the searching area, a rectangular region surrounding the ray cell is defined. (b) Vectors $\vec{d}_{x_n}$ are distance vectors of the grid point under consideration from the ray end point x_n. By the vector products $\vec{d}_{A_1} \times \vec{d}_{B_1}$, $\vec{d}_{B_1} \times \vec{d}_{B_2}$, $\vec{d}_{B_2} \times \vec{d}_{A_2}$, and $\vec{d}_{A_2} \times \vec{d}_{A_1}$ it is checked if the grid point G is inside the ray cell A_1, A_2, B_1, B_2.

To decide if a grid point is inside or outside the cell, the implementation uses the approach introduced by Ettrich and Gajewski (1996). They connected the grid point to every node

by a vector and perform the vector products $\vec{d}_{A_1} \times \vec{d}_{B_1}$, $\vec{d}_{B_1} \times \vec{d}_{B_2}$, $\vec{d}_{B_2} \times \vec{d}_{A_2}$, and $\vec{d}_{A_2} \times \vec{d}_{A_1}$. The grid point is inside the cell if the signs of all resulting vector products are the same. If the grid point is located inside the cell, the traveltime will be interpolated.
Figure 4.23 shows the distances which are used for the calculation of traveltimes within a ray cell in a 2-D media. The traveltime τ_G at grid point G is calculated by:

$$\tau_G = w_{a1}\tau_{a1} + w_{a2}\tau_{a2} + w_{b1}\tau_{b1} + w_{b2}\tau_{b2}, \tag{4.12}$$

where, e.g. τ_{a1} is the traveltime to G interpolated from node A_1 and w_{a1} is the corresponding distance weight. The detailed description of how the weights are calculated from the distances d_1, d_2, d_a, d_b is given by Coman (2003).

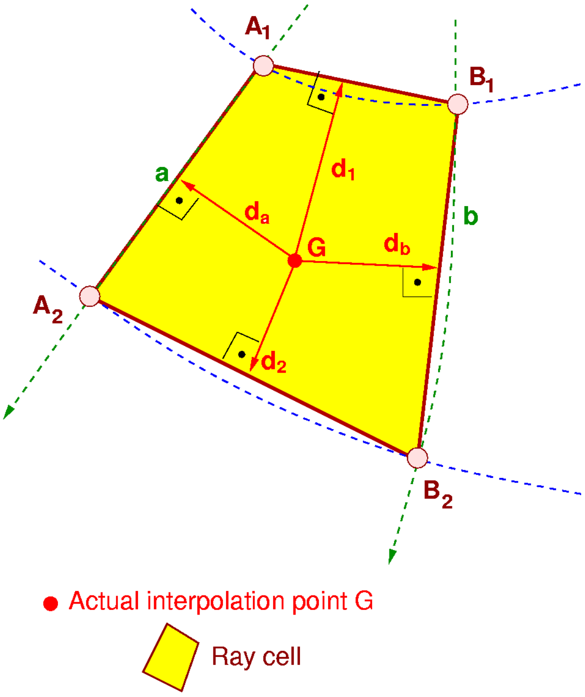

Figure 4.23: For a grid point G within the cell the distances d_1, d_2, d_a, d_b are used for the computation of the distance weights required for the traveltime interpolation.

Figure 4.24 shows how the wavefront curvature at node A_1 is approximated by using the slowness vector at this node and the position of the nodes A_1 and the adjacent node on the same wavefront B_1. The intersection point between the normal to the segment $\overline{A_1B_1}$ at M and the backward continuation of the slowness vector $\vec{p}$ at A_1 define the center of the circle which passes the nodes A_1 and B_1. The radius of this circle R is assumed to be radius of the wavefront curvature at node A_1. Therefore, the traveltime τ_{a_1} from the node A_1 to the grid point G can approximated by:

$$\tau_{a_1} = \tau_{A_1} + \frac{|\overline{GG'}|}{\frac{1}{2}(v_G v_{G'})}, \tag{4.13}$$

where τ_{A_1} is traveltime at node A_1, G' is the projection of point G on the approximated wavefront with the radius R, $\overline{GG'}$ is the distance between G and G', v_G is the velocity at point G and the velocity at G' is given by $v_{G'}$. The interpolation of traveltimes from the other three nodes to the grid point G is similar.

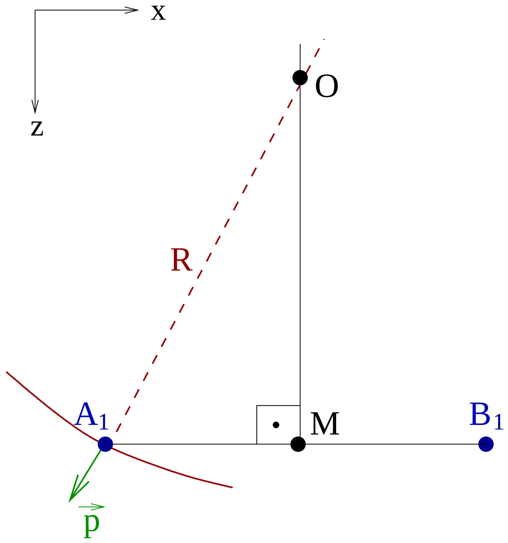

Figure 4.24: Approximation of the wavefront curvature at node A_1. Point M is the midpoint of the segment $\overline{A_1B_1}$ and point O represents the centre of the circle which passes the nodes A_1 and B_1. Point O is obtained by the intersection of the backward extension of the slowness vector $\vec{p}$ at A_1 and the normal to the segment $\overline{A_1B_1}$ at M. The radius of the wavefront curvature at node A_1 is approximated by the distance $|\overline{OA_1}|$.

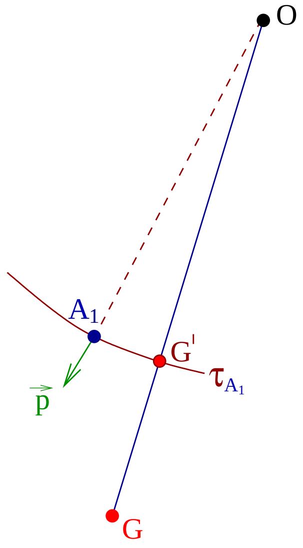

Figure 4.25: Interpolation of the traveltimes from node A_1 to the grid point G. The point G' is the projection of the grid point G onto the circular wavefront that passes the node A_1.

If the medium is anisotropic we have to distinguish phase and group velocity. In the anisotropic implementation in equation 4.13 the phase velocity is used.

3-D case

To decide whether a grid point is within a 3-D cell, which is bounded by the two wavefronts and three rays (Figure 4.26), the cell is decomposed into three tetrahedra.

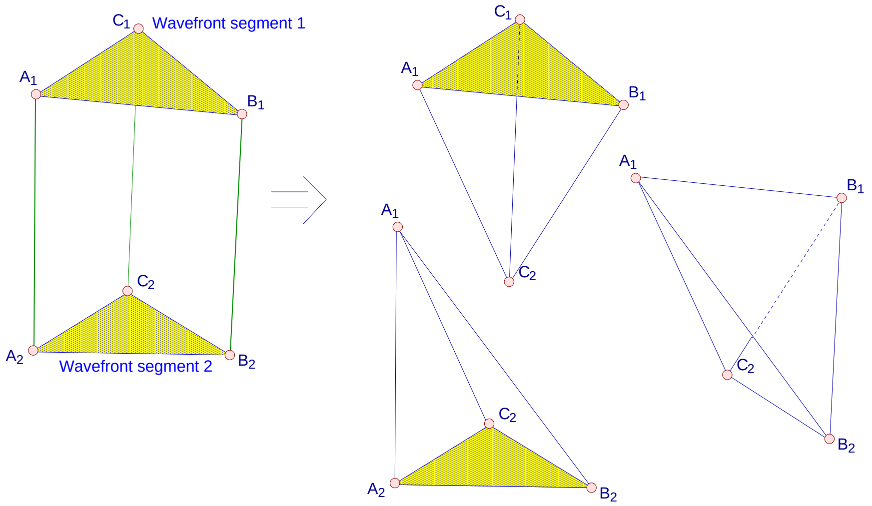

Figure 4.26: Decomposition of a ray cell into three tetrahedra.

The decision whether a grid point is inside a ray cell is performed by testing if this grid point is within one of the three tetrahedra. The position of a grid point with respect to a tetrahedron is well-defined. For instance, a grid point G is within the tetrahedron $A_1B_1C_1C_2$ if, for each plane defined by three points of the tetrahedron, the point G is in the same half-space as the fourth point of this tetrahedron (see Figure 4.27). As half-space we considers the spaces separated by the plane under consideration. Similar to the 2-D case, the interpolated traveltimes from nodes to grid points use the wavefront curvature at this nodes. In 2-D, the wavefront is represented by a curve and the wavefront curvature at nodes is approximated by a circle. In 3-D, the wavefront is represented by a surface. The curvature of this surface will be approximated by two curvatures, which are estimated in two normal sections at the node. The normal section at node A_1 in the direction of B_1 (Figure 4.28(a)) is the intersection of a normal plane with the surface. This normal plane is defined by the normal to the surface at point A_1 and point B_1. The interpolated traveltime from node A_1 to the grid point G with respect to the normal plane in the direction of B_1 is denoted by $t_{a1\beta}$ and can be calculated by equation (4.13). In contrast, $t_{a1\gamma}$ represents the interpolated traveltime from node A_1 to the grid point by approximating the wavefront curvature in the normal plane in the direction of node C_1 (see Figure 4.28(b)).

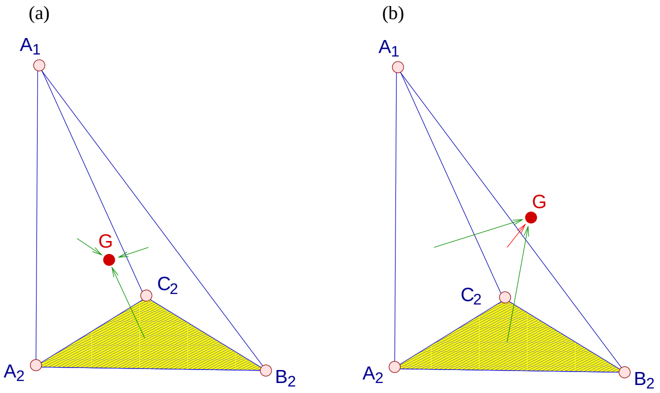

Figure 4.27: For each plane defined by three points of the tetrahedron, the point G (a) is in the same half-space as the fourth point of this tetrahedron; or (b) if the grid point is not located within the tetrahedron, the point G is for plane $A_1B_2C_2$ not in the same half-space as the fourth point A_2.

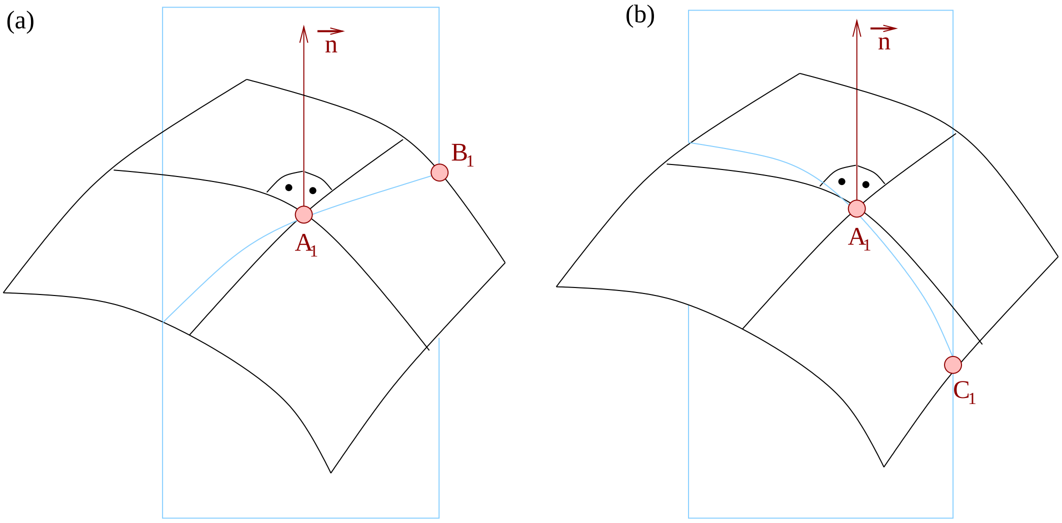

Figure 4.28: The surface of a wavefront in the vicinity of a node A_1. (a) The normal section at node A_1 in the direction of node B_1 is the intersection of a normal plane with the surface. (b) Here, the normal plane is defined by the normal to the surface at point A_1 and point B_1 and the normal section is the intersection between this normal plane and the surface.

Thus, the traveltime t_G at the grid point G is interpolated by the weighted average of the twelve interpolated traveltimes:

$$\begin{aligned} t_G &= w_{a1\beta}t_{a1\beta} + w_{a1\gamma}t_{a1\gamma} + w_{b1\alpha}t_{b1\alpha} + w_{b1\gamma}t_{b1\gamma} + w_{c1\alpha}t_{c1\alpha} + w_{c1\beta}t_{c1\beta} \\ &+ w_{a2\beta}t_{a2\beta} + w_{a2\gamma}t_{a2\gamma} + w_{b2\alpha}t_{b2\alpha} + w_{b2\gamma}t_{b2\gamma} + w_{c2\alpha}t_{c2\alpha} + w_{c2\beta}t_{c2\beta}. \end{aligned} \tag{4.14}$$

Each weight can be expressed as a function of three distances (see also Figure 4.29):

- The distance between the grid point and the linear ray segment, e.g., d_a

- The distance between the grid point and the lateral plane, e.g., d_β
- The distance between the grid point and the triangular base, e.g., d_1

For more details about the interpolation and for the solution in the boundary area of the model see Coman (2003).

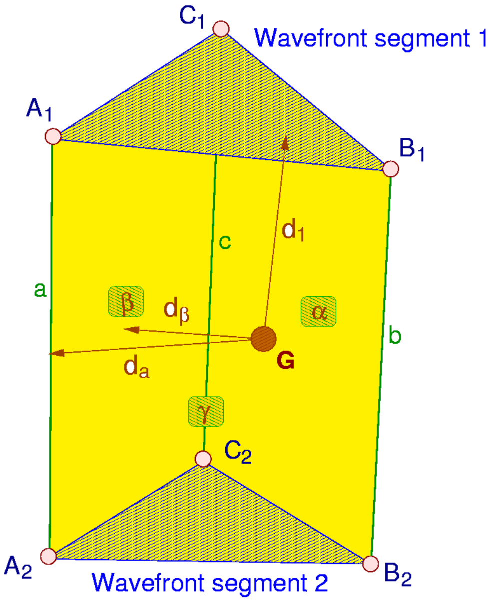

Figure 4.29: 3-D cell and the distances which are used for the traveltime interpolation. The distance between the grid point G and the upper triangular base is denoted by d_1, d_a is the distance between G and the ray segment a and d_β is the distance between G and the side β of the 3-D cell.

In general, the number of arrivals in this implementation is limited to three, mainly motivated by the fact that the spatial distribution of later arrivals is usually small. In case of multivalued arrivals at grid points more than one traveltime value is calculated. In this case the storing is preceded by sorting. The arrivals (1nd, 2nd, 3nd etc.) are sorted with regard to their traveltimes.

Chapter 5

Numerical examples

After introducing the method of wavefront-oriented ray tracing for anisotropic media in the previous chapter, here the accuracy of the proposed technique will be demonstrated. However, the accuracy of the wavefront-oriented ray tracing depends on the accuracy of the ray-tracing procedure, the accuracy of the insertion of new rays, and the accuracy of the traveltime interpolation to grid points.

Since in the presented implementation the forth-order Runge Kutta method is used, the traveltime errors introduced by the numerical integration of the kinematic ray tracing system can be considered to be negligible.

Because a new ray is inserted by tracing the ray directly from the source, the errors due to the insertion of a new ray are the same order as the errors of the parent rays.

As described above for the interpolation of the grid point traveltimes from the traveltimes at nodes, a method of second order is used. The accuracy of this interpolation can be increased by increasing the ray and wavefront density.

To establish the accuracy of the wavefront-oriented ray tracing, several numerical examples are presented in this chapter:

- Elliptically anisotropic model (quasi-compressional (qP) wave, quasi-shear vertical (qSV) wave, shear horizontal (SH) waves)
- Polar anisotropic (qP-wave and quasi-shear (qS) waves)
    - homogeneous model
    - low velocity lens
- Triclinic (qP- and qS-waves)
    - homogeneous model
    - gradient model

Almost all chosen elastic parameters are related to real rocks. For example, in the homogeneous triclinic model I assumed a triclinic sandstone (Mensch and Rasolofosaon, 1997). To demonstrate the accuracy of the method the traveltimes computed for a homogeneous

anisotropic model with elliptical symmetry are compared to exact traveltimes available for this medium.
Since there exists no analytical solution for an inhomogeneous anisotropic model, I compare the results with an alternative method for traveltime computation, the FD perturbation method (Soukina and Kashtan, 2001). To estimate the accuracy of this method compared to wavefront-oriented ray tracing we start with homogeneous models (sections 5.2 and 5.3). The heterogeneous media presented in these sections are factorised anisotropic media (see section 3.3).
To benefit from the task of wavefront construction methods not only first arrivals are presented in this chapter, but also second and third arrivals for a selected model are shown. As already mentioned in the previous chapter the traveltimes are interpolated from wavefronts to grid points. Close to the boundary of a 3D model, where the grid cells are fragmented, this interpolation is less accurate than in the remainder of the model. Because these effects are not related to the algorithm itself, these regions were omitted for the traveltime accuracy analysis. To avoid this loss in accuracy at boundaries would causes much more computational time. Usually the area of interest is located inside the model, therefore we can ignore these boundary effects.

5.1 Elliptically anisotropic medium

A special case of transversely isotropy which assumes the wavefronts to be ellipsoids has been used by Cholet and Richard (1954) and Richards (1960) in accounting for the observed traveltimes at Berraine in the Sahara and in the foothills of Western Canada. For this type of anisotropy the quasi-shear wavefront is forced to be spherical. However, it is instructive to investigate this simple anisotropic model as it incorporates many features inherent to wave propagation in a more general anisotropic medium (Daley and Hron, 1979). The kinematics of this anisotropy type have been treated in a number of papers, e.g., Gassman (1964). A brief overview of the theory for the wave propagation in an ellipsoidally anisotropic medium is given in appendix C. The Thomsen parameters of the example medium are given by

$$\epsilon = \delta = 0.165, \quad \gamma = 0.2, \quad v_{P0} = 3.38\ km/s, \quad v_{S0} = 2.12\ km/s.$$

The given model has 201 grid points in x-direction and 101 grid points in y- and z-direction. The grid spacing is 10 m in each direction. The source point is located in the center of the x-y-plane and 100 m in depth i.e. at (1.0, 0.5, 0.1 km). The exact calculated traveltimes for the qP-wave (equation (C.20) in appendix C) with the corresponding isochrones are shown in Figure 5.1.
The results of the comparison of the exact traveltimes and the traveltimes computed by the wavefront-oriented ray tracing for all wave types are shown in Figures 5.2-5.4.
Figure 5.2 illustrates the relative errors for the qP-wave. The error distribution for the 3-D model is presented by 2-D-slices through the model, one vertical x-z-slice through the source position y=500m and two horizontal slices at z=100m and z=500m. The top figure has a different error scale than the two horizontal slices. As readily identifiable in

the vertical slice the maximum relative error of 0.04% is located near the source. The relative errors near the source appear exaggerated since there the traveltimes themselves are very small. Due to the fact that in the remainder of the model the traveltime error is significantly smaller the observed average relative error is only $1.69 \cdot 10^{-3}$%. The lattice-like pattern of the traveltime error which can be observed in all error distributions are originated by the traveltime interpolation to grid points. The absolute traveltime errors for the qP-wave are shown in the top of Figure 5.5. In this case the observed average of the absolute traveltime error is $2.12 \cdot 10^{-3}$ ms. The calculation of the qP-wave therefore has a high accuracy and meets the standard demands of all applications, such as migration.

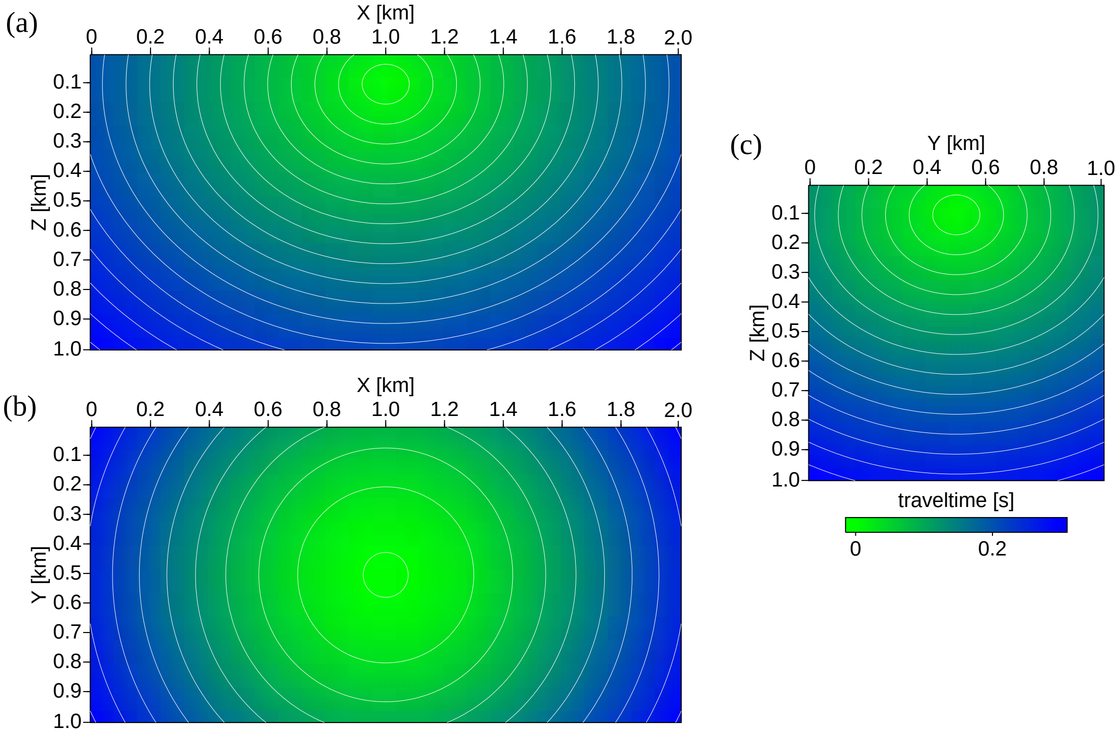

Figure 5.1: Wavefronts for the elliptical anisotropic medium. The underlying colour-scale illustrates the exact traveltimes for the qP-wave. The figures show three different slices of the 3-D model: (a) in the x-z-plane; (b) in the x-y-plane; (c) in the y-z-plane.

Figure 5.3 visualises the relative errors for the computation of the SH-waves. As for the qP-wave the upper figure is generated by using a larger error margin than for the horizontal slices of the traveltime distribution. The magnitude of the traveltime errors are comparable to the qP-wave. The average relative traveltime error for the SH-wave is $7.43 \cdot 10^{-4}$% and the average of the absolute traveltime error is $2.78 \cdot 10^{-3}$ ms. Figure 5.4 shows the relative errors for the computation of the qSV-waves. We find an average of the relative traveltime error for the qSV-wave of $6.25 \cdot 10^{-3}$% and the average absolute traveltime error is $3.05 \cdot 10^{-2}$ ms.

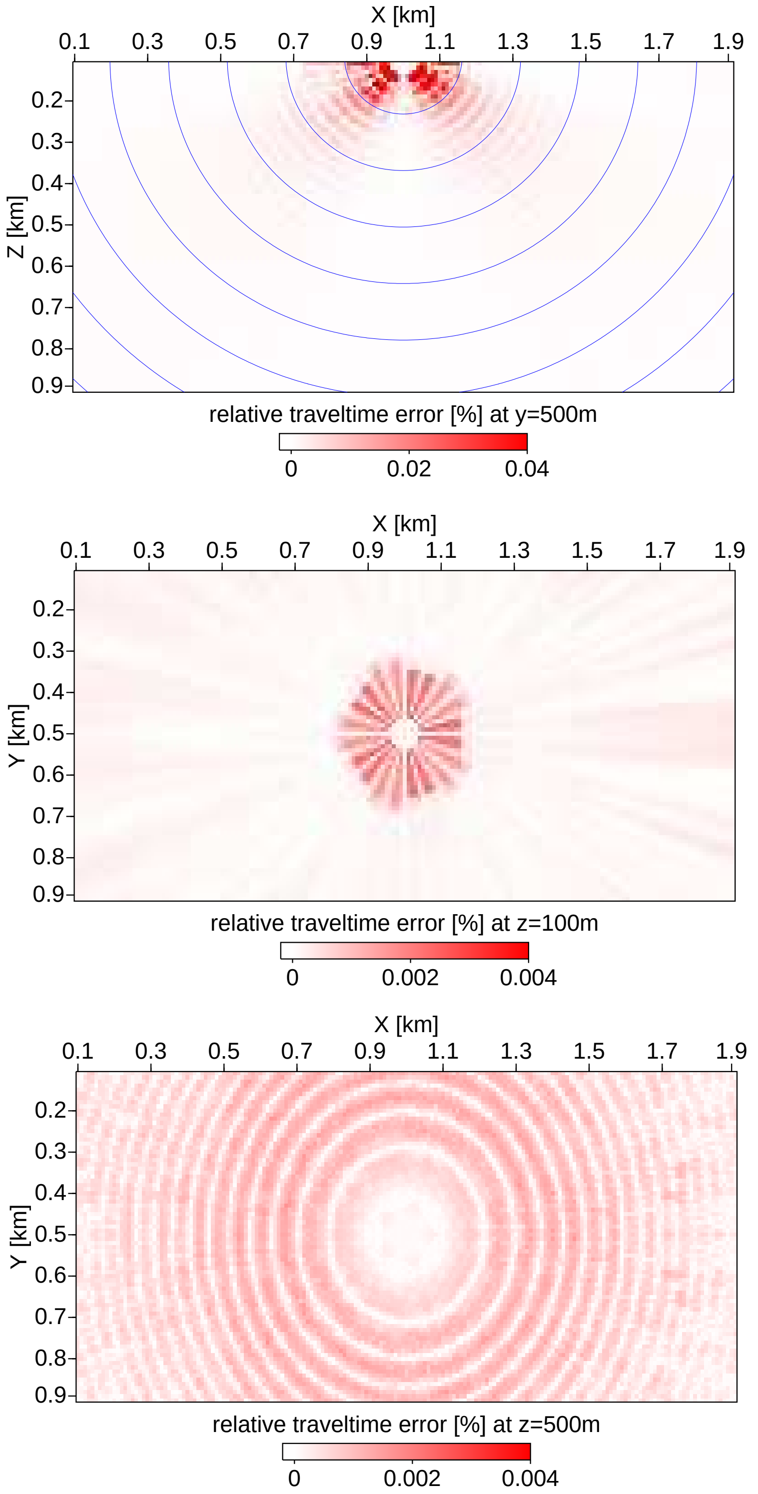

Figure 5.2: Relative errors for the qP-wave in the elliptically anisotropic model. The upper figure shows a x-z-slice through the source; the lower figures are 2-D slices in the x-y plane, one through the source location (z=100 m) and the other at a depth of 500 m. The isochrones in the upper figure are shown in 0.04 s steps. Note the different error scale of the top figure.

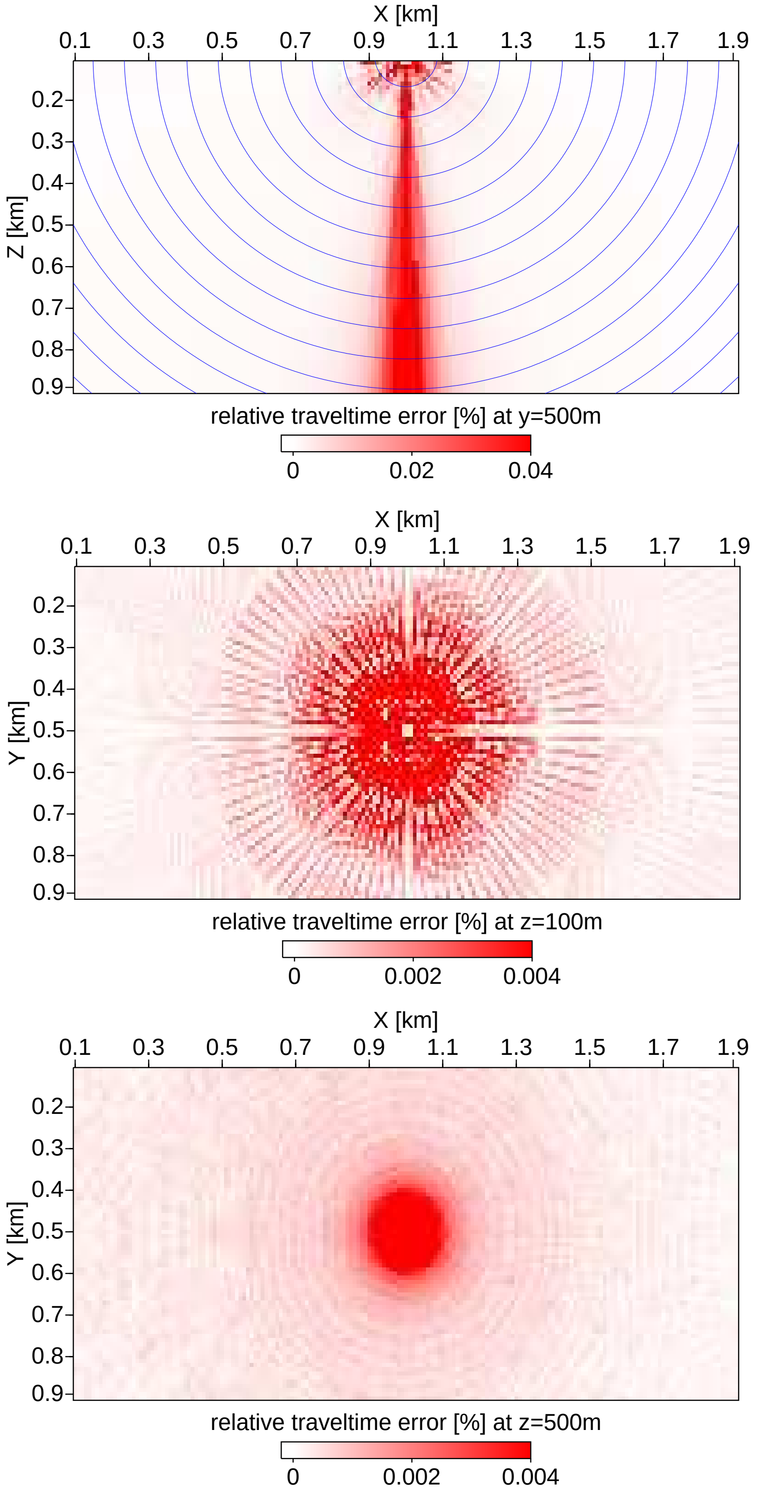

Figure 5.3: Relative traveltime errors for the SH-wave in the elliptically anisotropic model. The upper figure shows a x-z-slice through the source; the lower figures are 2-D slices in the x-y plane, one through the source location (z=100 m) and the other at a depth of 500 m. The isochrones in the upper figure are shown in 0.04 s steps. Note the different error scale of the top figure.

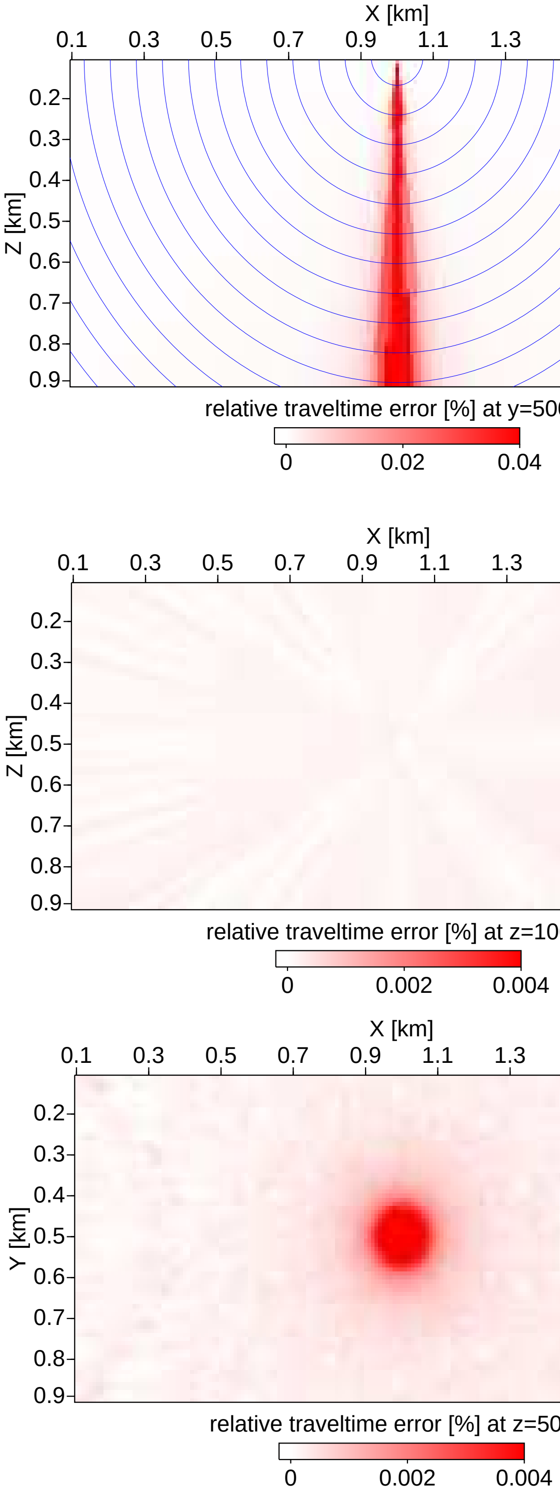

Figure 5.4: Relative traveltime errors for the qSV-wave in the elliptically anisotropic model. The upper figure shows a x-z-slice through the source; the lower two figures are 2-D slices in the x-y plane, one through the source location at 100 m and the other at a depth of 500 m. The isochrones in the upper figure are shown in 0.04 s steps. Note the different error scale of the top figure.

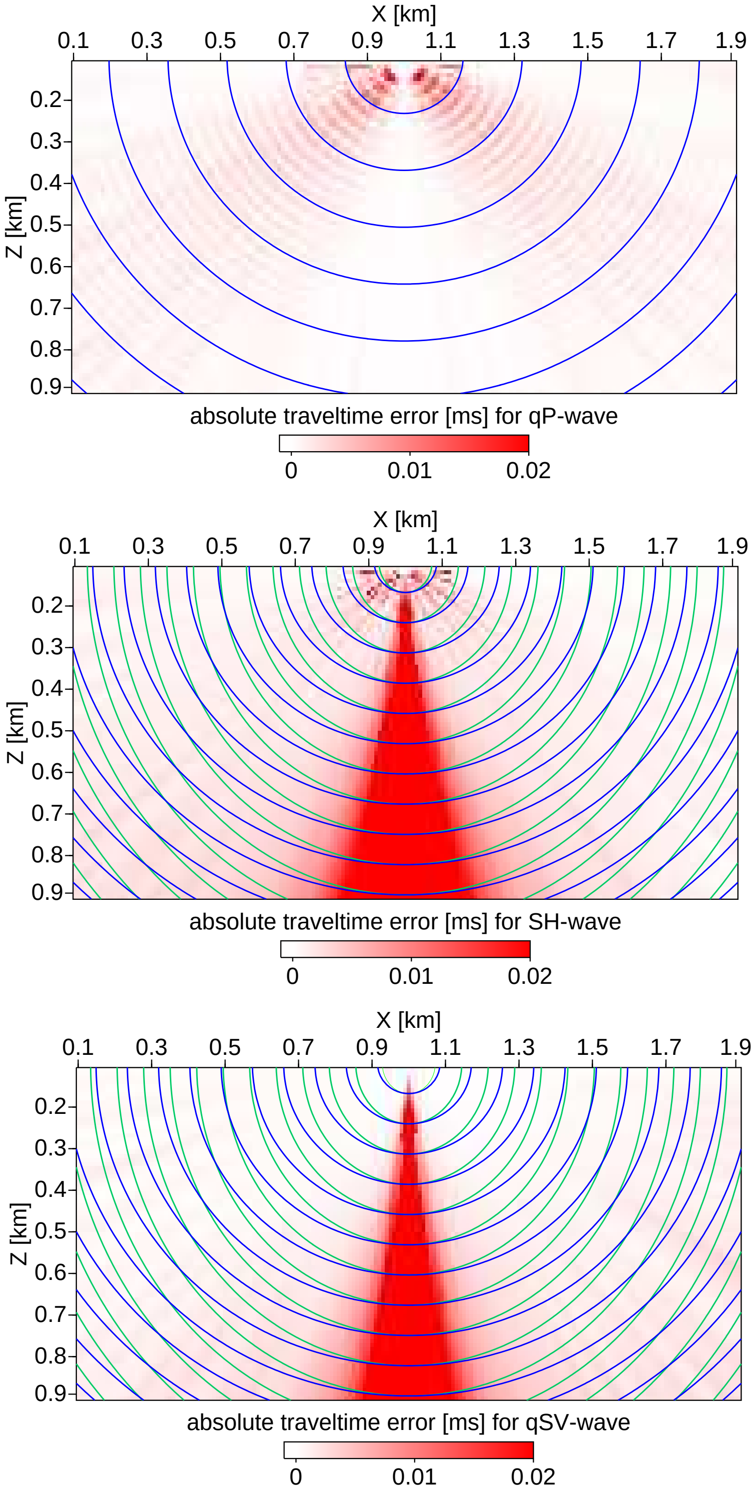

Figure 5.5: Absolute traveltime errors in the elliptically anisotropic model. All figures show a 2-D slice in the x-z-plane. The upper figure represents the error distribution for the qP-wave and the lower figures corresponds to the qSV- and SH-wave. Here the isochrones for the SH-wave are illustrated by the blue lines and the green lines are the isochrones for the qSV-wave.

The cone-shaped region in the error distribution of the shear waves is connected to qS-wave coupling. Here, the SH- and the qSV-wave cannot be treated as two independent waves and some formulas of the ray theory fail, e.g. the ray tracing system (2.28), where the D_{jk}/D is an indefinite expression of the type $0/0$. This is the case where two eigenvalues are locally close to each other. In Figure 5.6 the traveltime differences between the shear waves are displayed. The red colour indicates the region where the traveltimes of both shear waves are nearly the same. In Figure 5.5 the isochrones for both types of waves are displayed. The green lines present the SH-wave and the blue lines are the isochrones for the qSV-wave. In the vertical directions the highest traveltime errors correspond to the region where the isochrones overlap each other. Here, the wavefront-oriented ray-tracing techniques, as other methods based on zero-order ray theory, cannot calculate traveltimes for the qS-waves.

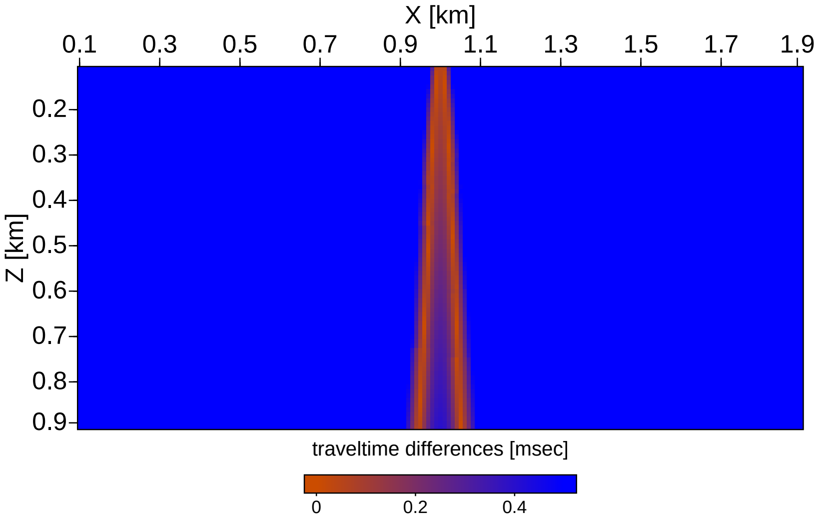

Figure 5.6: Absolute traveltime differences between the SH-wave and the qSV-wave in the elliptically anisotropic model. The figure shows a 2-D slice in the x-z-plane.

5.2 Anisotropic model with polar symmetry

Since no exact traveltimes for a heterogeneous anisotropic medium are available, the calculated qP traveltimes by wavefront-oriented ray tracing are compared with traveltimes obtained by the FD perturbation method (Soukina and Kashtan, 2001). To estimate the error distribution for both methods, we calculate the absolute traveltime error for the corresponding homogeneous model (see Figure 5.7). Thus, the magnitude and distribution of both methods can be quantified and discussed. Subsequently, this knowledge can be used to estimate the accuracy for a heterogeneous model (see Figure 5.14). For the qS-waves no reference traveltimes were available, thus only the results of the traveltime computation by the wavefront-oriented method are presented.

The first example model has polar symmetry and the density normalised elastic parameters are defined by :

$$A_{qp} = \begin{pmatrix} 15.96 & 6.99 & 6.06 & 0.00 & 0.00 & 0.00 \\ & 15.96 & 6.06 & 0.00 & 0.00 & 0.00 \\ & & 11.40 & 0.00 & 0.00 & 0.00 \\ & & & 2.22 & 0.00 & 0.00 \\ & & & & 2.22 & 0.00 \\ & & & & & 4.48 \end{pmatrix} [km^2/s^2].$$

The Thomsen's parameters of this anisotropic shale are $\epsilon = 0.143$, $\gamma = 0.508$ and $\delta = -0.075$. We consider a model cube of $100 \times 100 \times 100$ grid points. The grid spacing is 10 m in each direction. The source is located in the center of the x-y plane and at a depth of 100m at the position $(0.5, 0.5, 0.1\text{km})$.

Traveltime calculation for the qP-wave

For both methods Figure 5.7 display one vertical slice of the absolute traveltime error distribution computed for the qP-wave.

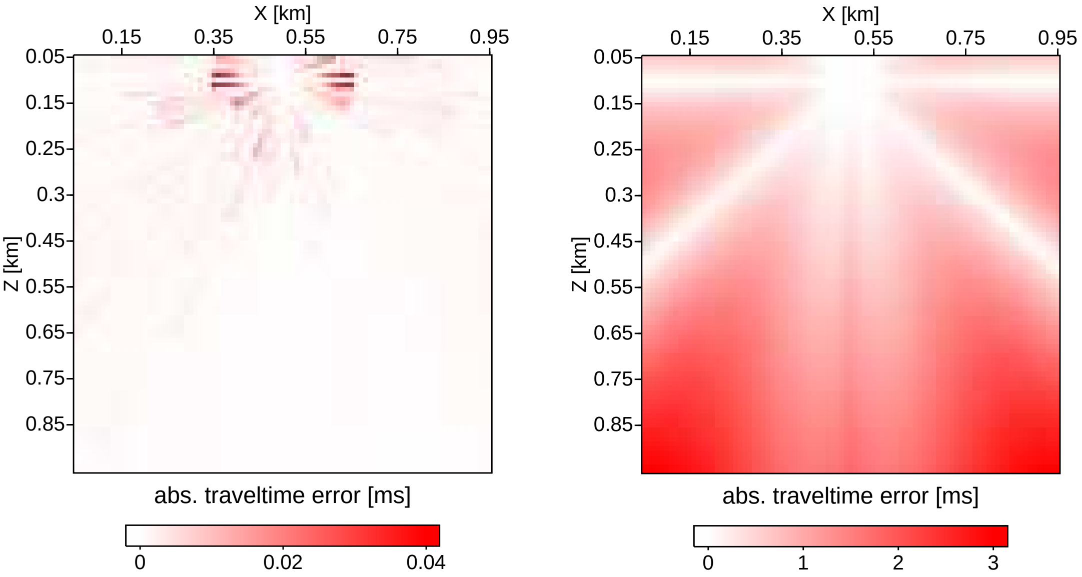

Figure 5.7: Absolute traveltime error for the qP-wave in the anisotropic homogeneous model with polar symmetry, both figures show a x-z slice at y=500m representing the error distribution for the different methods. Left: wavefront-oriented ray tracing. Right: FD perturbation method. Please note the different error scales.

The maximum of the absolute traveltime error for the wavefront-oriented ray tracing, 0.04ms, is located in the source region. The traveltime errors of the wavefront-oriented ray-tracing technique are due to the interpolation to the traveltime grid. Therefore, the traveltime error distribution has that lattice-like pattern. The comparison of the whole 3D model leads to an observed absolute traveltime average error of 10^{-3}ms. In comparison the right side in Figure 5.7 show the absolute traveltime errors of the FD perturbation method (Soukina and Kashtan, 2001). The traveltimes calculated by this method show a typical error distribution of the Vidale scheme. The FD perturbation method accumulates the traveltime errors with increasing distance from the source location. Therefore, in this case the maximum of the traveltime error (3ms) is located near the boundaries of the model. In addition, for this model the traveltime errors depend on direction of propagation. Before this knowledge can be used for an inhomogeneous model with the same type of anisotropy, the results of the comparison between exact traveltimes and traveltimes computed by wavefront-oriented ray tracing are shown in Figure 5.8. As expected the maximum relative error of 0.11% is located near the source position. The average relative error is $1.15 \cdot 10^{-3}\%$. The horizontal slice in 500 m depth demonstrates that for this homogeneous model the traveltime calculation by the wavefront-oriented ray tracing technique yields only randomly distributed round off errors. Again the lattice-like pattern due to the traveltime interpolation from wavefronts to grid points are visible.

Traveltimes of the qS-waves

To investigate the potential of the wavefront-oriented ray tracing technique to calculate traveltimes for qS-waves, no reference traveltimes are available. Therefore, in this part only the calculated results are shown and discussed. To compute both qS-waves for this homogeneous transversely isotropic medium the source location is moved to the center of the model $(0.5, 0.5, 0.5)$km. The main reason for this approach is that in this case the symmetric behaviour of the wave propagation is easier to verify.

The left side in Figure 5.9 images the different phase velocities. The red curve represent the phase velocity of the qP-wave, which is significantly separated from the qS-waves. The qSV-wave (indicated by the green curve) and the qSH-wave (indicated by the blue curve) crosses each other. The wavefront-oriented ray tracing technique assumed that the three wave types have different properties, particularly different velocities of propagating. As described in section 2.6 the initial conditions in anisotropic media specify the type of wave that is to be computed. The right-hand side of Figure 5.9 displays the separation of two qS-wave due to the phase velocity. Here, the green line represents the faster qS1-wave, whereas the phase velocity for the slower qS2-wave is indicated by the blue line. Figure 5.11 shows the results of the traveltime computation by the wavefront-oriented ray tracing for the faster qS-wave. The underlying colour scale images the computed traveltimes and the green curves are the corresponding isochrones. It is readily identifiable that the shape of the isochrone is similar to the green curve in the right-hand side of Figure 5.9. Obviously the isochrones for the slower qS-wave, which are displayed in Figure 5.12, correspond to the blue line in the right-hand side of Figure 5.9.

By plotting the computed isochrones for both qS-waves in one Figure 5.10 it is clearly visible that for this anisotropic model the correct separation of the qS-waves fails.

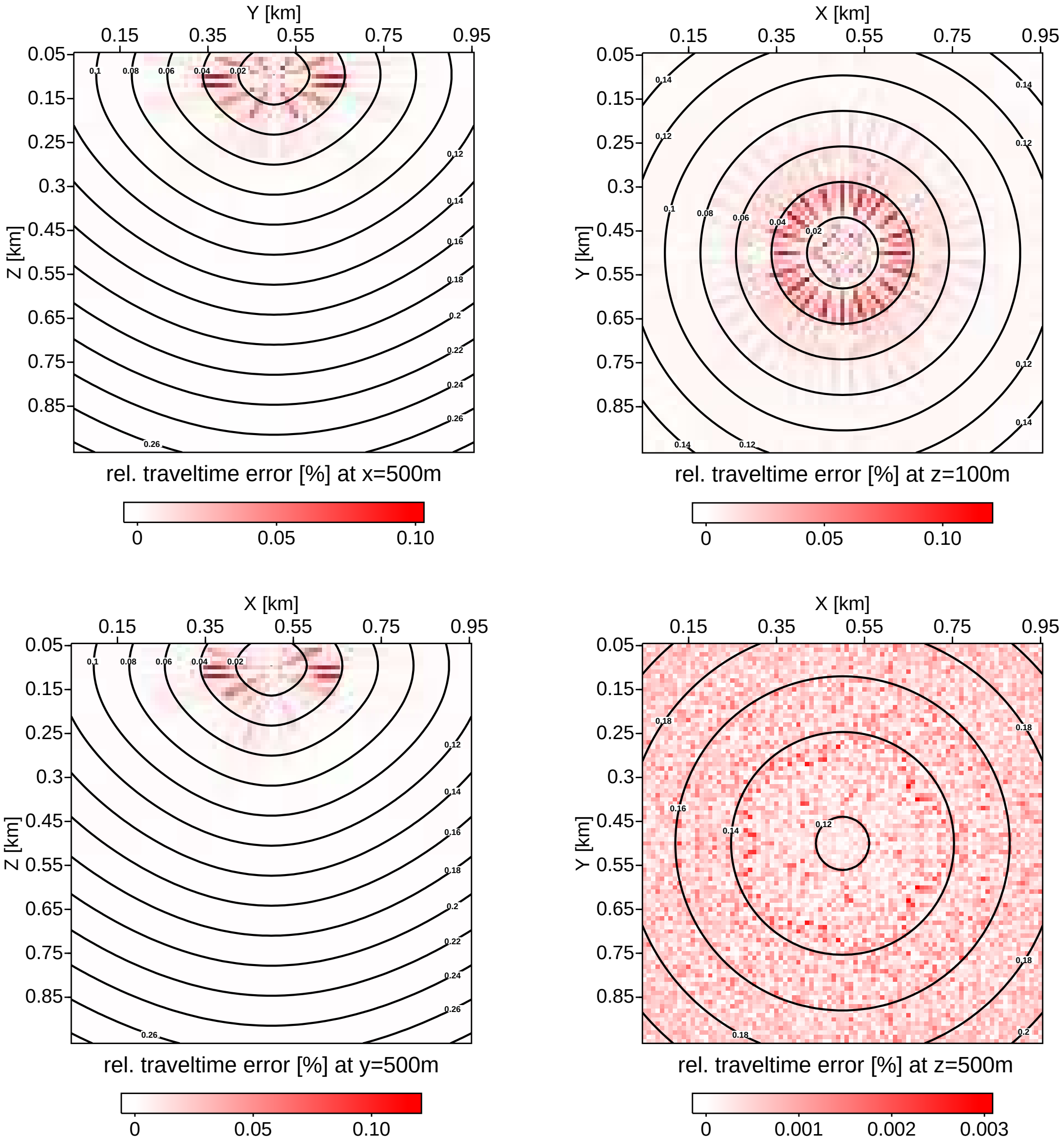

Figure 5.8: Wavefronts for the qP-wave in the anisotropic model with polar symmetry. The source is located in the center of the x-y-plane and in 100m in depth. The figures on the left side show vertical slices through the source position. The figures on the right side show horizontal slices at two different depths (100 m and 500 m).

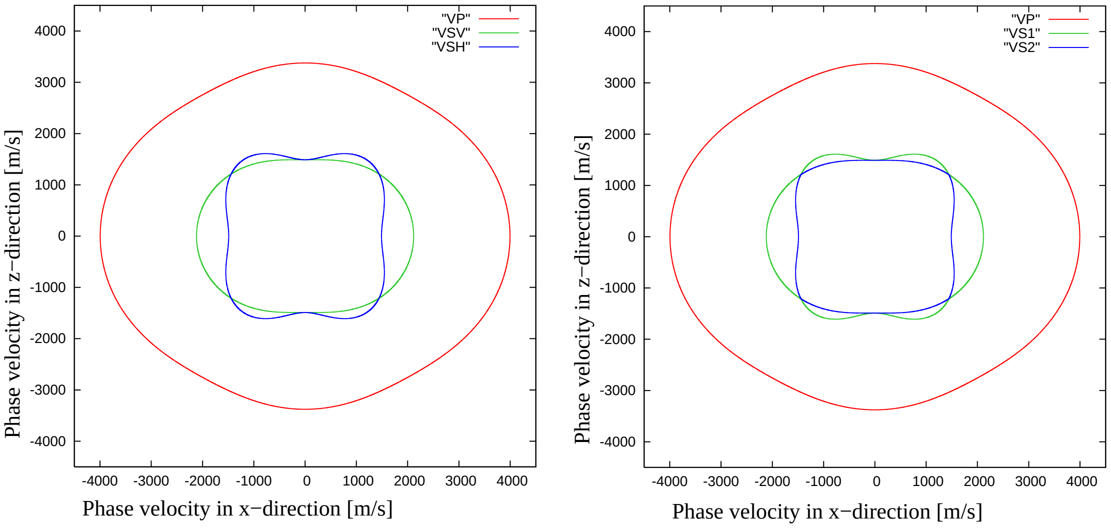

Figure 5.9: Left: Phase velocity for the three propagating wave-types, qP, qSH and qSV. Right: Type of wave separated due to the phase velocity qP, qS1 and qS2.

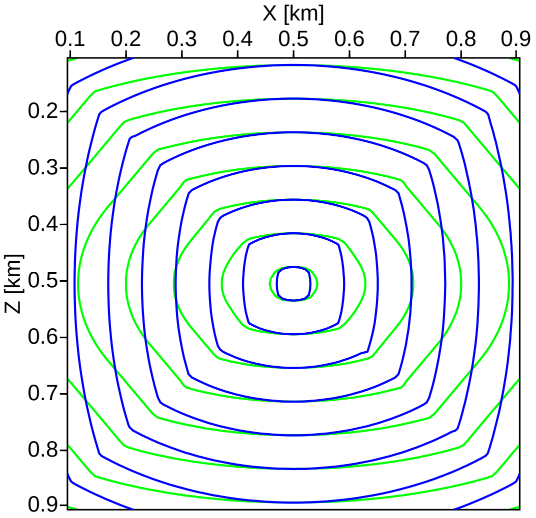

Figure 5.10: Isochrones for both qS-waves computed by the wavefront-oriented ray tracing technique. The green lines indicate the faster qS1-wave and the blue isochrones correspond to the slower qS2-wave.

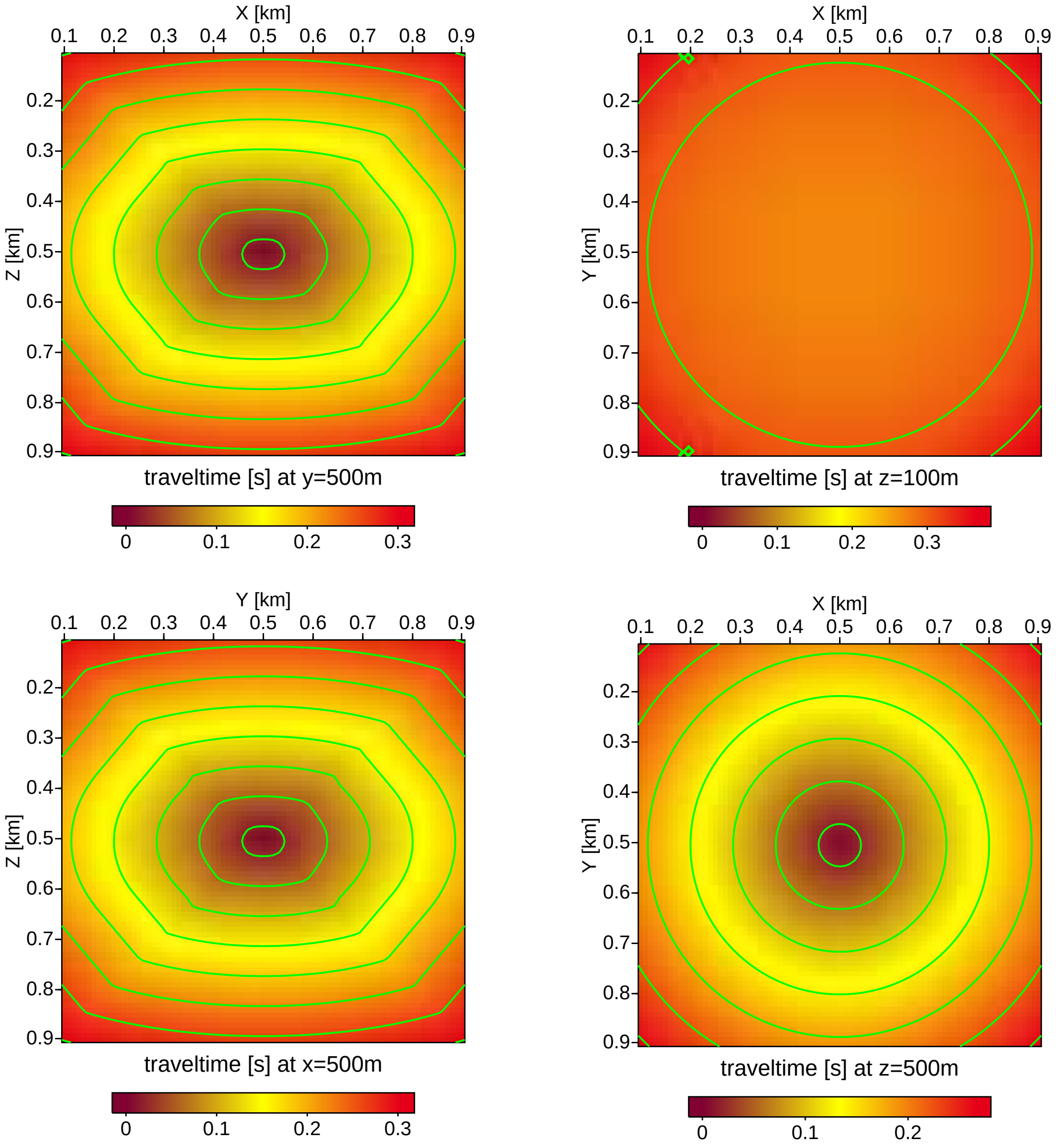

Figure 5.11: Wavefronts for the qS1-wave in the anisotropic model with polar symmetry. The source is located in the center of the model $(0.5, 0.5, 0.5)$km. The figures on the left side show vertical slices through the source position. The figures on the right side show horizontal slices at two different depths (100 m and 500 m).

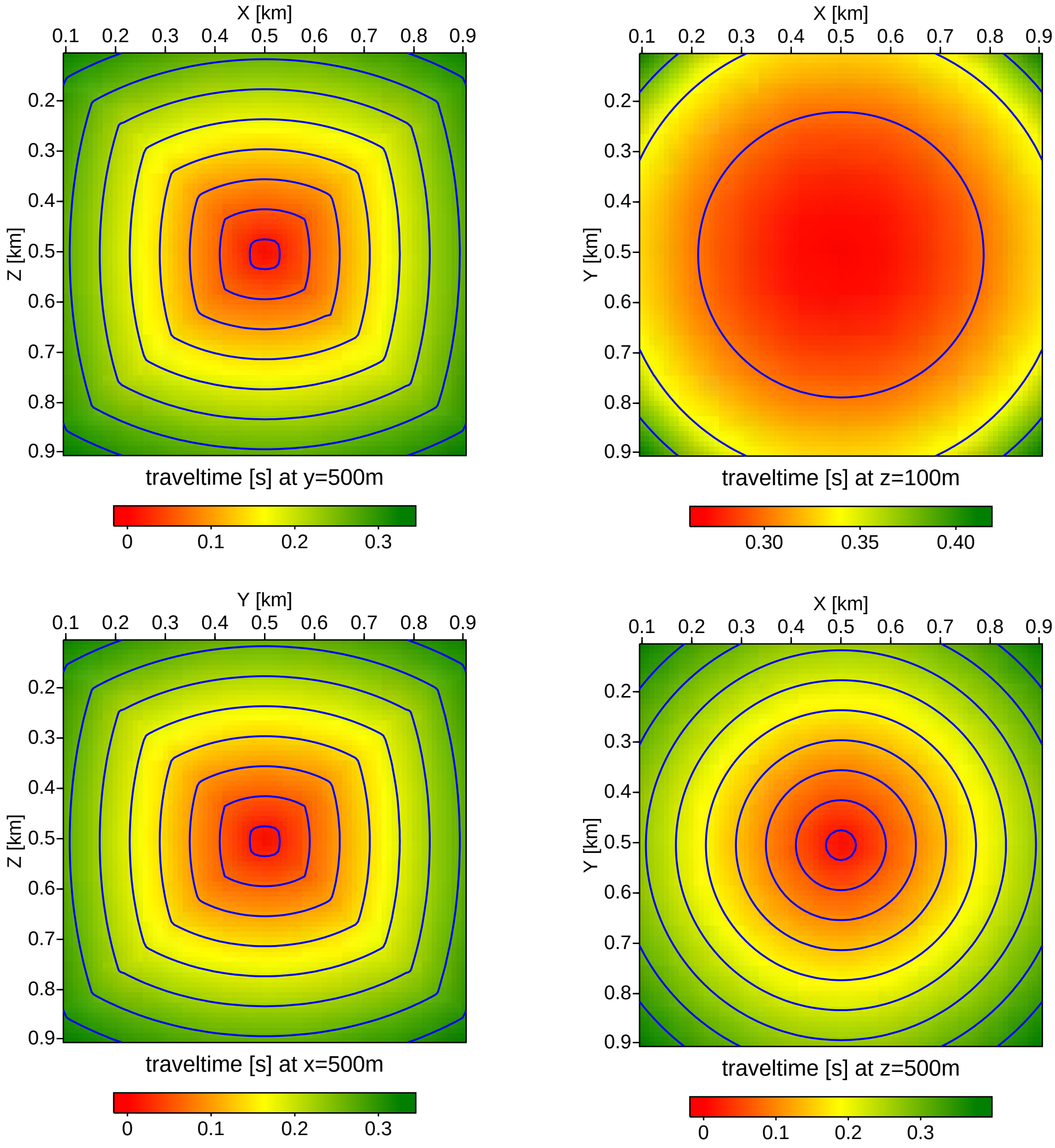

Figure 5.12: Wavefronts for the qS2-wave in the anisotropic model with polar symmetry. The source is located in the center of the model $(0.5, 0.5, 0.5)$km. The figures on the left side show vertical slices through the source position. The figures on the right side show horizontal slices at two different depths (100 m and 500 m).

In conclusion, the computed traveltimes for the qS-waves look reasonable, but the separation in the specific model fails.

I now consider the result about the error distribution for both methods to assess the quality of the implementation for traveltimes in a heterogeneous anisotropic model with polar symmetry.

Factorised anisotropic model with polar symmetry

As an inhomogeneous anisotropic example we use a factorised anisotropic medium (FAI). To construct a FAI we multiply the elastic parameters by an individual factor for each grid point (see also section 3.3). The elastic parameters are the same as in the previous paragraph. The factor-field for the polar symmetry vary smoothly from 3 to 5 and form a parabolic lens (see Figure 5.13).

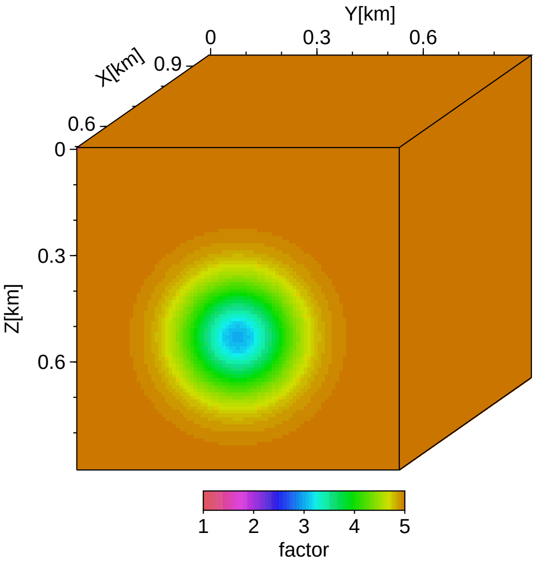

Figure 5.13: Factor field for the heterogeneous anisotropic medium.

For this type of heterogeneity the wavefronts triplicate, which leads to caustics. Therefore, this factor-field is used in section 5.4 to analyse the potential of the wavefront-oriented ray tracing technique for traveltime computation in these regions.

The result of the traveltime comparison is displayed in Figure 5.14. The figure shows four different slices through the 3-D model. On the left hand side, two vertical slices are shown, and the right hand side presents two horizontal slices at different depth. Wavefronts computed from wavefront-oriented ray tracing and FD perturbation method are shown, the black lines indicate the results of the wavefront-oriented ray-tracing method, and the red dotted line the wavefronts calculated by the FD perturbation method. The underlying green scale illustrates the traveltime differences between both methods. The error distribution looks similar to the homogeneous case of the FD perturbation method, and the magnitude of the observed differences are comparable to the homogeneous example as well. Therefore, we assume that the traveltimes calculated by the wavefront-oriented ray tracing are in the same accuracy range as in the homogeneous case shown before.

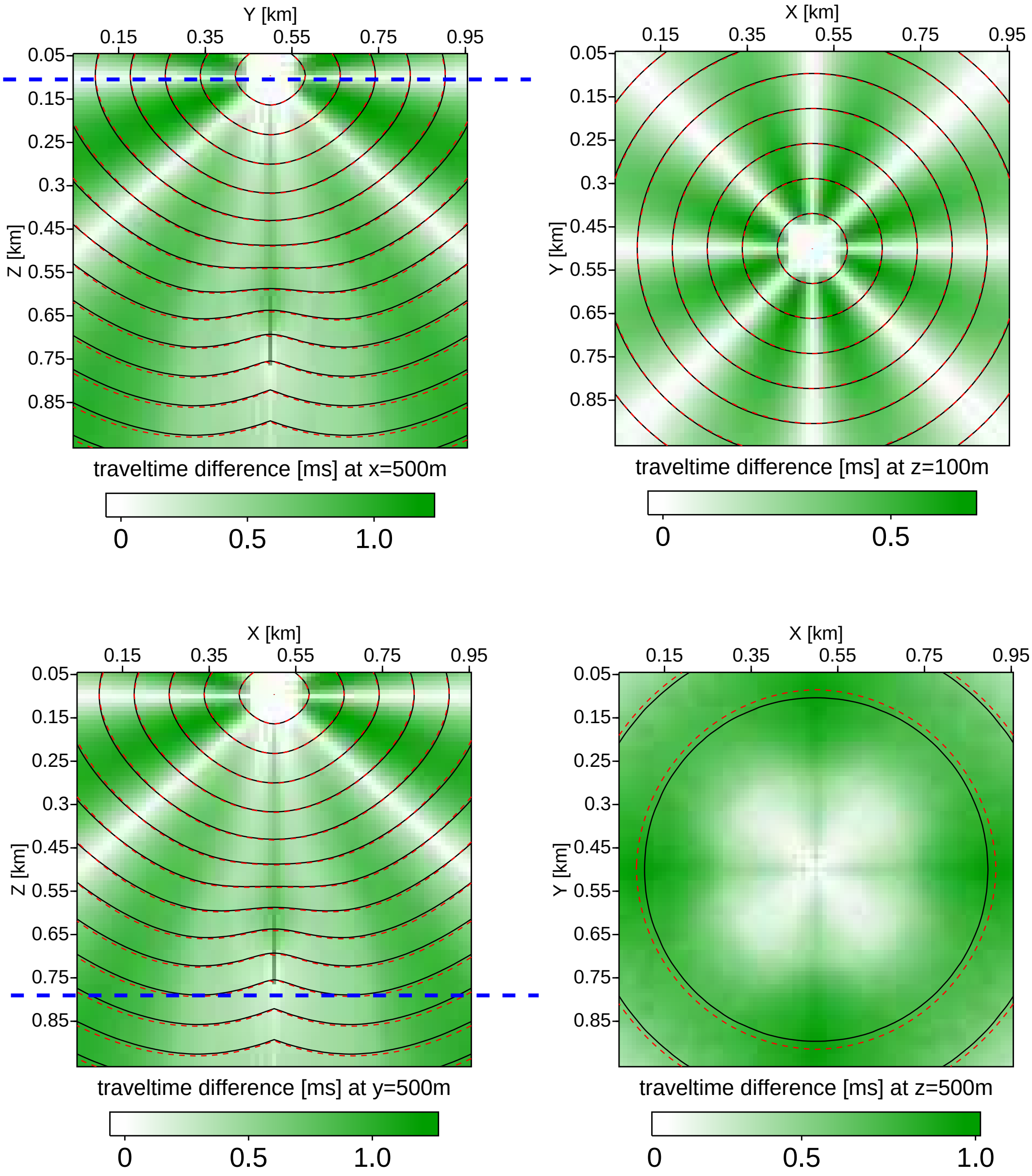

Figure 5.14: Wavefronts in the factorised anisotropic model with polar symmetry. The source is located in the center of the x-y-plane and at 100 m in depth. The figures on the left side show vertical slices through the source position. The figures on the right side show horizontal slices at two different depths (100 m and 500 m). The solid lines are the wavefronts calculated by wavefront-oriented ray tracing, and the thin dashed lines are wavefronts obtained by the FD perturbation method. The underlying green scale illustrates the absolute traveltime difference between both methods in ms.

5.3 Anisotropic medium with triclinic symmetry

The most general form of anisotropy is the triclinic medium. Therefore, the next numerical example is a 3-D anisotropic model of triclinic sandstone. The elastic parameters have been obtained by Mensch and Rasolofosaon (1997) for a rock sample:

$$A_{qp} = \begin{pmatrix} 6.77 & 0.62 & 1.00 & -0.48 & 0.00 & -0.24 \\ & 4.95 & 0.43 & 0.38 & 0.67 & 0.52 \\ & & 5.09 & -0.28 & 0.09 & -0.09 \\ & & & 2.35 & 0.09 & 0.00 \\ & & & & 2.45 & 0.00 \\ & & & & & 2.88 \end{pmatrix} km^2/s^2$$

Again, traveltimes were computed first for a homogeneous triclinic model and then a heterogeneous model is assumed. The model dimension is the same as for the previous model with polar symmetry. The source location is assumed to be in the center of the x-y-plane and in 100m depth $(0.5, 0.5, 0.1\text{km})$. For the homogeneous triclinic sandstone nearly exact traveltimes can be calculated by standard ray tracing. Figure 5.15 shows the results of the comparison between the traveltimes calculated by wavefront-oriented ray tracing with the exact traveltimes. The figure includes two vertical slices through the source location and two horizontal slices in different depth (100m and 500m). The error distribution necessitates the usage of different error scales. The black lines illustrate the computed isochrones in this medium (display traveltime step is 0.04s). The relative error distribution is similar to the medium with elliptical and polar symmetry: we have small errors at the source and for the remainder of the model very accurate computed traveltimes. Again the horizontal slice in 500m depth illustrates that only more or less random inaccuracies due to round off errors of digital numbers are introduced by the wavefront-oriented ray tracing technique. As already discussed the form of the pattern visible in the traveltime error distribution is due to the traveltime interpolation to grid points.

The computed traveltimes for the quasi-shear waves are displayed in Figure 5.16 and 5.17. Both figures comprise two vertical slices through the source position and two horizontal slices 100m and 500m in depth. For the faster qS1-wave the presented isochrones in the x-z-plane are smooth and the implementation succeeds by calculating all grid point traveltimes. In comparison the results in the y-z-plane and in the x-y-plane in 100m depth possess kinks in the wavefronts. As it has been proved in the transversely isotropic case these kinks can occur if the separation of the two qS-waves fails. However, while in this example in the x-y-plane at 100m depth the kinks are visible for the qS1-wave, the isochrones of the qS2-wave are smooth and comprise no kinks at all. On closer examination the “propagation direction of the kinks” in the y-z-plane for the qS1-wave differs from the location of the kinks in the same plane for the qS2-wave. These observation suggests that the observed kinks in the isochrones are due to the wave propagation within this medium and not a consequence of difficulties to separated both qS-waves.

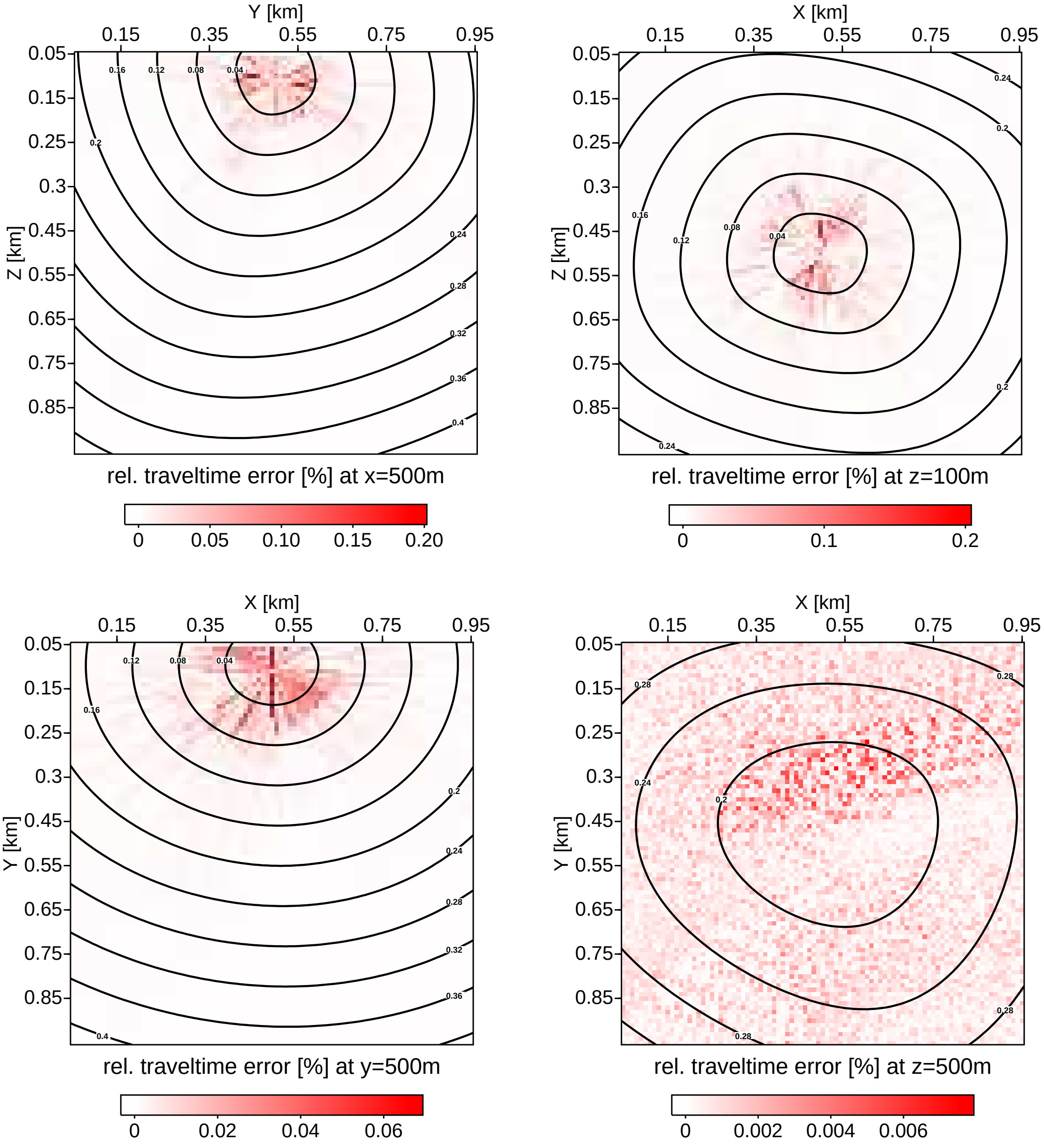

Figure 5.15: Wavefronts for the qP-wave in the homogeneous triclinic sandstone. The source is located in the center of the x-y-plane and at 100 m in depth. The figures on the left side show vertical slices through the source position. The figures on the right side show horizontal slices at two different depths (100 m and 500 m). The underlying red-scaled image shows the relative errors. Please note the different error scales.

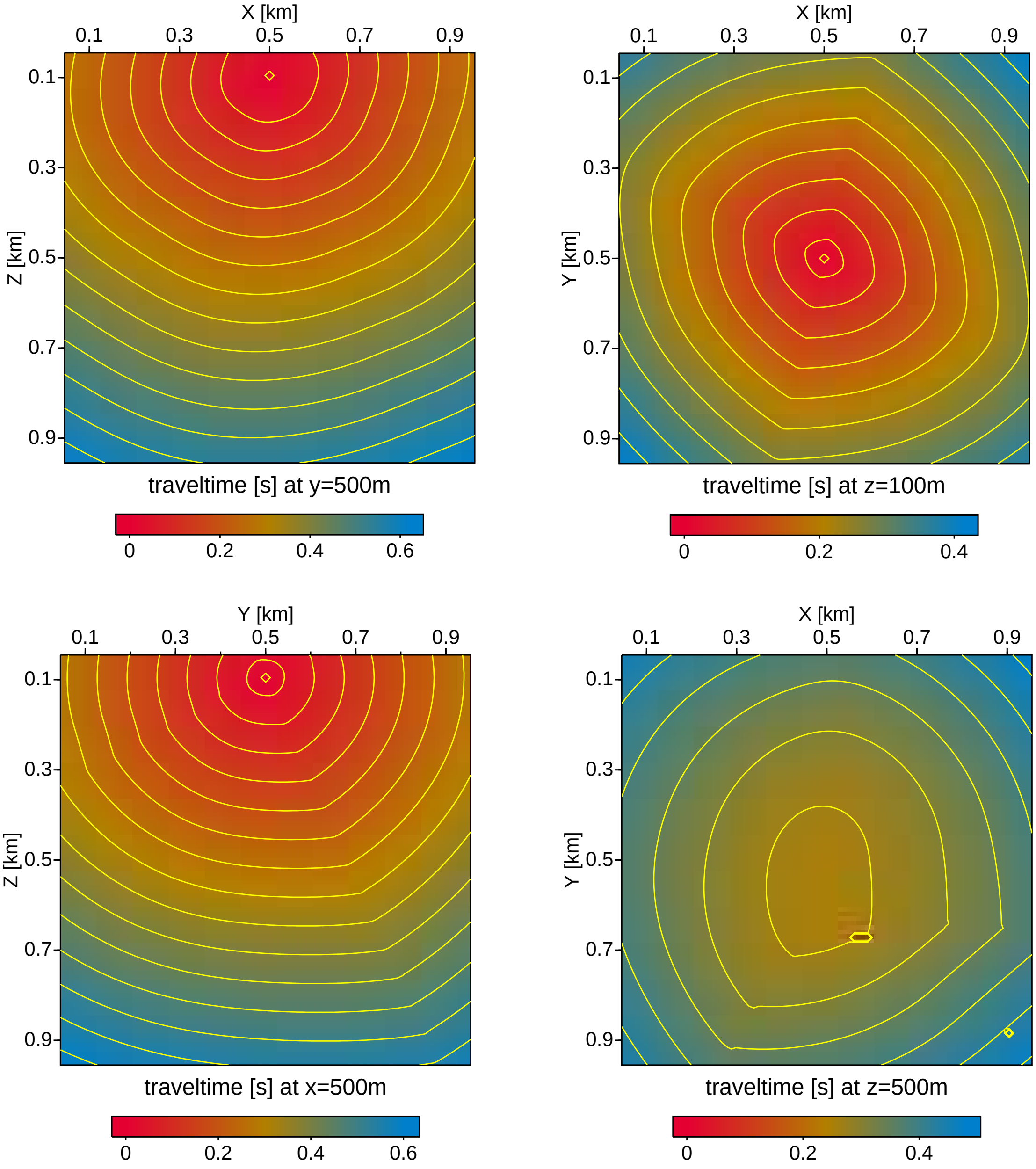

Figure 5.16: Wavefronts for the qS1-wave in the homogeneous triclinic sandstone. The source is located in the center of the x-y-plane and 100 m in depth. The figures on the left side show vertical slices through the source position. The figures on the right side show horizontal slices at two different depths (100 m and 500 m).

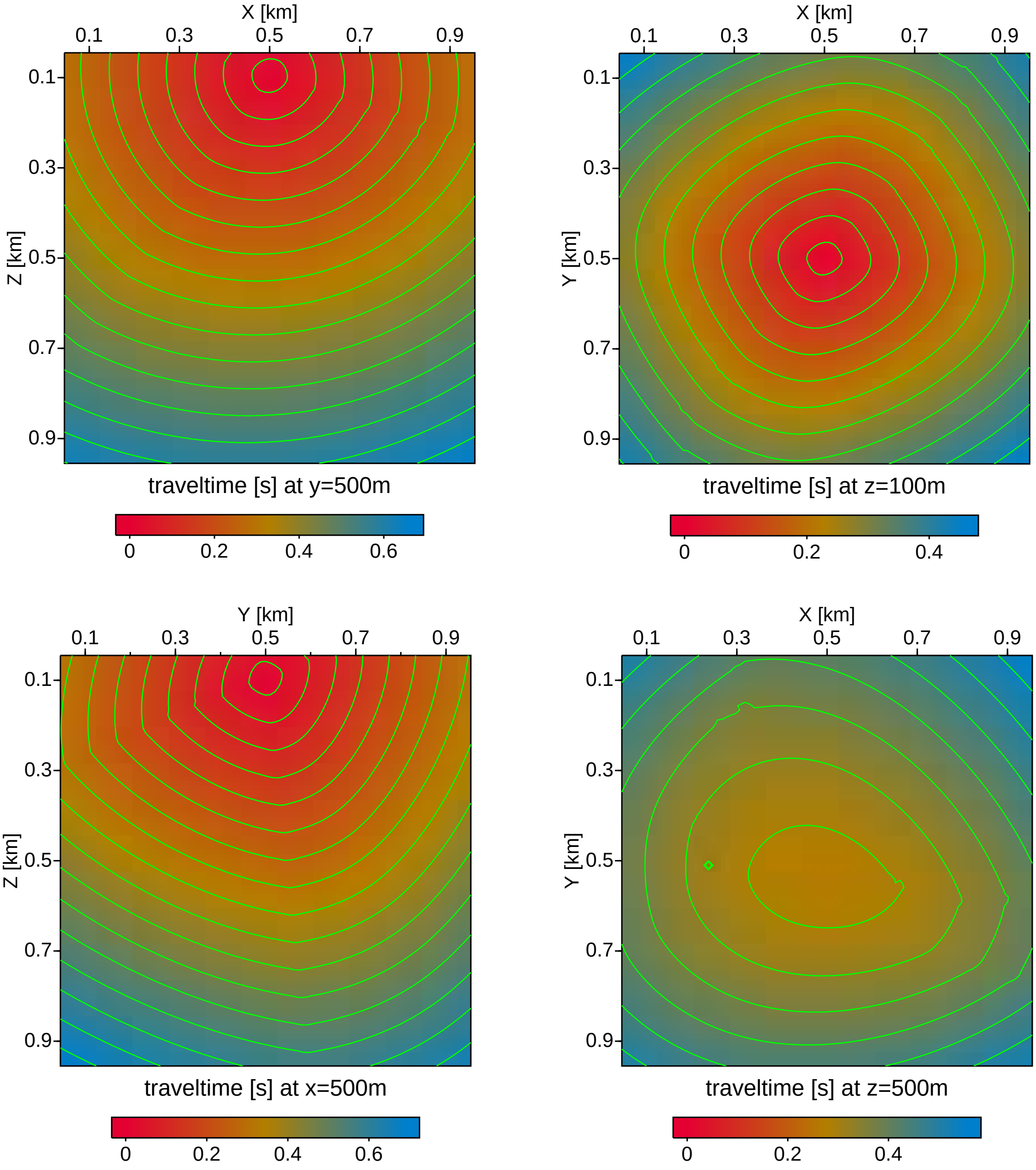

Figure 5.17: Wavefronts for the qS2-wave in the homogeneous triclinic sandstone. The source is located in the center of the x-y-plane and 100 m in depth. The figures on the left side show vertical slices through the source position. The figures on the right side show horizontal slices at two different depths (100 m and 500 m).

Sometimes undulations appear in the isochrones, which is, for example visible for the slower qS2-wave in the x-y-plane in 500m depth (see Figure 5.16). These are inaccuracies which occur predominated in the boundary region or in areas where the ray density is low despite of numerous insertion of a new ray.
For both qS-waves the traveltime grid in the x-y-plane in 500m comprises a few gaps. Here the grid point has it's initial value and during the propagation the traveltime calculation to this grid point fails.

Causes for gaps in the traveltime tables

There are two main reasons for these gaps. The interpolation is performed for each grid point within a grid cell, but sometimes the detection of the grid point fails and therefore the interpolation is not accomplished. In Figure 5.18 the 2D case is illustrated. Here a ray cell is bordered by two ray segments and two linearised wavefronts. In the 2-D case this approach leads to a complete coverage of the model, and all grid points can be detected. By assuming a 3-D model and a varying curvature of the wavefronts the geometrical construct of a ray cell is much more complicated. Consequently, the probability to "oversight" some grid points increases.

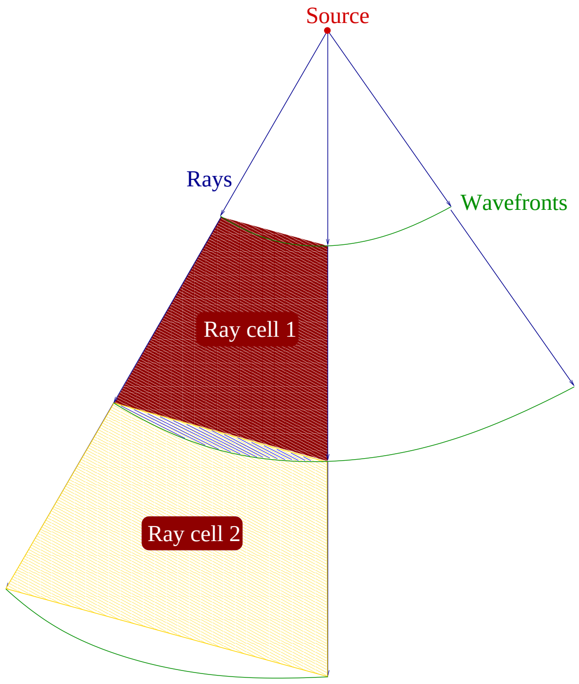

Figure 5.18: The traveltime interpolation is performed within ray cells. In the 2D case each ray cell is restricted by two ray segments and two linearised wavefronts. Grid points which are not part of ray cell 1 because of the curvature of the wavefront will be part of ray cell 2.

The singular behaviour of amplitudes in certain regions, such as caustics, and shear wave singularities in strongly anisotropic media, can produce numerical instabilities. Triplications complicate the geometry of the wavefront but do not pose complications for the ray tracing equation. In this case the problem occurs due to the traveltime interpolation and the sorting of the different arrivals. In Figure 5.19 the red circle roughly indicates the area where the traveltime difference between the first and the second arrival is too small to determine the number of arrival. For this reason there occurs a few gaps in the vicinity of a caustic or the interpolated traveltime at some grid points is less accurate.

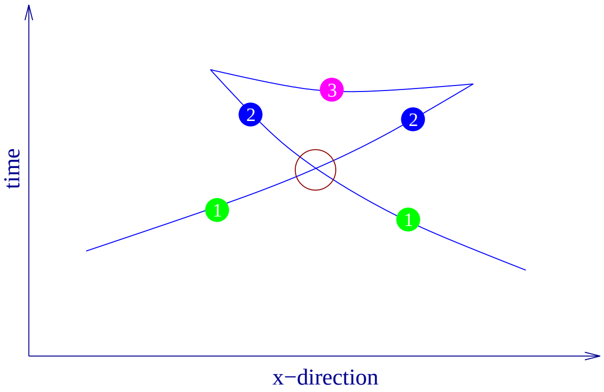

Figure 5.19: Problems by interpolation traveltimes in the vicinity of caustic.

The application of the standard ray method (Červený, 1972) to the propagation of the qS waves in inhomogeneous anisotropic media is more complicated than for the qP-wave, because of difficulties related to singularities. Singularities can cause breakdowns of the ray tracing algorithm (Gajewski and Pšenčik, 1990). Moreover, in the vicinity of shear wave singularities, the two qS waves do not propagated independently but mutually coupled (Chapman and Shearer, 1989).

Factorised anisotropic model with triclinic symmetry

To construct the heterogeneous triclinic model we again use a factorisation. For the uppermost 100m the model is homogeneous with the factor $F^2 = 3$, below the factor increases by a vertical gradient with depth up to a value of 3.4 at the bottom of the model. The size of the model and the location of the source are the same as in the previous example. Figure 5.20 shows the differences between traveltimes from the FD perturbation method and the traveltimes obtained by wavefront-oriented ray tracing. The solid lines display the wavefronts calculated by wavefront-oriented ray tracing, and the dotted lines show the results from the FD perturbation method. The maximum absolute traveltime difference is 2.3 ms and we observe an average absolute traveltime difference of 0.6 ms. It can be seen that the behaviour and the order of traveltime differences are similar to the observed errors for the heterogeneous medium with polar symmetry.
The wavefront-oriented ray tracing procedure allows the calculation of qP traveltimes within anisotropic models with arbitrary symmetry with a high accuracy. Additionally, the calculation of traveltimes for the qS-waves is performed (see Figure 5.21 and 5.22). Here, no reference qS traveltimes are available, but it is demonstrated that in general the

traveltime computation can be accomplished. The few gaps in the traveltime table can be filled by an interpolation algorithm.

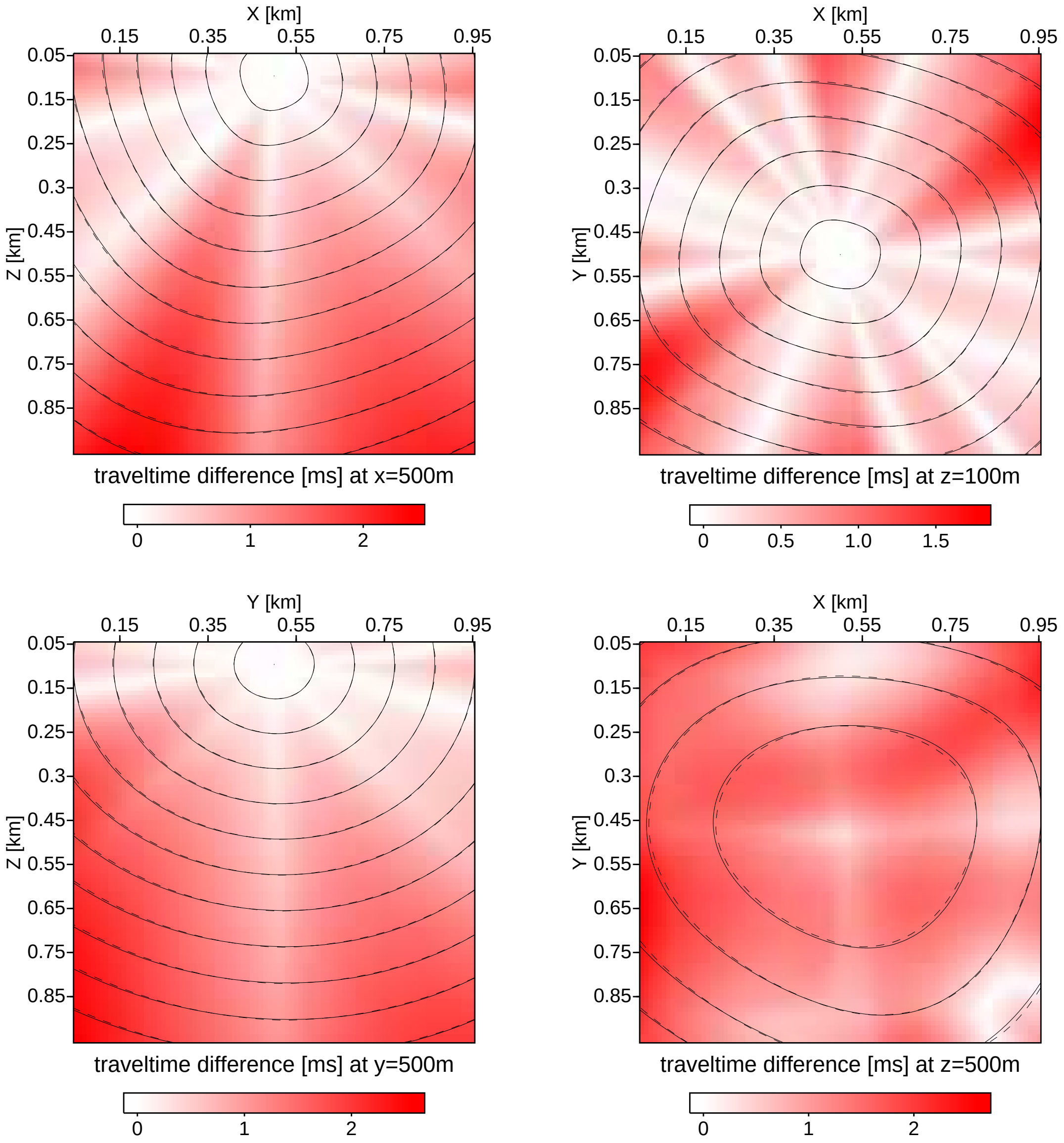

traveltime difference [ms] at x=500m

traveltime difference [ms] at z=100m

traveltime difference [ms] at y=500m

traveltime difference [ms] at z=500m

Figure 5.20: Wavefronts for the qP-wave in the factorised triclinic sandstone. The source is located in the center of the x-y-plane and at 100 m in depth. The figures on the left side show vertical slices through the source position. The figures on the right side show horizontal slices at two different depths (100 m and 500 m). The solid lines are the wavefronts calculated by wavefront-oriented ray tracing, and the thin dashed lines the wavefronts obtained by the FD perturbation method. The underlying red-scaled image shows the absolute traveltime differences. Please note the different error scales.

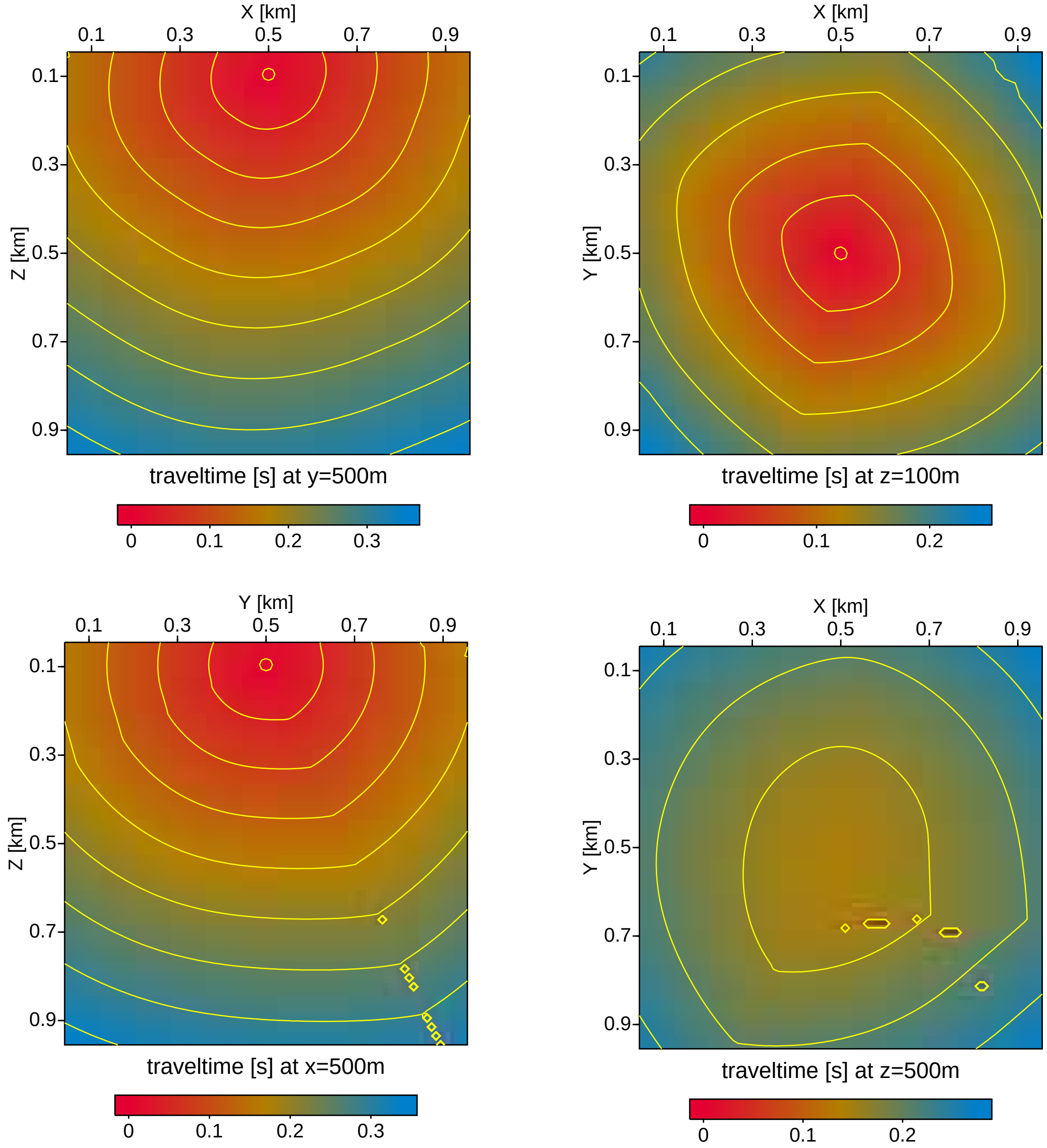

Figure 5.21: Wavefronts for the qS1-wave in the factorised triclinic sandstone. The source is located in the center of the x-y-plane and 100 m in depth. The figures on the left side show vertical slices through the source position. The figures on the right side show horizontal slices at two different depths (100 m and 500 m).

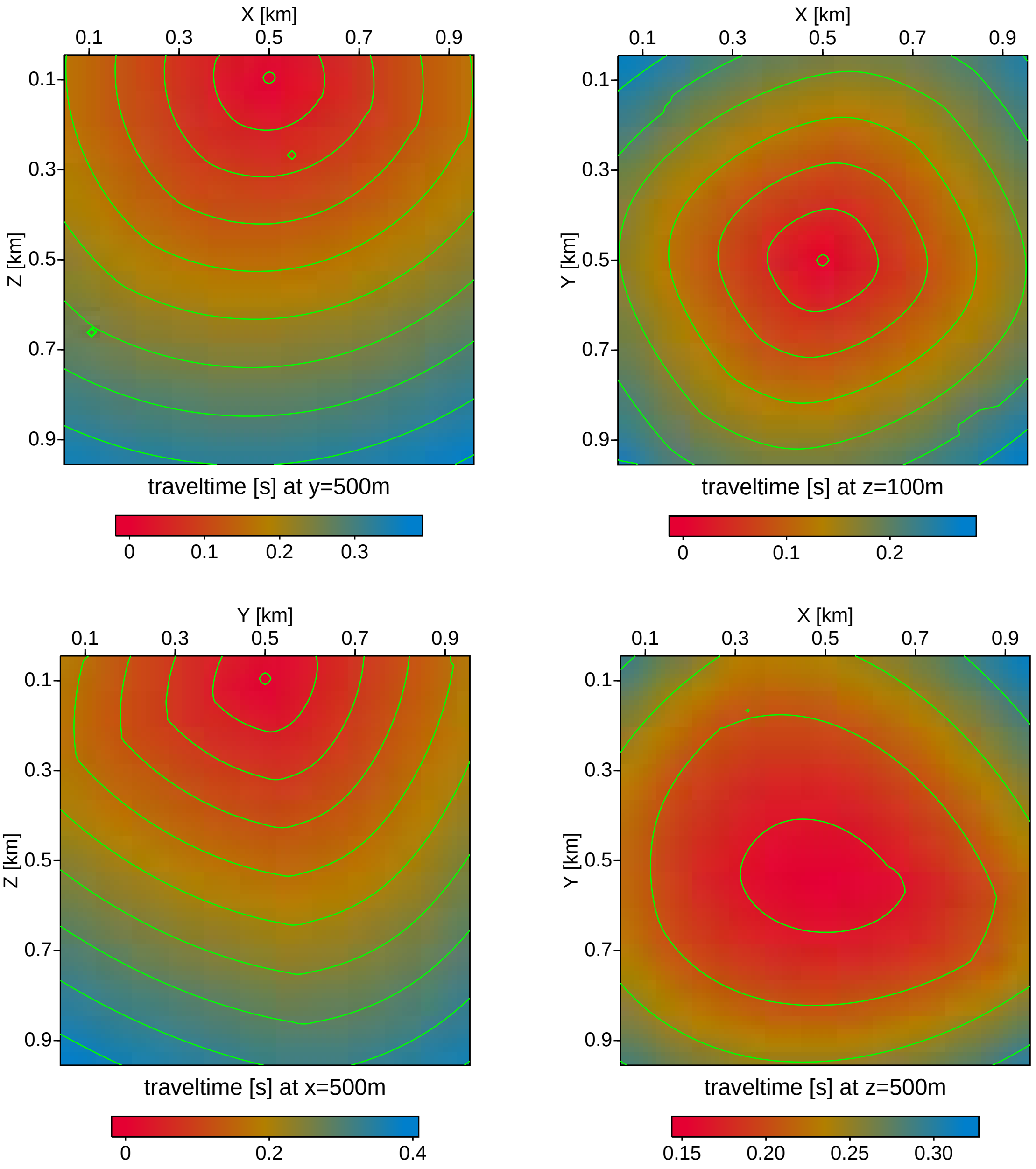

Figure 5.22: Wavefronts for the qS2-wave in the factorised triclinic sandstone. The source is located in the center of the x-y-plane and 100 m in depth. The figures on the left side show vertical slices through the source position. The figures on the right side show horizontal slices at two different depths (100 m and 500 m).

5.4 Calculation of multivalued-arrival traveltimes

The previous sections have demonstrated that the wavefront-oriented ray tracing is an efficient and accurate technique for the calculation of first arrival traveltimes. In addition this method allows the calculation of multivalued traveltimes, which occur if the wavefront triplicates. In this section we presented the traveltime results for a factorised anisotropic medium with polar symmetry. The corresponding elastic parameters are given in section 5.2. The factor-field (see Figure 5.23) corresponds to a spherical intrusion, where the factor decreases from $f^2(x_i) = 5$ to $f^2(x_i) = 2$.

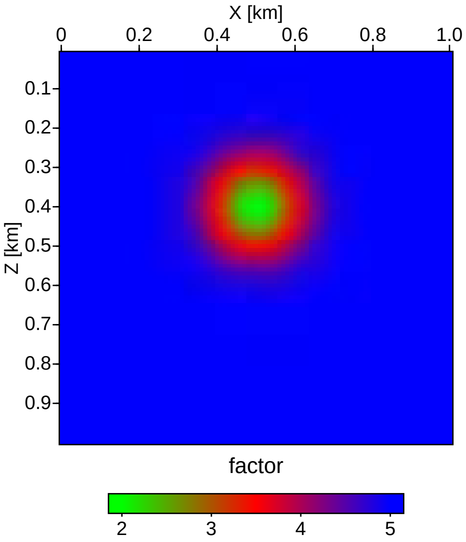

Figure 5.23: Factor field for the heterogeneous anisotropic medium. The constant factor field ($f^2 = 5$) has a spherical intrusion, where the factor decreases to $f^2 = 2$ in the center of the lens structure.

The behaviour of the factor-field causes the wavefront to gradually fold into itself forming a cusp. The traveltimes which are shown in Figure 5.24 are calculated for the qSV-wave. The figure shows 2-D slices in the x-z-plane at the left side and y-z-plane at the right side. All arrivals are displayed.

As already mentioned before in the immediate vicinity of a caustic sometimes the precise calculation of multivalued traveltimes on grid points failed. This region is roughly bounded by the green rectangle. Since here the traveltimes of the first arrivals and the second arrival traveltimes are close to each other and therefore, it is difficult to distinguish between them. This effect is reflected in the unevenness of the isochrones of the second arrivals (see Figure 5.24 (b)) near the caustic.

In comparison, the distinction between third and second arrival is unambiguously. Figure 5.24 demonstrates that the isochrones of the second and third arrivals for the rest of the model, apart from the caustic region, are smooth and traceable.

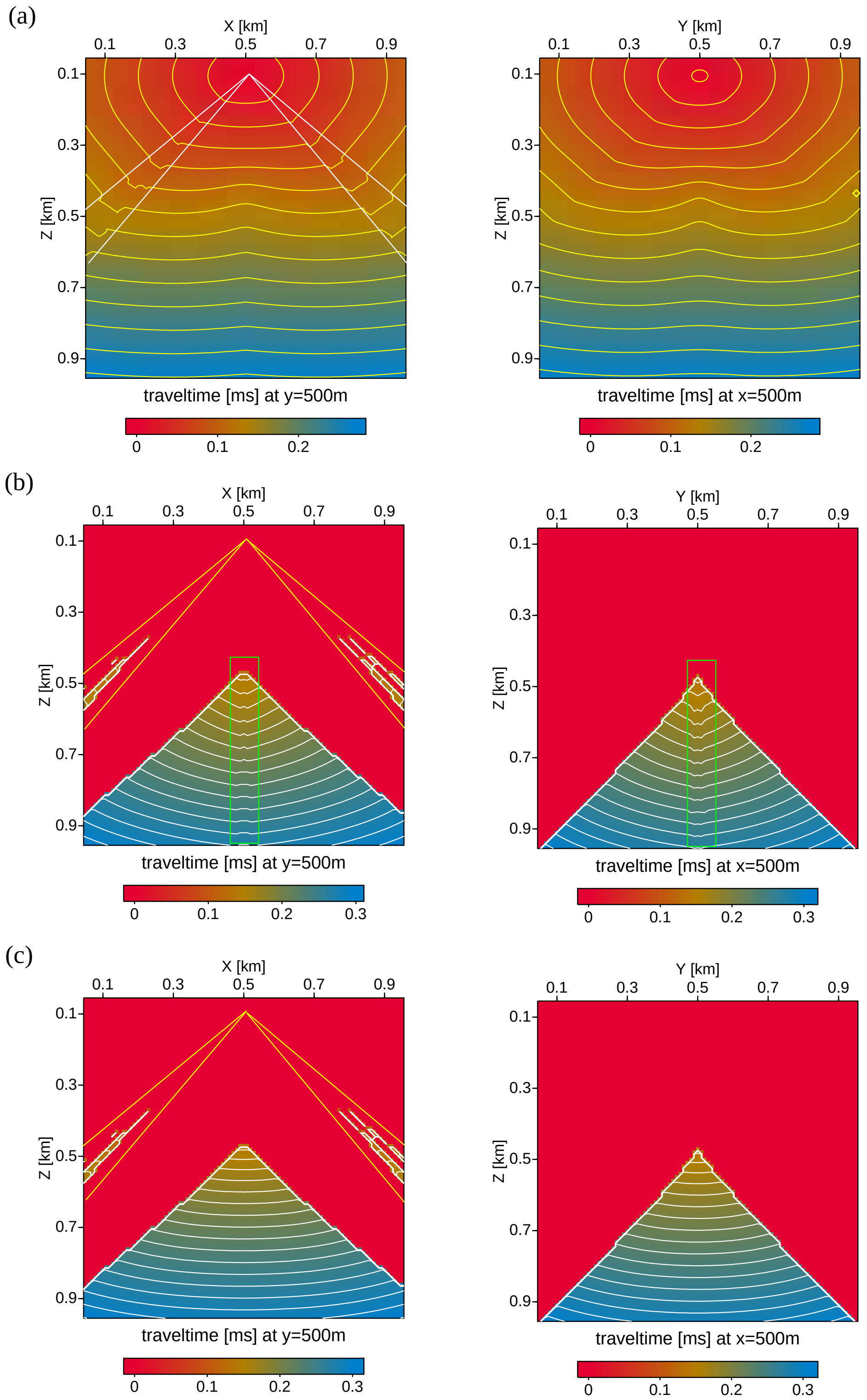

Figure 5.24: First (a), second (b) and third (c) arrivals in the factorised anisotropic model with polar symmetry.

The observed undulations indicated by the white lines in Figure 5.24(a) are due to the shear wave singularities. This effect was already discussed for the homogeneous model with transversely anisotropic symmetry. Consequently for the qSH-wave similar problems by calculating the traveltimes occurs within the marked region, which are not shown here. Obviously the artifacts in the second and third arrival traveltimes are connected to this shear wave singularity.

Chapter 6

Traveltime-based migration with angular parametrisation

So far this work has presented a method to calculate traveltimes in heterogeneous 3-D anisotropic media. Traveltimes are needed in several seismic processing methods such as Kirchhoff prestack and poststack migration, migration velocity analysis, Kirchhoff modelling, or traveltime tomography. The largest number of traveltime is needed by 3-D prestack Kirchhoff depth migration. The resulting traveltime tables calculated by the wavefront-oriented ray-tracing method can be directly used for the conventional migration techniques. Gray et al. (2001) give an overview of current migration practice.
Common-offset migration results in common-image gathers that can be used for migration velocity analysis (MVA) and amplitude-versus offset (AVO) studies. For amplitude-versus-angle (AVA) studies an offset-to-angle transformation involving two complete prestack common-offset migrations need to be performed (Bleistein, 1987). Prestack depth Kirchhoff migration is implemented as diffraction stacking along traveltime curves in the prestack data using source-receiver coordinates as integration variables. This configuration, however, can complicate the determination of the reflection angle of a reflection event for a given source-receiver pair.
In geological complex situations, such as imaging beneath gas clouds or salt bodies, multipathing occurs. There it may happen that for a single subsurface point two (or more) specular events with different reflection angles are recorded into the same common-shot or common-offset gather. Here, the single-path assumption of most common-offset migrations is violated, and the resulting common-image gathers are unsuitable for AVO or velocity analysis (Xu et al., 2001). Problems caused by multipathing can be resolved by inversion or migration using angle coordinates at the depth image point (Brandsberg-Dahl et al., 2001). In this context, deHoop et al. (1999) replaced the surface coordinates by the migration dip, the scattering angle, and the azimuth.

In this chapter I introduce a strategy for a migration with angular parametrisation in combination with ray shooting and hyperbolic traveltime interpolation to calculate the traveltimes. In the first step, I will explain the general idea of this technique. Till now, the method is developed for 3-D models where no variation in the third direction is assumed. Therefore, the basic concept is described by 2-D slices.

The implementation of the traveltime-based migration in the angular domain will be described by using a complex isotropic velocity model. The medium (see Figure 6.1) is composed of two layers with a lens-shaped high velocity intrusion in the upper layer. The velocity varies from 3000 m/s to 4500 m/s. The model dimensions are 2 kilometers in depth and 3 kilometers in x-direction. Inside the predefined target zone (see Figure 6.1) traveltimes are calculated from image points on a coarse grid to the registration surface. To provide the desired uniform angular coverage at the image point M the slownesses rays emerging at M are chosen by equidistant angles. To calculate the traveltimes by rayshooting from the image point M to a point at the surface we solve the kinematic ray tracing system (2.28) with the corresponding slownesses as initial conditions (see Figure 6.2a).

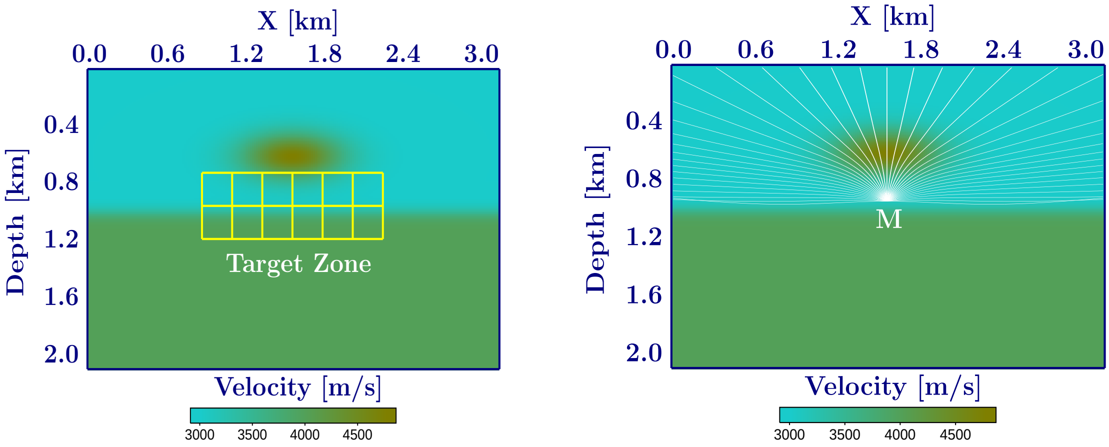

Figure 6.1: Left: Definition of the target zone. Right: Rayshooting for an image point on a coarsely gridded subsurface to the surface for each angle increment.

For the kinematic ray tracing system the constant traveltime step Δt is defined. After each time step the position of the ray endpoint and the slowness at this new ray endpoint is calculated (see Figure 6.2b and 6.2c). If the ray passes the surface the traveltime step will be bisected as long as the distance between the ray endpoint and the surface is less than 10 cm (see Figure 6.2d).

As it can be observed in Figure 6.3, the equi-angular increment at the image point does not coincide with an uniform coverage at the registration surface.

Consequently, the traces which are recorded at the marked green triangles, which represent sources and receiver positions, have negligible contribution to that image point. During the migration only those traces, which have a significant contribution to the image point, are taken into account. By applying rayshooting the traveltimes at irregularly discretise positions on the registration surface are computed. This is illustrated in Figure 6.4 by the red curve. In a typical seismic experiment the receiver spacing is uniform. Therefore, in most cases there will be no source or receiver at the ray-end position.

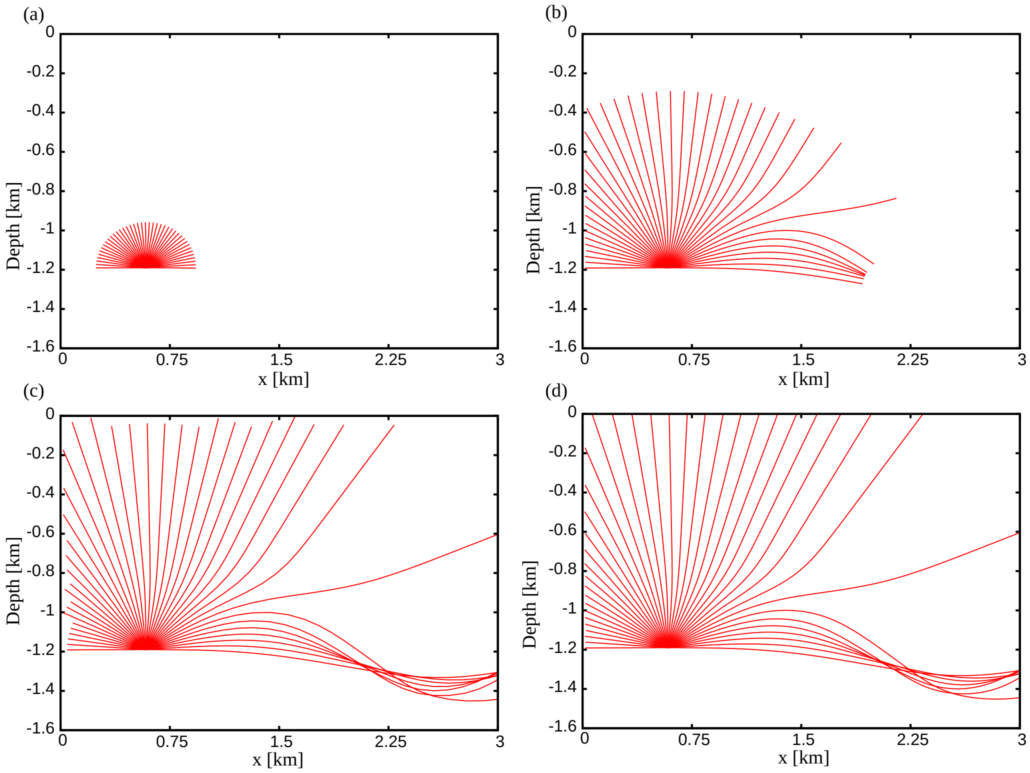

Figure 6.2: For the rayshooting procedure a constant traveltime step Δt is defined. If the ray pass over the surface the traveltime step will be bisected. This procedure will be repeated as long as the difference between the ray endpoint and the surface is less than $10\,cm$.

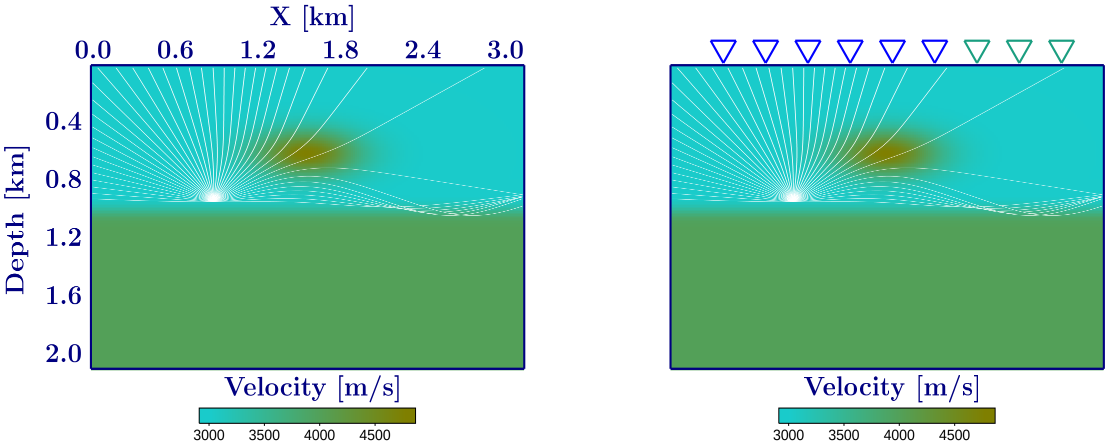

Figure 6.3: If the model includes a geologically complex subsurface structure, the equiangular increment at the image point does not lead to an equidistant spacing at the registration surface.

If the distance between the receiver and the ray end point is greater than a predefine

distance the shooting angle will be reduced as long as the angle step is greater than a predefined angle step.
Instead of applying seismic trace interpolation (e.g. Spitz, 1991), I calculate the traveltime to the real trace positions by applying hyperbolic traveltime interpolation. For this purpose I have extended the hyperbolic traveltime approach by Vanelle and Gajewski (2002a) to irregular traveltime grids.
This approach allows to interpolate the traveltimes to the real trace position (Figure 6.4). The derived formulas for the traveltime coefficients in this case were already given in section 7.2.
Until now the implementation do not consider, that the interpolation of the traveltimes to the receivers and therefore the corresponding movement at the surface is associated to a slightly different ray, and consequently to a different angle at the image point. By assuming the theory of the paraxial ray it would be possible to get the new departure angle.

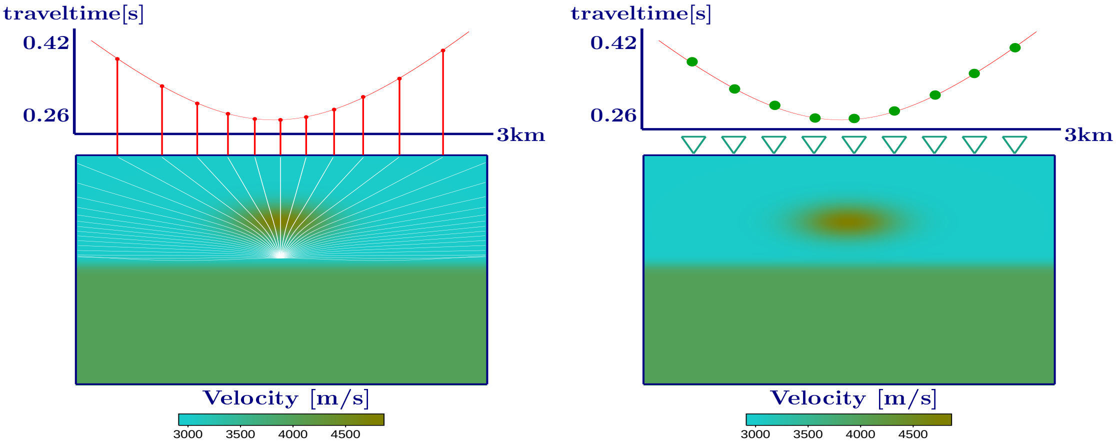

Figure 6.4: Left: The red dots, respectively the red line, illustrate the traveltime curve that is computed by rayshooting. Right: the migration requires the traveltimes at the real receiver position. Therefore, I implemented the hyperbolic traveltime interpolation for irregular grids.

To obtain an image with high resolution, the subsurface is discretise on a fine grid. Since traveltimes to the registration surface are required for each image point on that fine migration grid, I also use hyperbolic traveltime interpolation. Then, rayshooting only needs to be carried out for image points on a coarse grid. By using these traveltimes all coefficients for the hyperbolic traveltime interpolation are computed. Now we have the ability to calculate all traveltimes for all source-receiver combinations.

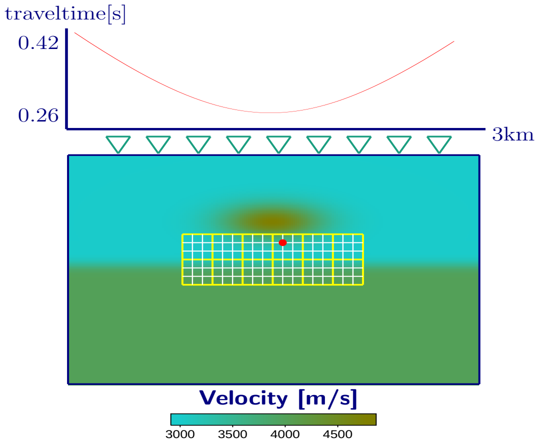

Figure 6.5: To provide a most realistical image of the subsurface the traveltimes are needed on a fine migration grid. Therefore, the hyperbolic traveltime interpolation is also used for the interpolation of traveltimes of new image points in the subsurface.

Chapter 7

Hyperbolic traveltime expansion

As already shown in the previous chapter of this work, traveltime tables can be calculated efficiently. Kirchhoff migration, for instance, needs these traveltime maps for the summation stack along the diffraction surface. In the case of 3-D depth migration large amounts of finely-gridded traveltime tables are required. The effort in computational time as well as in data storage can be significantly reduced if a fast and accurate traveltime interpolation is applied.

In this context, various authors have developed second-order approximations for reflection traveltimes mainly by using dynamic ray tracing for the determination of the wavefront curvature (Ursin, 1982; Gjøystdal et al., 1984). Bortfeld (1989) established a general second order approximation of traveltimes in seismic systems, which is based on the paraxial ray approximation (Červený, 2001). A hyperbolic variant of the paraxial traveltime interpolation was introduced by Schleicher et al. (1993). Both methods are, however, restricted to reference surfaces, e.g. source and receiver surfaces.

Gajewski (1998) provides the hyperbolic variant of the paraxial approximation and introduces an algorithm to determine the interpolation coefficients directly from traveltimes, and therewith finds an alternative to dynamic ray tracing. That technique is, however restricted to horizontal interpolation.

Accordingly, Vanelle and Gajewski (2002a) introduce a hyperbolic and parabolic traveltime interpolation algorithm, that is neither restricted to laterally homogeneous media nor to interpolation in horizontal layers. Additionally, it allows also the interpolation of sources, not only receivers.

This chapter contains the hyperbolic traveltime expansion in arbitrary 3-D media and gives a brief description of the determination of the Taylor coefficients (section 7.1) . For the application to the migration in the angular domain the hyperbolic traveltime interpolation is extended to an irregular grid (see section 7.2). Due to the fact that this method allows the interpolation of sources (see section 7.3) the effort in computational storage can be significantly reduced. To demonstrate the accuracy of the traveltime interpolation several numerical examples in 2-D are given in section 7.4.

7.1 Theoretical background

Since the traveltime interpolation to e.g. the receiver position in this work is based on the hyperbolic traveltime interpolation this section summarises the basic principles of this theory.

The Taylor expansion of a traveltime T from a source at the coordinates $\vec{s}$ to a receiver at $\vec{g}$ yields a good approximation of the exact traveltime provided that the distance $\Delta\vec{g}$ and $\Delta\vec{s}$ to the expansion point, $\vec{g}_0$, $\vec{s}_0$, are small (the first and second order spatial derivatives are assumed to exist and be continuous). For the 3-D case, the Taylor expansion has to be carried out in six variables: the three components of the source position vector $\vec{s} = (s_1, s_2, s_3)^T$ and those of the receiver position $\vec{g} = (g_1, g_2, g_3)^T$. The hyperbolic traveltime expression is given by Vanelle and Gajewski (2002a)

$$\begin{aligned} T^2(s_i, g_i) = T_0^2 \quad &+ \quad \Delta s_i \left.\frac{\partial T^2}{\partial s_i}\right|_{\vec{s_0},\vec{g_0}} + \Delta g_i \left.\frac{\partial T^2}{\partial g_i}\right|_{\vec{s_0},\vec{g_0}} + \Delta s_i \Delta g_j \left.\frac{\partial^2 T^2}{\partial s_i \partial g_j}\right|_{\vec{s_0},\vec{g_0}} \\ &+ \quad \frac{1}{2}\Delta s_i \Delta s_j \left.\frac{\partial^2 T^2}{\partial s_i \partial s_j}\right|_{\vec{s_0},\vec{g_0}} + \frac{1}{2}\Delta g_i \Delta g_j \left.\frac{\partial^2 T^2}{\partial g_i \partial g_j}\right|_{\vec{s_0},\vec{g_0}} + \mathcal{O}(3), \end{aligned} \tag{7.1}$$

where T_0 is the traveltime at the expansion point, e.g. calculated by the wavefront-oriented ray tracing on a coarse grid. The "source" location here is assumed to be at the surface, and the receiver at the image point (see Figure 7.1). The first-order derivatives

$$p_{i_0} = -\left.\frac{\partial T}{\partial s_i}\right|_{\vec{s_0}\vec{g_0}} \quad \text{and} \quad q_{i_0} = \left.\frac{\partial T}{\partial g_i}\right|_{\vec{s_0}\vec{g_0}}, \tag{7.2}$$

are the slowness vectors at the source and the receiver point, and the matrices

$$\begin{aligned} S_{ij} &= -\left.\frac{\partial^2 T}{\partial s_i \partial s_j}\right|_{\vec{s_0}\vec{g_0}} = S_{ji}, \\ G_{ij} &= \left.\frac{\partial^2 T}{\partial g_i \partial g_j}\right|_{\vec{s_0}\vec{g_0}} = G_{ji}, \\ N_{ij} &= -\left.\frac{\partial^2 T}{\partial s_i \partial g_j}\right|_{\vec{s_0}\vec{g_0}} \neq N_{ji}, \end{aligned} \tag{7.3}$$

($i, j = 1, 2, 3$ correspond to x, y, and z) are the second derivatives of the traveltimes, which are related to the curvature of the wavefront. With these coefficients the Taylor series (7.1) reads

$$\begin{aligned} T^2(\vec{s}, \vec{g}) \quad &= \quad (T_0 - \vec{p}_0^{\,T} \Delta\vec{s} + \vec{q}_0^{\,T} \Delta\vec{g})^2 \\ &+ \quad T_0 \left(-2\Delta\vec{s}^{\,T} \underline{\mathsf{N}} \Delta\vec{g} - \Delta\vec{s}^{\,T} \underline{\mathsf{S}} \Delta\vec{s} + \Delta\vec{g}^{\,T} \underline{\mathsf{G}} \Delta\vec{g}\right) + \mathcal{O}(3). \end{aligned} \tag{7.4}$$

To compute, e.g. q_{x_0} and G_{xx} from the traveltime tables, only the traveltimes τ_0, τ_m and τ_p are required, as shown in Figure 7.1. The traveltimes are inserted into the hyperbolic expansion (7.4). Building the sum and the difference of the resulting expressions yields

$$\begin{array}{rcl}
\tau_m^2 & = & \tau_0^2 + \; q_{x0}^2\Delta g_x^2 - 2\tau_0 \; q_{x0}\Delta g_x + \; \tau_0 \; G_{xx}\Delta g_x^2 \\
\tau_p^2 & = & \tau_0^2 + \; q_{x0}^2\Delta g_x^2 + 2\tau_0 \; q_{x0}\Delta g_x + \; \tau_0 \; G_{xx}\Delta g_x^2 \\
\hline
\tau_m^2 + \tau_p^2 & = & 2\tau_0^2 + 2q_{x0}^2\Delta g_x^2 \qquad\qquad + 2\tau_0 \; G_{xx}\Delta g_x^2 \\
\tau_m^2 - \tau_p^2 & = & \qquad\qquad - 4\tau_0 \; q_{x0}\Delta g_x
\end{array} \tag{7.5}$$

As result the coefficients q_{x0} and G_{xx} are calculated by:

$$q_{x0} = \frac{\tau_m^2 - \tau_p^2}{4T_0\Delta g_x}, \quad \text{and} \quad G_{xx} = \frac{\tau_m^2 + \tau_p^2 - 2\tau_0^2}{2\tau_0\Delta g_x^2} - \frac{q_{x0}^2}{\tau_0}. \tag{7.6}$$

The $y-$ and the $z-$ components of $\vec{q}_0$ and $\hat{G}$ can be found in the same way by varying g_y and g_z, respectively. Varying both g_x and g_y leads to G_{xy}; and the components G_{xz} and G_{yz} follow accordingly. The determination of $\vec{p}_0$ and $\hat{S}$ is straightforward: instead of varying the receiver position we use different source positions.

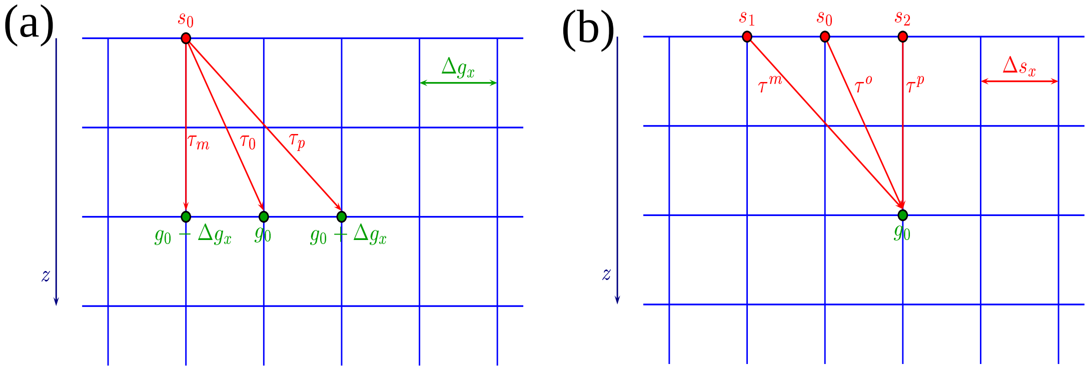

Figure 7.1: (a) Determination of the coefficients q_{x_0} and G_{xx}: the traveltimes τ_o from $\vec{s}_0$ to $\vec{g}_0$, τ_m from $\vec{s}_0$ to $\vec{g}_0 - \Delta g_x$, and τ_p from $\vec{s}_0$ to $\vec{g}_0 + \Delta g_x$ are required. Correspondingly (b), the determination of the coefficients p_{x_0} and S_{xx}: the τ^o from $\vec{s}_0$ to $\vec{g}_0$, τ^m from $\vec{s}_0$ to $\vec{g}_0 - \Delta g_x$, and τ^p from $\vec{s}_0$ to $\vec{g}_0 + \Delta g_x$ are required (Vanelle, 2002a).

The determination of all remaining coefficients which are needed in equation 7.1 are given in Vanelle (2002a).

7.2 Hyperbolic traveltime equation for irregular grids

To interpolate the traveltimes from the intersection points of the rays with the registration surface to the receiver position we use the 3-D hyperbolic traveltime expansion introduced by Vanelle (2002a).
In contrast to the previous section, the "source" position now is assumed to be the image point, and the receiver in the registration surface. Therefore, the expansion point now

corresponds to the “source” on the coarse subsurface grid and the receiver at the endpoint of the ray in the registration surface. We will now consider one expansion point. The receiver position of the expansion point is defined by the emergence angle at the image point. The coefficients G_{xx} and q_{x0} can be computed from the three traveltime values $T_0 = T(\vec{s}_0, \vec{g}_0)$, $T_m = T(\vec{s}_0, \vec{g}_0 - \Delta g_m)$ and $T_p = T(\vec{s}_0, \vec{g}_0 + \Delta g_p)$ (see Figure 7.2).

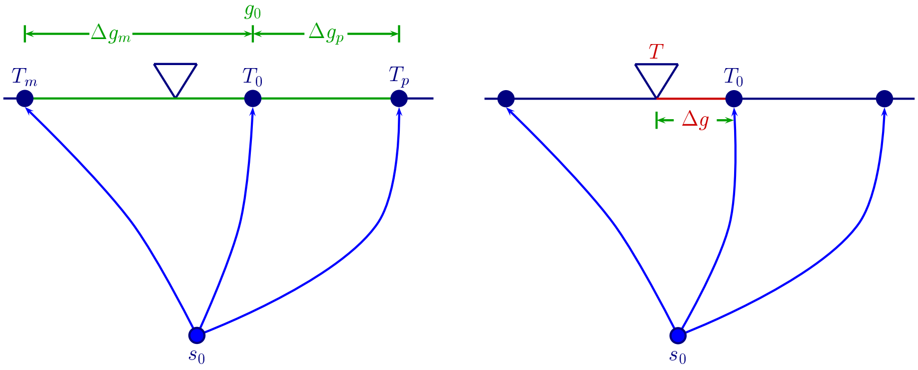

Figure 7.2: Traveltime interpolation to the real receiver position. The traveltimes T_m, T_0 and T_p are computed by ray shooting. First step (left): Determination of the traveltime coefficients q_x and G_{xx} at position g_0. Second step (right): Interpolation to the real receiver position g.

In comparison to the regular grid formula given by Vanelle and Gajewski (2002a), here the distances between grid points may differ ($\Delta g_m \neq \Delta g_p$). The insertion of T_m and T_p into the hyperbolic equation (7.1) leads to a linear system of two equations with two unknowns, which can be solved for q_{x0} and G_{xx}.

$$\begin{array}{rcl}
T_m^2 & = & T_0^2 + q_{x0}^2\ \Delta g_m^2 - 2T_0\ q_{x0}\ \Delta g_m + T_0\ G_{xx}\ \Delta g_m^2 \\
T_p^2 & = & T_0^2 + q_{x0}^2\ \Delta g_p^2 + 2T_0\ q_{x0}\ \Delta g_p + T_0\ G_{xx}\ \Delta g_p^2 \\
\hline
T_m^2 + T_p^2 & = & 2T_0^2 + q_{x0}^2(\Delta g_m^2 + \Delta g_p^2) - 2T_0\ q_{x0}(\Delta g_m - \Delta g_p) + T_0\ G_{xx}(\Delta g_m^2 + \Delta g_p^2) \\
T_m^2 - T_p^2 & = & + q_{x0}^2(\Delta g_m^2 - \Delta g_p^2) - 2T_0\ q_{x0}(\Delta g_m + \Delta g_p) + T_0\ G_{xx}(\Delta g_m^2 - \Delta g_p^2)
\end{array} \tag{7.7}$$

As result for the slowness component q_{x0} and for the second-derivative component G_{xx} we get

$$\begin{aligned}
q_{x0} &= \frac{T_p^2 \Delta g_m^2 - T_m^2 \Delta g_p^2 - T_0^2(\Delta g_m^2 - \Delta g_p^2)}{2T_0(\Delta g_m^2 \Delta g_p + \Delta g_m \Delta g_p^2)}, \\
G_{xx} &= \frac{T_m^2 \Delta g_p + T_p^2 \Delta g_m - T_0^2(\Delta g_m + \Delta g_p)}{T_0(\Delta g_m^2 \Delta g_p + \Delta g_m \Delta g_p^2)} + \frac{q_{x0}^2}{T_0}.
\end{aligned} \tag{7.8}$$

After the coefficients have been determined, equation (7.1) can be directly applied for the traveltime interpolation to the real receiver position g (see Figure 7.2). This is repeated for all receiver positions and for each subsurface point.

7.3 Interpolation to the fine migration grid

It is also possible to interpolate traveltimes between image points, i.e. $\Delta\vec{s} \neq 0$. This requires that the derivatives with respect to the image point positions are also known. The coefficients S_{xx}, p_{x0} can be obtained from the traveltimes T_m and T_p (see Figure 7.3).

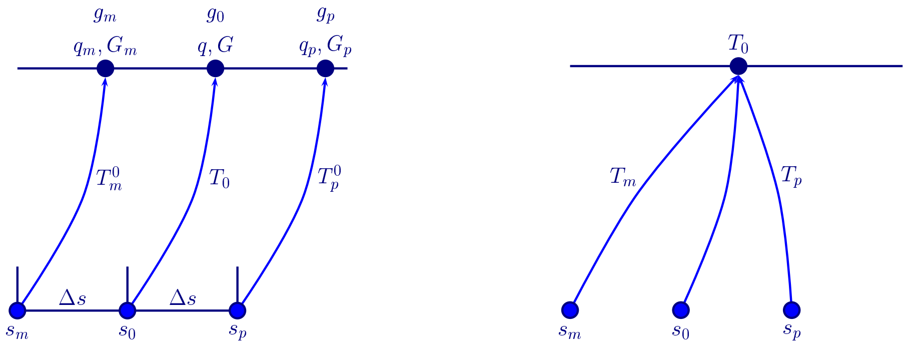

(a) (b)

Figure 7.3: (a) Rays are shot from the three subsurface points at s_m, s_0 and s_p, respectively. The corresponding traveltimes to the surface are T_m^0, T_0 and T_p^0. (b) With the coefficients q_m, q_p, G_m and G_p we obtain the traveltimes T_m and T_p. These lead to the coefficients p_{x0} and S_{xx}.

The ray shooting from the three subsurface points s_m, s_0 and s_p gives us the traveltimes T_m^0, T_0 and T_p^0. By applying the hyperbolic traveltime interpolation with the coefficients q_m and G_m for the expansion point (s_m, g_m) which we have already calculated before, we get (see also Figure 7.3)

$$T_m^2 = (T_m^0 - q_m \Delta g_m)^2 + T_m^0 G_m \Delta g_m^2. \tag{7.9}$$

Similar, interpolation with the coefficients q_p and G_p at (s_p, g_p) yields

$$T_p^2 = (T_p^0 + q_p \Delta g_p)^2 + T_p^0 G_p \Delta g_p^2. \tag{7.10}$$

With these traveltimes we can calculate the coefficients p_{x0} and S_{xx}:

$$\begin{aligned} p_{x0} &= \frac{T_m^2 - T_p^2}{4T_0 \Delta s}, \\ S_{xx} &= \frac{T_p^2 + T_m^2 - 2T_0^2}{2T_0 \Delta s^2} - \frac{p_{x0}^2}{T_0}, \end{aligned} \tag{7.11}$$

where $\Delta s = s_p - s_0 = s_0 - s_m$. The remaining coefficients are computed correspondingly. Afterwards the traveltimes can be interpolated from the fine grid of image points to the receiver positions (see also Appendix D).

7.4 Numerical examples

The hyperbolic formula from the previous sections can be used for traveltime interpolation with high accuracy, once the according sets of coefficients are known. In this section three different examples are shown: First a homogeneous anisotropic model with elliptical symmetry is presented. The accuracy investigation concerns not only the resulting traveltimes but also the coefficients themselves. The second example is an anisotropic homogeneous model with orthorhombic symmetry and the interpolated traveltimes will be compared to traveltimes calculated by the wavefront-oriented ray tracing. Finally, the interpolation of traveltimes for a more complex isotropic model is presented.

Homogeneous model with elliptical anisotropy

To illustrate the accuracy of the traveltime interpolation presented in the previous section we have chosen an anisotropic model with elliptical symmetry. As already mentioned, elliptical anisotropy is a special case of polar anisotropy with an additional constraint and it is rarely found in real rocks. This kind of symmetry, however, is suitable for verification purposes since traveltimes and synthetic seismograms can be computed analytically. We describe our model by the Thomson parameters $\epsilon = \delta = 0.187$ and $\gamma = 0.2$ and the vertical velocities $v_{p0} = 3.38$ km/s and $v_{s0} = 1.80$ km/s. The ray shooting is performed on a coarse subsurface grid of $21 \times 21 \times 21$ grid points and a grid spacing of 100 m is considered. The receivers are located at the surface with 10 m spacing.

The exact coefficients and traveltimes are calculated by the formulas that are given in appendix C. The left sides of Figures 7.4-7.6 illustrate the calculated coefficients. The solid blue lines are the analytically calculated values whereas the red dots represent the computed coefficient by the formulas derived in the previous sections, respectively in appendix D. The right side presents the corresponding relative error distribution. The highest relative errors for the x-components of the slowness at the source q_x and at the receiver p_x correspond to the region near the zero-crossing of the coefficient, because here the values themselfs are zero or very small. The average relative error is less than 0.004%. For the z-component of the first derivative p_z the relative traveltime error is still smaller, about 0.0002%. The magnitude of the relative errors for the second-order derivative in x-direction for the source S_{xx}, the receiver G_{xx} and the mixed derivatives N_{xx} is around 0.1%. Nearly the same accuracy is obtained for the second-order derivative at the source S_{xz}, S_{zz} and N_{zx}. To evaluate the accuracy of the traveltime interpolation, we will consider an image point at $s_0 = (1.1, 1.1)$km. From here and the neighbouring image points on a 100 m coarse grid we have performed ray shooting with a constant angular increment. Traveltimes were interpolated from four different image points to the receivers using (7.1) and were compared to analytic values. The results are shown in Figure 7.7 and 7.8.

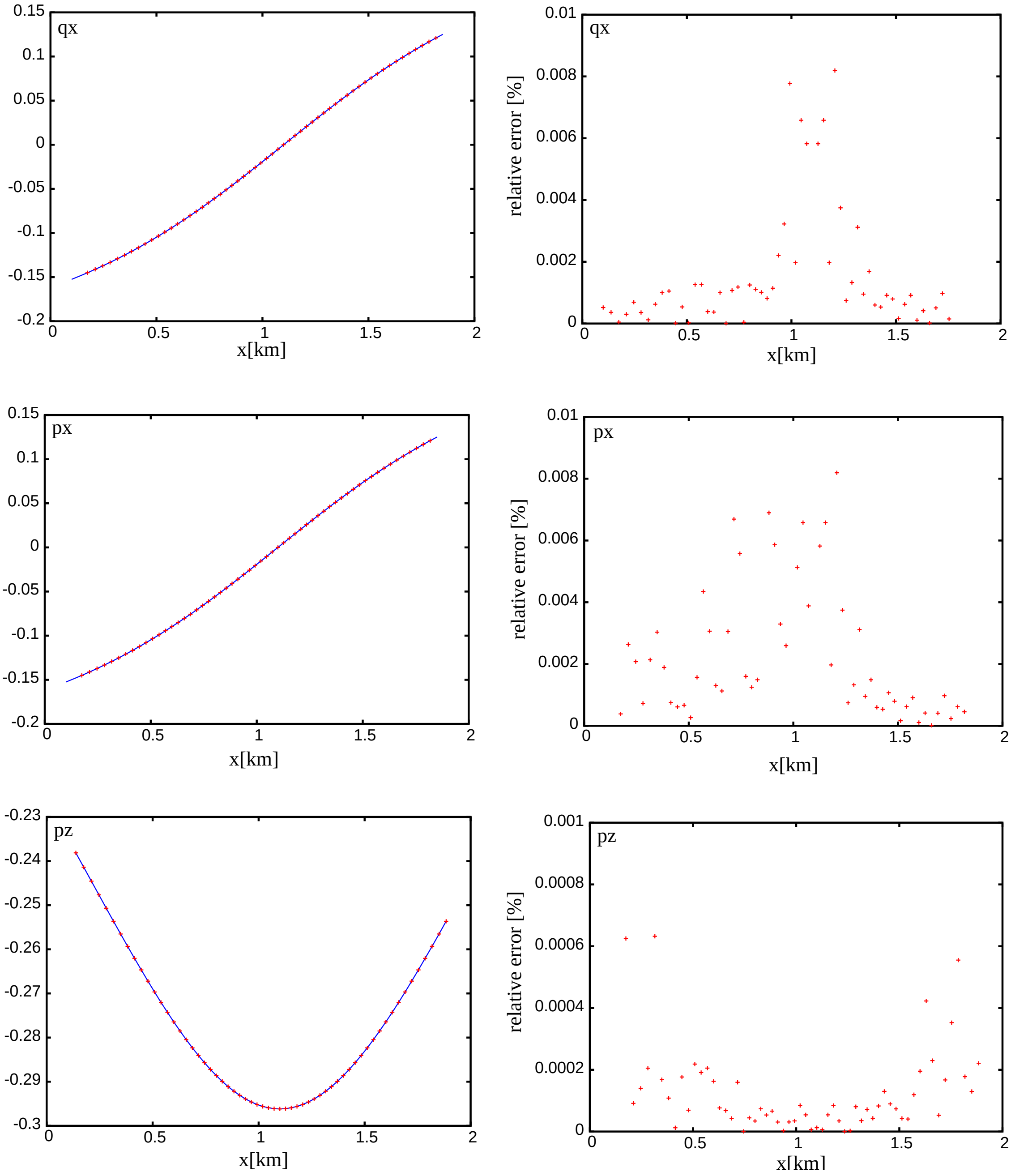

Figure 7.4: Analytical coefficients q_x, p_x, p_z for the elliptical anisotropic medium (solid blue line) and the corresponding values (red dots), calculated by the ray shooting and the hyperbolic traveltime interpolation for irregular grids. The right side shows the acquired relative errors.

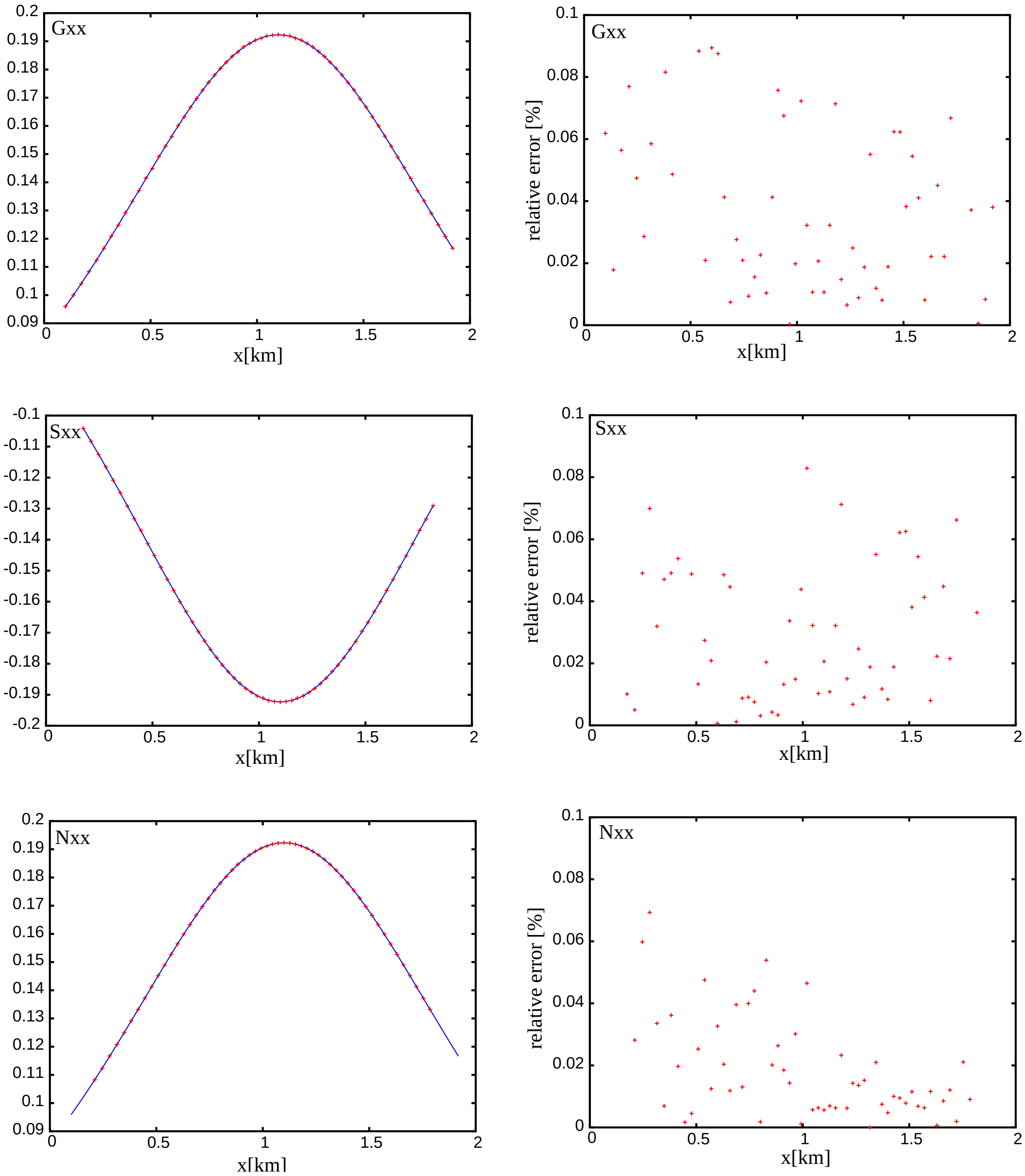

Figure 7.5: Analytical coefficients G_{xx}, S_{xx}, N_{xx} for an elliptical anisotropic medium (solid line) and the corresponding values (red dots), calculated by the ray shooting and the hyperbolic traveltime interpolation for irregular grids. The right side shows the acquired relative errors.

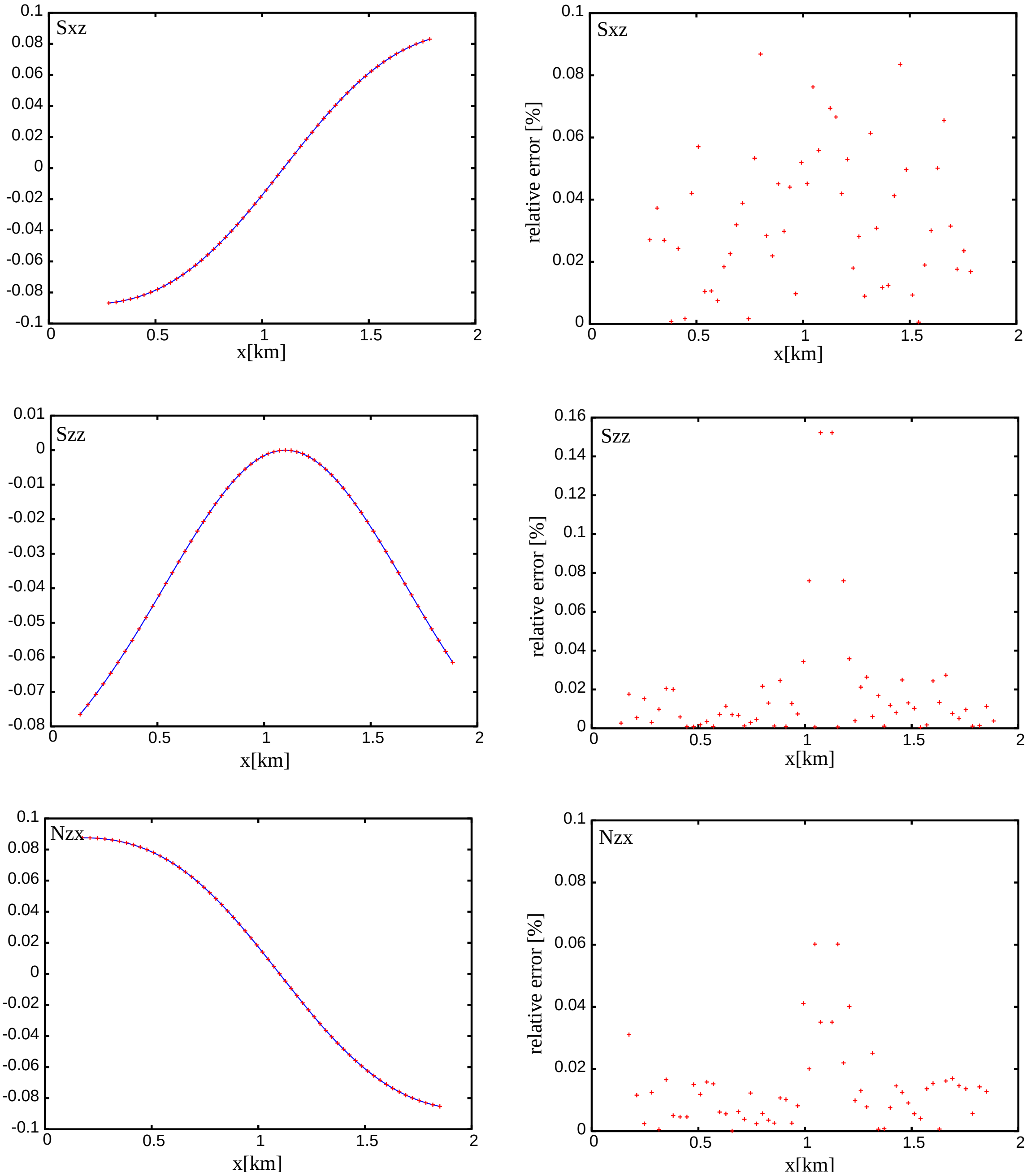

Figure 7.6: Analytical coefficients S_{xz}, S_{zz}, N_{zx} for an elliptical anisotropic medium (solid line) and the corresponding values (red dots), calculated by the ray shooting and the hyperbolic traveltime interpolation for irregular grids. The right side shows the acquired relative errors.

To differentiate the influences due to the hyperbolic traveltime interpolation first, analytically calculated input traveltimes are used for the interpolation (see Figure 7.7). In comparison 7.8 presents the traveltime errors by using the ray shooting algorithm to calculate the input traveltimes.

In both cases the figures illustrate the results for different subsurface points: The upper figure on the left side shows the absolute traveltime error for the image point on the coarse grid, i.e. at $\vec{s}_0 = (1.1, 1.1)$km. Since the source in the subsurface is shifted only in one direction, x- or z-direction $\vec{s} = (1.15, 1.1)$ $\Delta x = 50$m and $\vec{s} = (1.1, 1.15)$ $\Delta z = 50$m, the results are given in the upper left and lower right side. The results for the traveltime interpolation where the source is shifted in both directions $\vec{s} = (1.15, 1.15)$ $\Delta x = \Delta z = 50$m, is presented in the lower right figure.

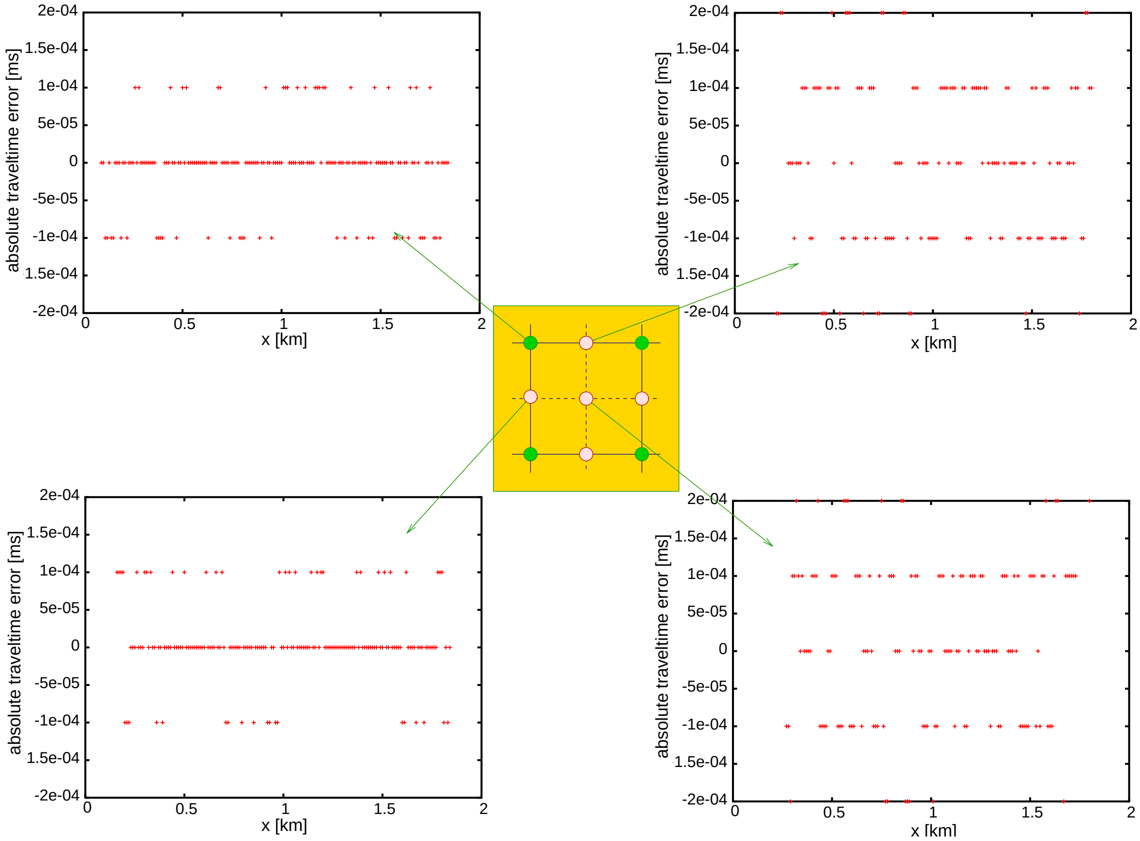

Figure 7.7: Distribution of traveltime errors with analytical input traveltimes. Upper left: errors for an image point on the coarse grid at $\vec{s}_0 = (1.1, 1.1)$km. Upper right: errors for an image point on the fine grid with $\vec{s} = (1.15, 1.1)$ $\Delta x = 50$m. Lower left: errors for an image point at $\vec{s} = (1.1, 1.15)$ $\Delta z = 50$m. Lower right: Error distribution for an image point on the fine grid with $\vec{s} = (1.15, 1.15)$ $\Delta x = \Delta z = 50$m.

For the analytical input traveltimes the hyperbolic traveltime interpolation is nearly exact, the observed absolute traveltime errors are less than $0.2 \mu s$. In comparison the observed average absolute traveltime error for the input traveltimes calculated by the ray shooting procedure is less than $0.5 \mu s$. The maximum of the traveltime errors is a magnitude larger

than for the analytically computed input traveltimes ($2.0\mu s$).
I have chosen a homogeneous medium with elliptical symmetry to validate our implementation. For this medium, the traveltime expression (7.1) is exact. Therefore, we expect traveltime errors within machine precision, which was confirmed by the tests.

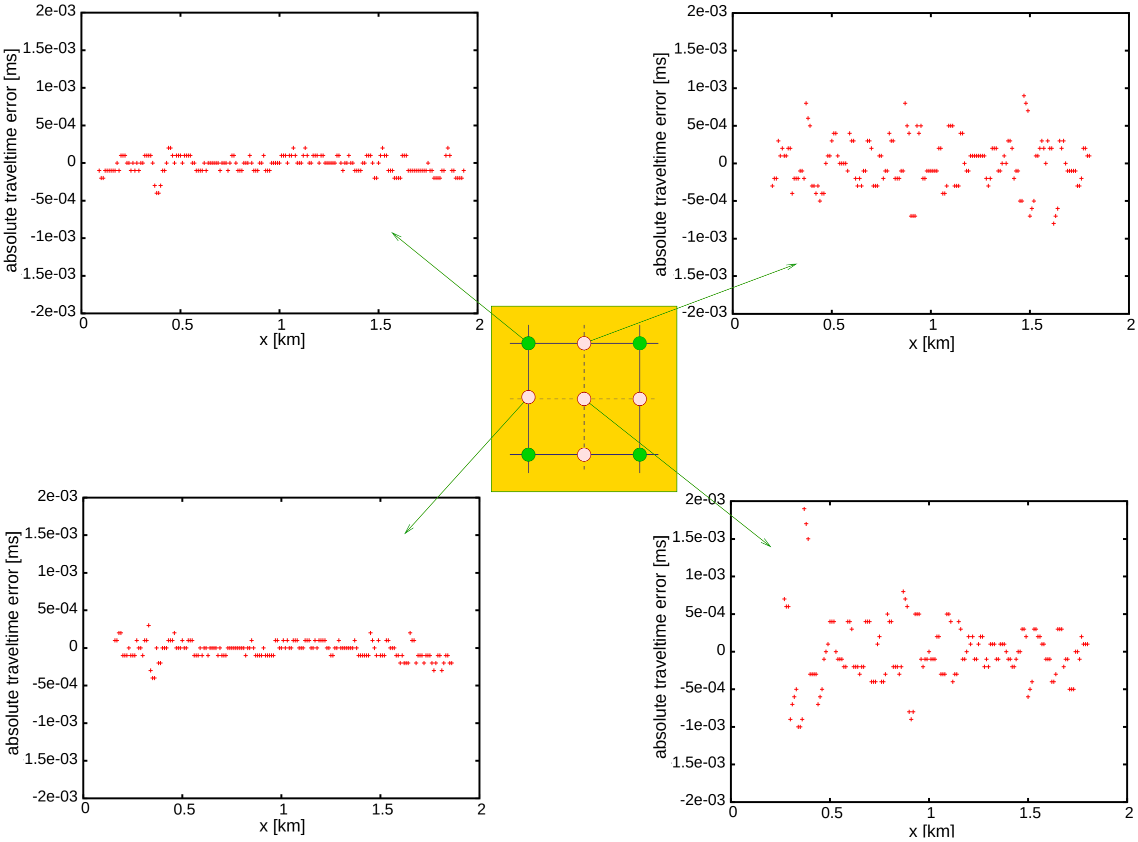

Figure 7.8: Distribution of traveltime errors of traveltimes derived by ray shooting. Upper left: errors for an image point on the coarse grid at $\vec{s}_0 = (1.1, 1.1)$km. Upper right: errors for an image point on the fine grid with $\vec{s} = (1.15, 1.1)$ $\Delta x = 50$m. Lower left: errors for an image point at $\vec{s} = (1.1, 1.15)$ $\Delta z = 50$m. Lower right: Error distribution for an image point on the fine grid with $\vec{s} = (1.15, 1.15)$ $\Delta x = \Delta z = 50$m.

Handling of Triplications

This section deals with the handling of triplicated traveltimes. To demonstrate how the implementation works in the presence of triplications I use an isotropic model with a lens structure (see Figure 7.9), where the velocity from the boundary of the lens (v=4 km/s) decreases towards the center of the lens (v=2 km/s). In this case, the complexity of the velocity model causes multipathing in the propagating wavefields. Consequently, there is more than one way for rays to propagate from the source to certain receivers and hence multiple arrivals from a single source pulse.

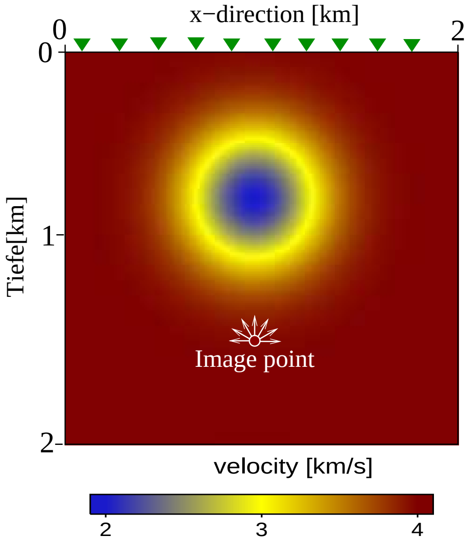

Figure 7.9: The homogeneous isotropic model has a lens structure in its center, where the velocity decreases from the boundary (v=4 km/s) towards the center of the lens (v=2 km/s). By using a constant angle step a fan of rays will be shot from each image point to the surface.

For each image point a fan of rays will be shot to the surface. The left side in Figure 7.10 illustrates that the angle of initial departure increases clockwise, starting in horizontal direction. For instance, a traveltime curve corresponding to an image point that is located below the lens structure in the velocity field like presented on the right-hand side of Figure 7.10. The different colours of the traveltime branches correspond to the symbolically illustrated starting rays on the left side. If a ray crosses his adjacent ray during the propagation the kmah index for this ray increases (see section 2.7). Only if the kmah index for the neighbouring ray is the same as for the actual ray the hyperbolic coefficients will be calculated and thus the traveltime calculation to the receiver position can be done (see section 7.2).

In Figure 7.10 point P_1 and P_2 limit the region with different kmah indices. These points defined in the time domain correspond to caustic points in the depth domain (see section 2.7).

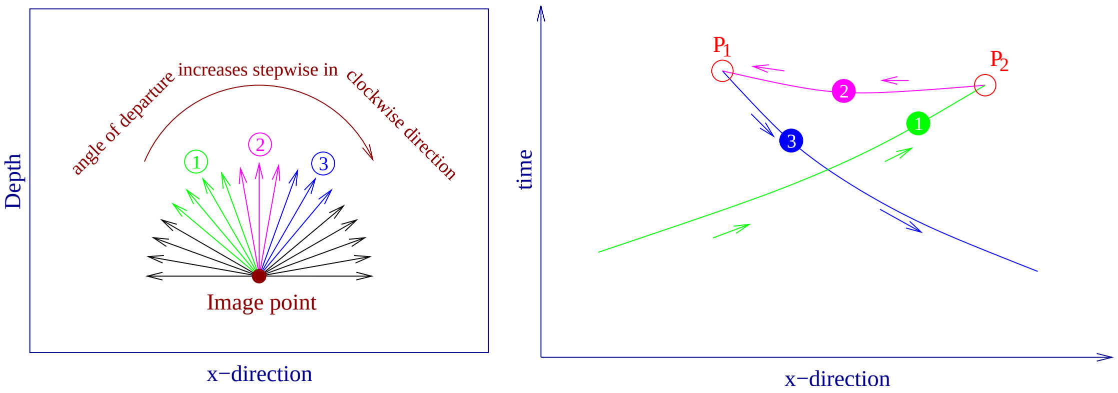

Figure 7.10: In general, the initial ray direction at an image points starts horizontal, then the angle of departure increases clockwise (see left side). The different colours of the initial directions at the image point correspond symbolically to the different traveltime branches (right figure) of the measured traveltime curve at the receivers.

For instance, Figure 7.11 shows exemplarily the ray paths from two different image points to the surface. Both image points are located in a depth of 1.5 km. The x-coordinate in the left figure is chosen to be 0.75 km and in the right figure the x-coordinate is x=1.05 km.

The resulting traveltime curves are presented by the red lines in Figure 7.12. The upper figures correspond to a receiver distance of 50 m, the lower figures show the resulting traveltimes if the receiver spacing is 10 m. Corresponding to the clockwise increasing take off angle at the image point the traveltimes indicated by the green crosses will be interpolated first. Those rays where the kmah index has changed compared to the green area, are used to interpolate the traveltimes which are indicated by the magenta crosses. Finally when the kmah index changes the second time the traveltimes at the blue crosses will be interpolated by using these corresponding rays. The visible

With ray shooting the change in direction is easily detected, and consequently the algorithm is able to separate the branches to interpolate the traveltimes.

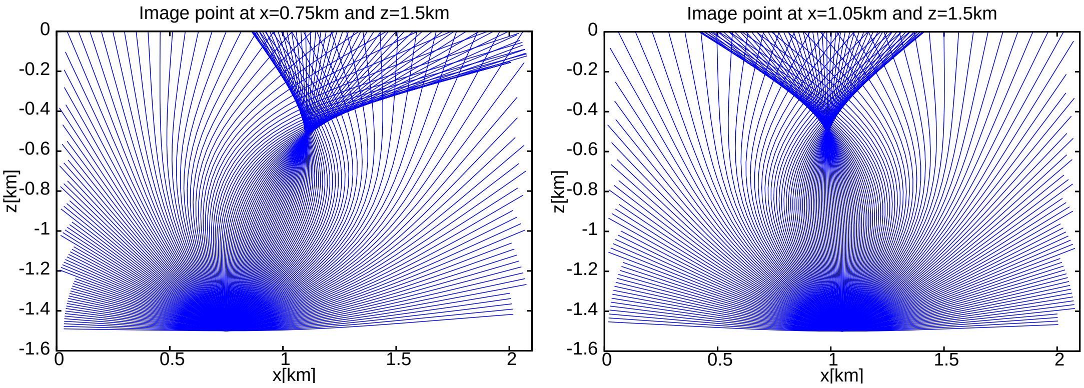

Figure 7.11: Ray paths for two different image points. Left: The image point is located at x=0.75 km and z=1.5 km. Right: The image point is located at x=1.05 km and z=1.5 km.

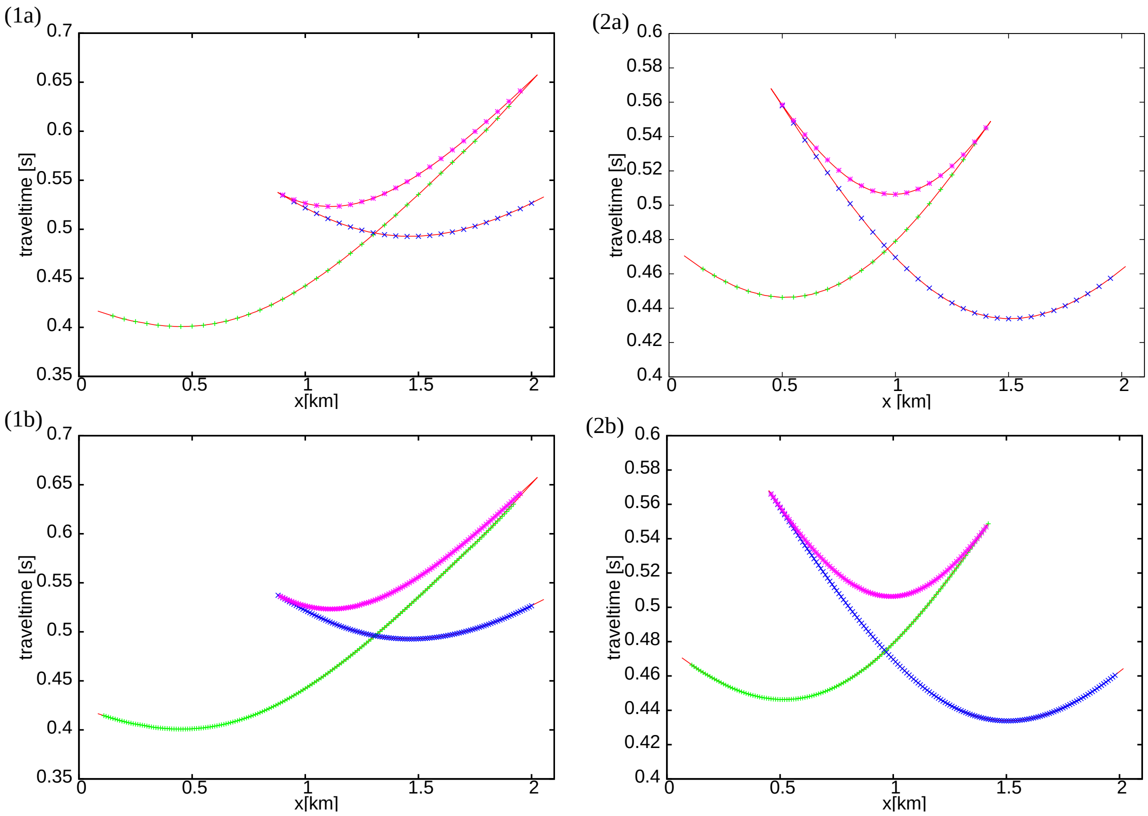

Figure 7.12: The upper figures (1a and 2a) correspond to a receiver distance of 50 m, in comparison the lower figures (1b and 2b) show the resulting traveltimes if the receiver spacing is 10 m. Corresponding to the clockwise increasing take off angle at the image point (see left side in Figure 7.10) the interpolated traveltimes at the receiver positions are indicated by different colours. Note that receivers are only located between 100 m and 2 km.

Chapter 8

Synthetic data example

In the next section I present two synthetic data examples: one anisotropic medium with elliptical symmetry and one more complex isotropic model. For the first anisotropic example, where an elliptical symmetry is assumed, the synthetic seismograms can be calculated analytically (Vanelle, 2002b).

8.1 Anisotropic medium with elliptical symmetry

To verify the migration algorithm synthetic seismograms in a common-shot configuration were computed for the two-layers model. This type of anisotropy was already used for the verification of the accuracy of the wavefront-oriented ray tracing technique. All required quantities to generate ray synthetic seismograms can be calculated analytically (Vanelle, 2002b). We describe our model by the Thomsen parameters $\epsilon = \delta = 0.187$ and $\gamma = 0.51$ and the vertical velocity v_{p0}. The model is shown in Figure 8.1.

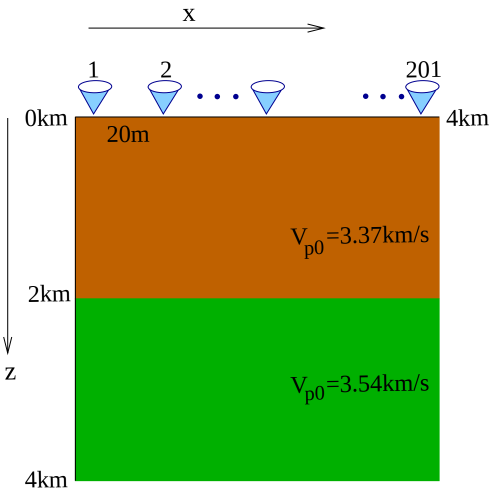

Figure 8.1: The model dimensions for the elliptically anisotropic test model.

The chosen model dimensions are 4 km in x-and z-direction with an input grid spacing of 20 m. The horizontal reflector is assumed to be in 2 km depth. The response of the single shot was received at 201 geophones which are placed every 20 m at the surface. The resulting synthetic shot section is presented in Figure 8.2. The explosion source is supposed to be at the surface and is located at x=1 km. The presented synthetic shot section is computed for the P-wave and a Gabor wavelet is assumed as the source pulse. As described in Chapter 6 the first step during the migration process is to calculate traveltimes on a coarse subsurface grid. In this case the input traveltimes were calculated on a subsurface grid with a grid spacing of 100 m. However, to achieve a satisfactory migration results the traveltimes are required on a finer migration grid. Therefore, by applying the hyperbolic traveltime interpolation the coarse grid is exchanged by a fine migration grid with a grid spacing of 5 m.

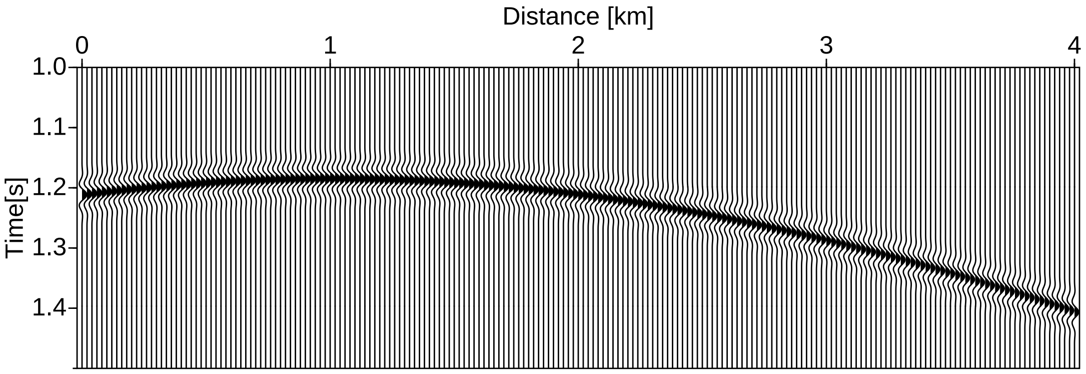

Figure 8.2: Synthetic common-shot section: The receiver spacing is 20 m and the source is located at 1 km.

Figure 8.3 shows the migrated depth section. Due to the limited extent of the receiver line the reflector cannot be imaged in the region of $x < 1$ km and $x > 2.2$ km. The reflector has been migrated to the correct depth. However the reconstruction of the Gabor wavelet cannot be obtained, until true amplitude migration is performed. The hyperbola-shaped events in the migrated section are artefacts caused by the limited extent of the receiver line. They can be suppressed by application of a suitable taper.

The application of the angle-based migration to a simple anisotropic model results in a kinematically correct image of the subsurface where the reflector depth is successfully reconstructed.

Definitely this simple anisotropic model cannot demonstrate the real potential of the traveltime-based angular migration, but it testifies that in general the implementation leads to reasonable results.

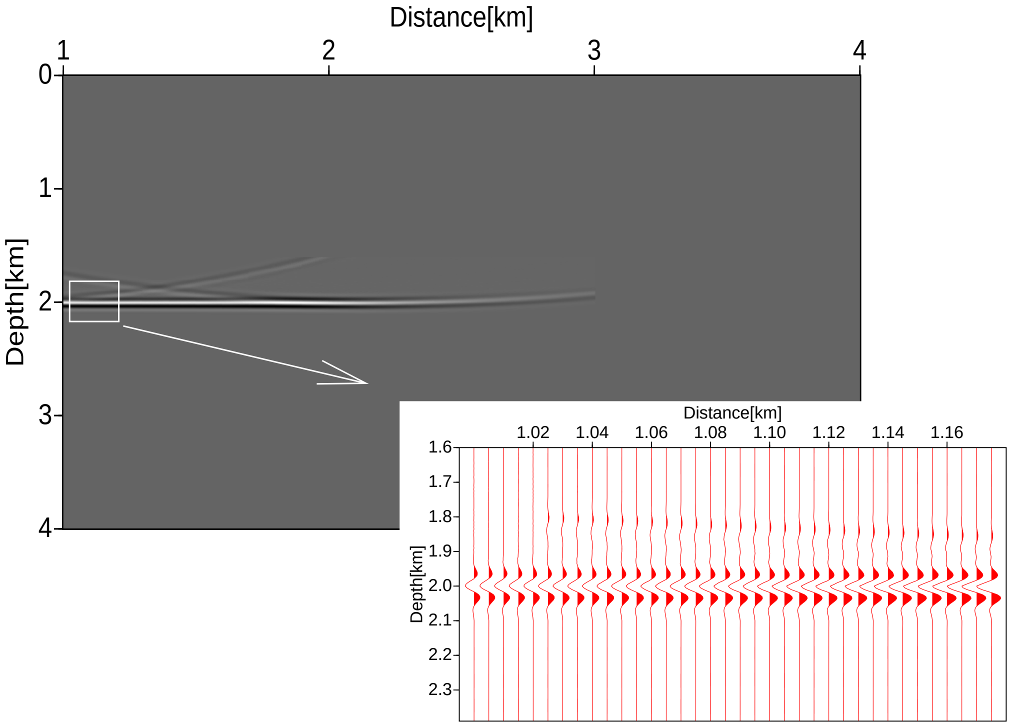

Figure 8.3: Migrated depth section of the common shot section shown in Figure 8.2. The reflector was migrated to the correct depth. The hyperbola-shaped artefact is an aperture effect which can be removed by applying a taper.

The main advantage of the migration with angular parametrisation in comparison to the conventional Kirchhoff migration is that it leads to an even illumination at the image point. This is especially important for media with a complex subsurface structure. Therefore, in the next section the migration for a more complex heterogeneous isotropic medium are presented.

8.2 Isotropic model with high velocity lens

The second test of the migration algorithm is performed in a two-layer model with a strong spherical high-velocity anomaly in the upper layer (Figure 8.4). The constant background velocity in the upper layer is chosen as 3 km/s, and the velocity in the lower layer is 4.5 km/s.

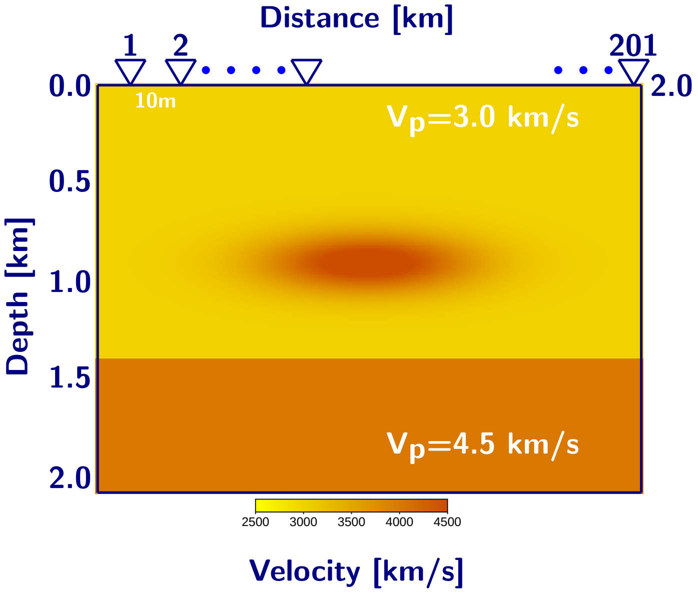

Figure 8.4: 2.5-D subsurface structure: two-layers velocity model with a strong high-velocity anomaly in the upper layer. The P-wave velocity considered to between 3.0 km/s and 4.5 km/s. The center of the lens is located at a depth of 0.8 km and the reflector depth is 1.4 km.

The model dimensions are 2 km in x- and z-direction, in y-direction the model extends to 800 m. The sources are located directly at the registration surface with a spacing of 100 m. Figure 8.5 shows exemplary seismograms for four different shot positions ($x_s = 0.0$ km, $x_s = 1.0$ km, $x_s = 1.5$ km, $x_s = 2.0$ km). The seismograms were computed by a seismic forward modeling algorithm which is based on a Fourier method (Kosloff and Baysal, 1982). The source pulse is assumed to be a Ricker wavelet. In these seismograms three real events are visible, the predominant direct wave, the reflection of the high-velocity anomaly and the reflection of the flat horizon. Additionally, the shot sections comprise a “shadow” beneath the direct wave (for further details see Kosloff and Baysal (1982) and Kosloff and Baysal (1982)).

All computed 21 synthetic shot sections are displayed in Figure 8.6. In these sections the direct wave is muted and the reflection of the lens structure is observed at approximately 0.6-0.7 s and the horizontal reflector at approximately 0.95 s. To get the traveltimes for the migration in the traveltime-based migration ray shooting is performed. Therefore, the velocity model had to be smoothed, here the smoothing operator (see section 4.3) was applied 20-fold.

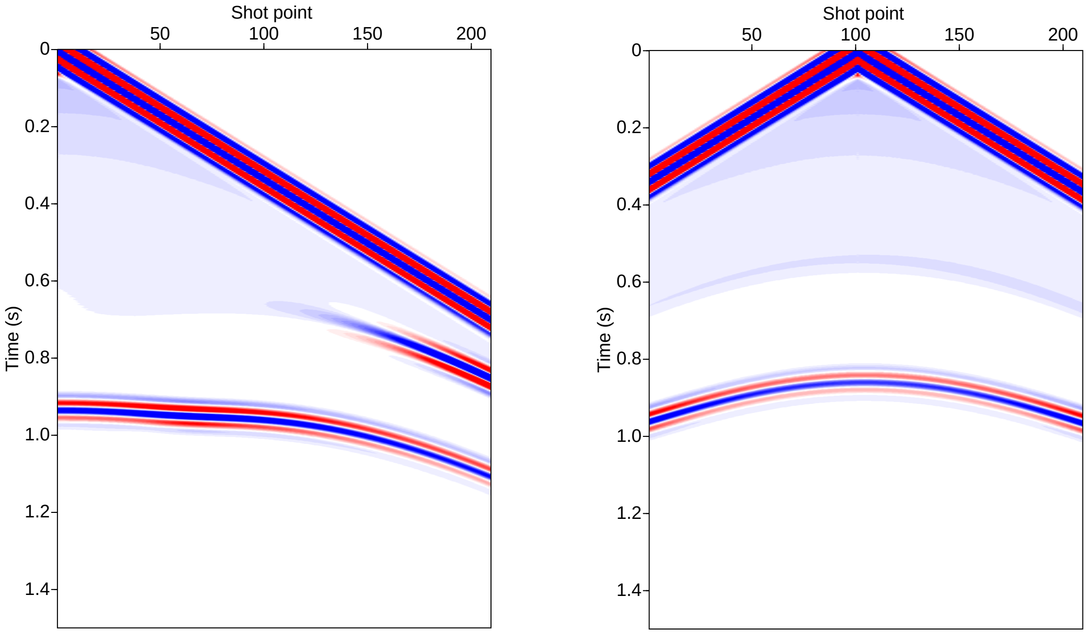

Shot at 0.0 km

Shot at 1.0 km

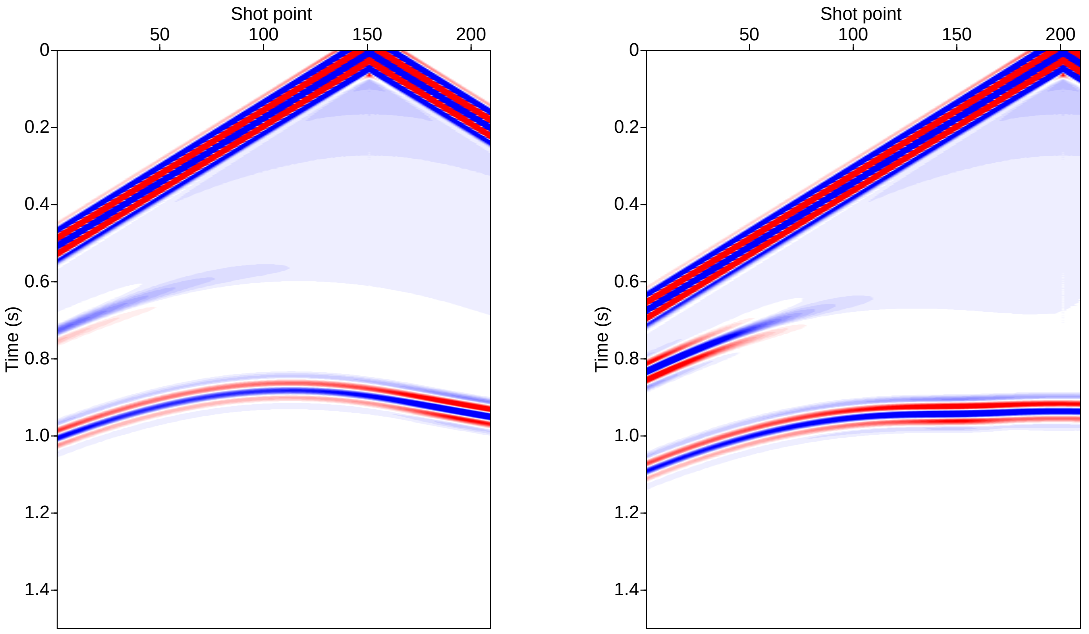

Shot at 1.5 km

Shot at 2.0 km

Figure 8.5: Synthetic common-shot sections: The figure display 4 shots at different shot positions . All figures represent the full response from all receivers, including the direct wave.

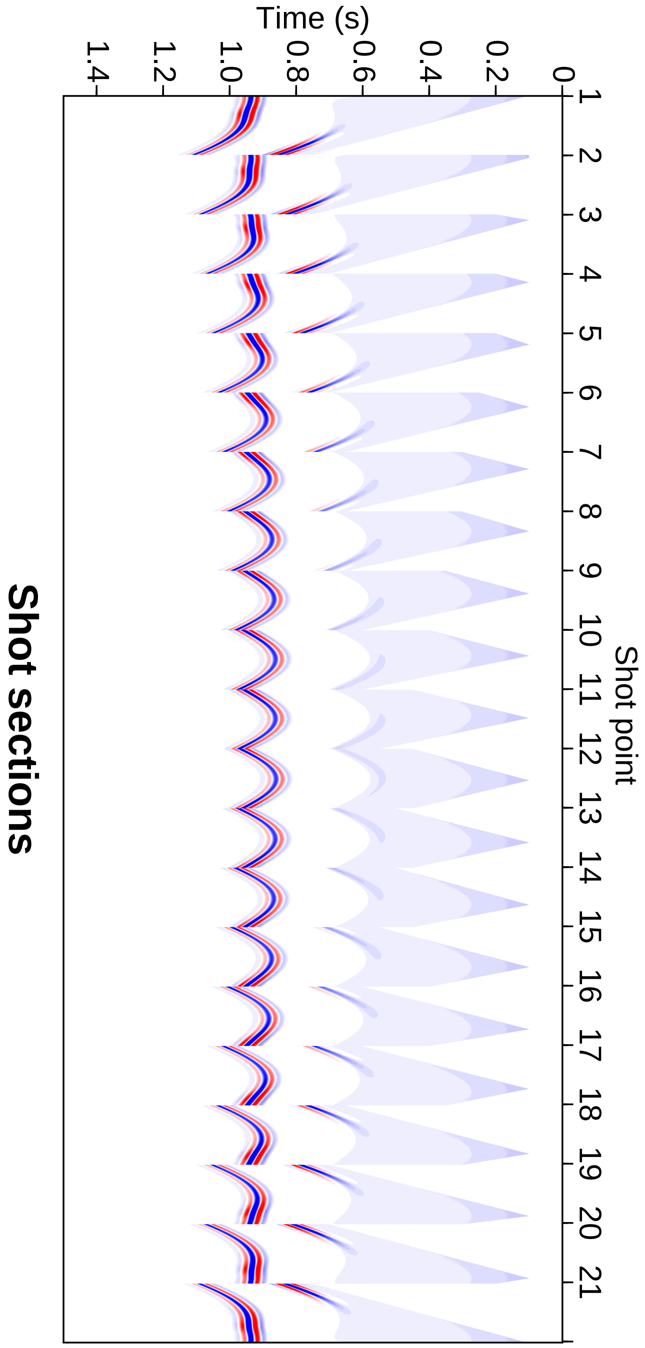

Figure 8.6: Synthetic common-shot sections: The figure display the 21 shots with a source spacing of 100m and the receiver spacing is 10 m. In all sections the direct wave is muted.

First a Kirchhoff migration is performed by Seismic Unix (sukdmig). The conventional migration needs a large number of traveltime tables. Figure 8.8 presents two different migration results. The subsurface structure in the upper figure is computed by using traveltimes generated by Seismic Unix. In comparison the lower figure illustrates the migration result by using traveltime tables calculated by the wavefront-oriented ray tracing procedure.

In the upper image, it can be observed that the quality of the migrated image near the boundary of the lens structure is poor in comparison to the lower image. This inaccuracies in the migrated image can be attributed to the inaccuracies due to the traveltime computation (see Figure 8.7).

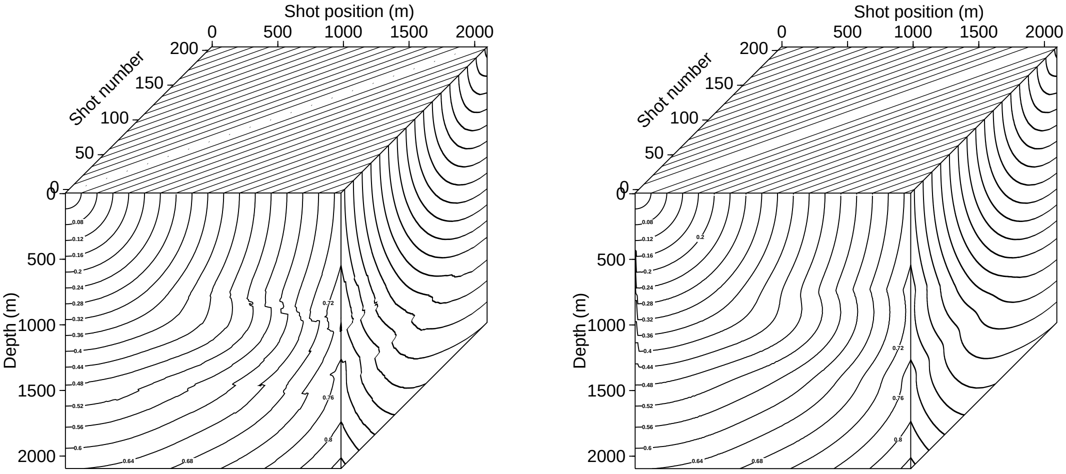

Figure 8.7: Left: Traveltime tables calculated by Seismic Unix. Right: Traveltimes computed by the wavefront-oriented ray tracing technique.

As it can be observed on the right-hand side of Figure 8.7. the traveltime calculation by the wavefront-oriented ray tracing is more accurate and leads to smooth isochrones even in the vicinity of the high-velocity structure. Consequently, by applying the same migration algorithm these traveltime tables lead to a better subsurface image (see Figure 8.8).

Finally Figure 8.9 displays the migrated image by the traveltime-based migration in the angular domain. In both migrated images the reflector is migrated to the correct position in 1.4 km depth. Furthermore the traveltime-based migration images the lens-shaped velocity structure more clearly. The green ellipse in both lower figures indicates roughly the position of the high-velocity anomaly, of course there are no sharp boundaries in the velocity model.

Now the same input data are migrated, but in comparison to the previous data set, here random white noise is added to the shot sections (see Figure 8.10). The chosen signal-to-noise (S/N) ratio is 2.

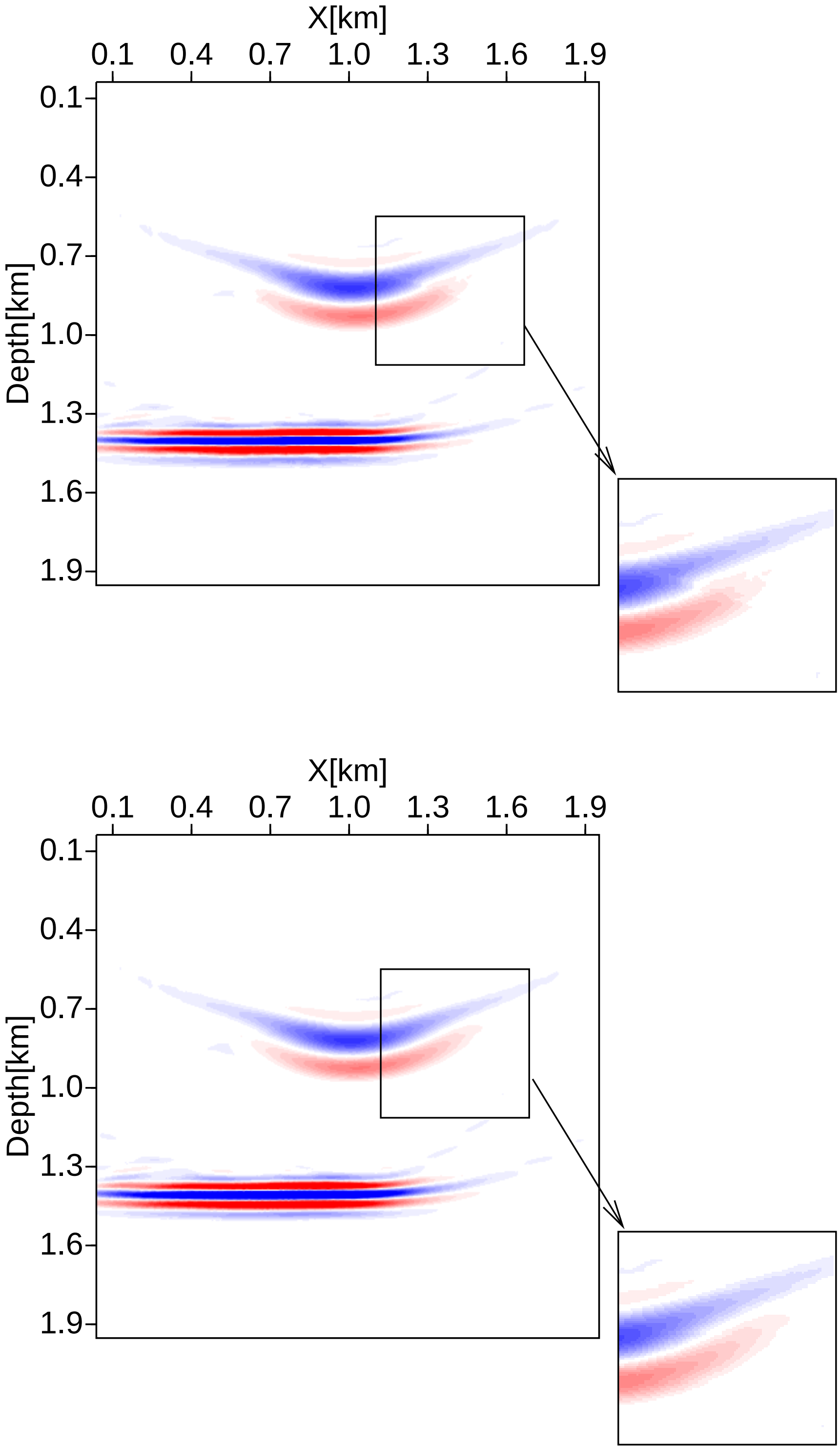

Figure 8.8: The figure show two migration results of the classical Kirchhoff migration. The upper migration result is computed by traveltime tables calculated by Seismic Unix, whereas the lower figure displays the migration result for traveltimes calculated by the wavefront oriented ray tracing algorithm.

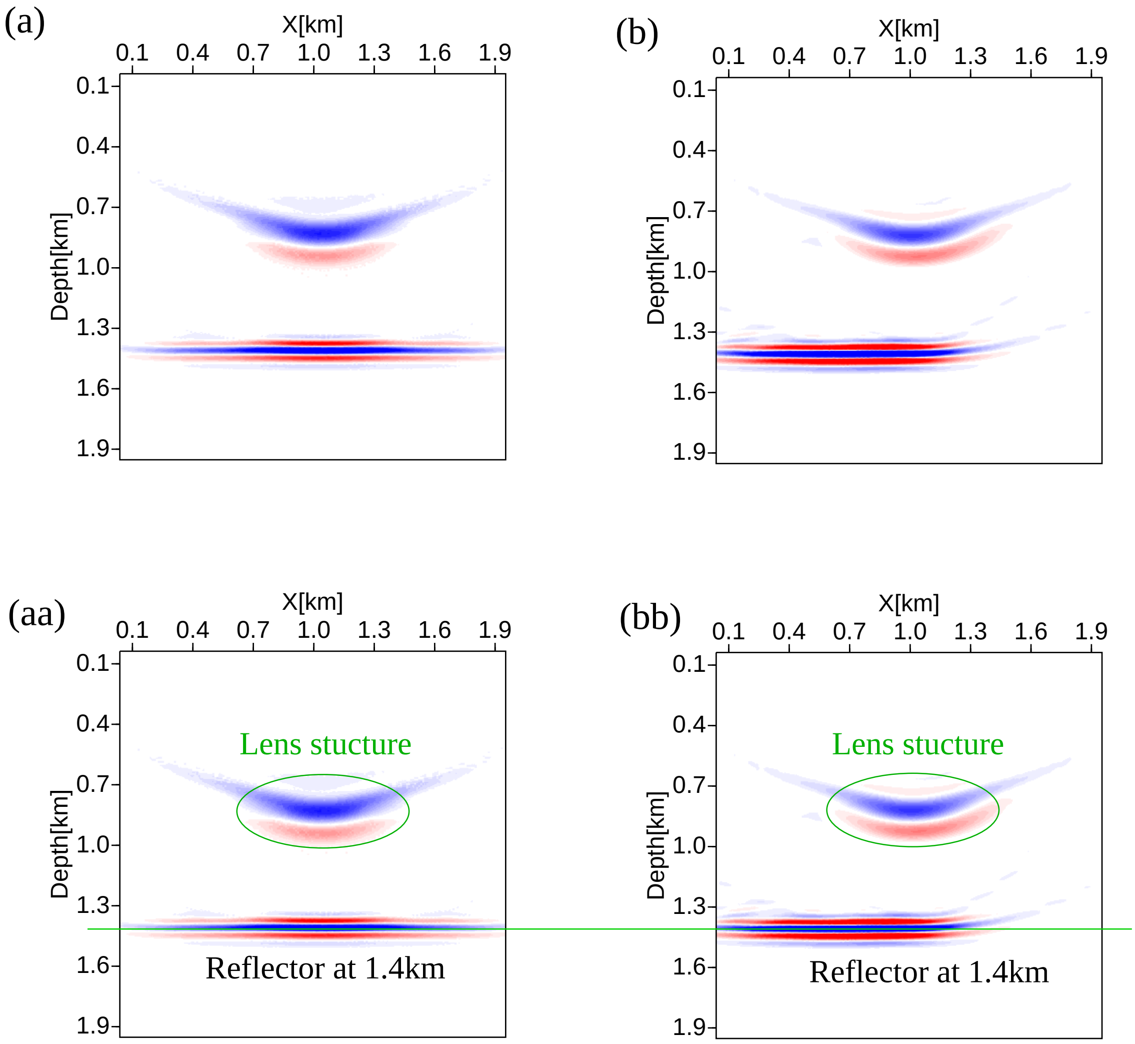

Figure 8.9: Left: Migration result of the traveltime-based migration in the angular domain (a,aa). Right: Migration result of the Seismic Unix Kirchhoff migration (b,bb). Lower: the horizontal green line indicates the position of the reflector and the green ellipses illustrate the position of the lens-shaped structure.

The same input traveltime tables calculated by the wavefront-oriented ray tracing are used and the migration result is displayed on the right side of Figure 8.11. In comparison the left side of Figure 8.11 gives the migration result of the traveltime-based migration in the angle domain. As in the previous example for both schemes the reflector is migrated to the correct depth.

As expected the noise in the data have different influences. In the Seismic Unix Kirchhoff migration in some regions the noise superposes constructively in other destructively. In praxis, the quality of the migrated section can be significantly increased by applying a filter operation before migration. Corresponding to the noise-free data example the lens-shaped velocity inclusion is better visible in the image of the traveltime-based migration algorithm.

In this section I have presented a traveltime-based implementation for the migration with angular parametrisation. The traveltimes are computed on coarse grids, leading to considerable savings in storage. Subsequent hyperbolic interpolation leads to the traveltimes on the required fine migration grid. Application of angle-based migration to a simple anisotropic model resulted in a kinematically correct image of the subsurface where the reflector depth was successfully reconstructed. As a second example the migrated image for a more complex isotropic model was presented. Here, the reflector depth and the lens-shaped structure were correctly imaged.

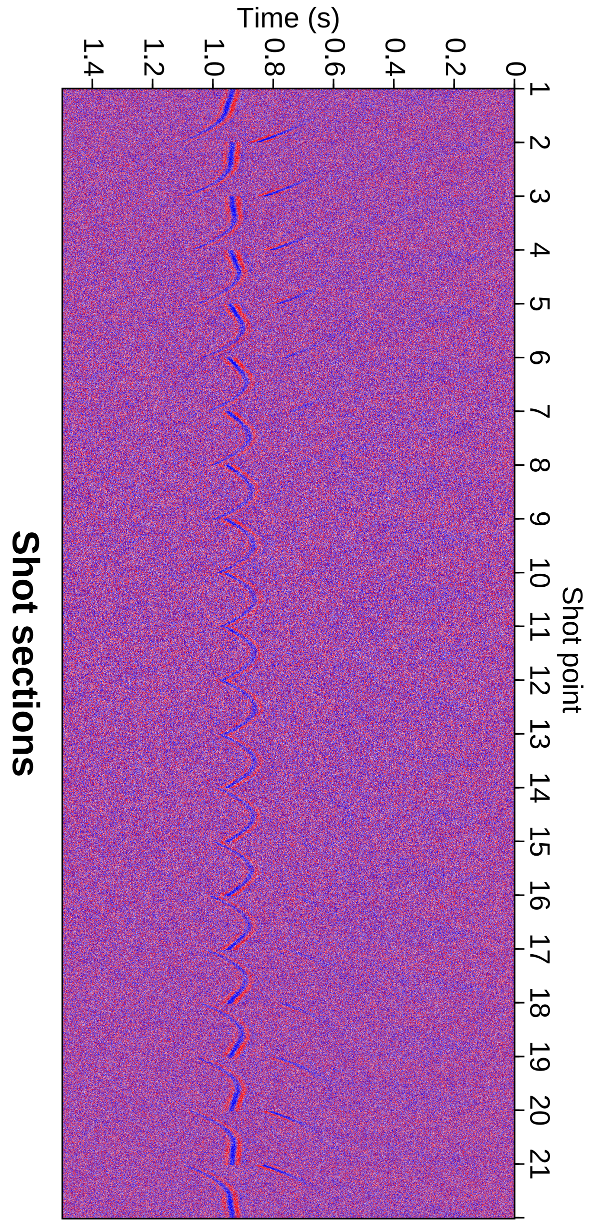

Figure 8.10: Synthetic common-shot sections with added random white noise: The figure displays the 21 shots with a source spacing of 100 m and the receiver spacing is 10 m. In all sections the direct wave is muted. The signal-to-noise (S/N) ratio is 2.

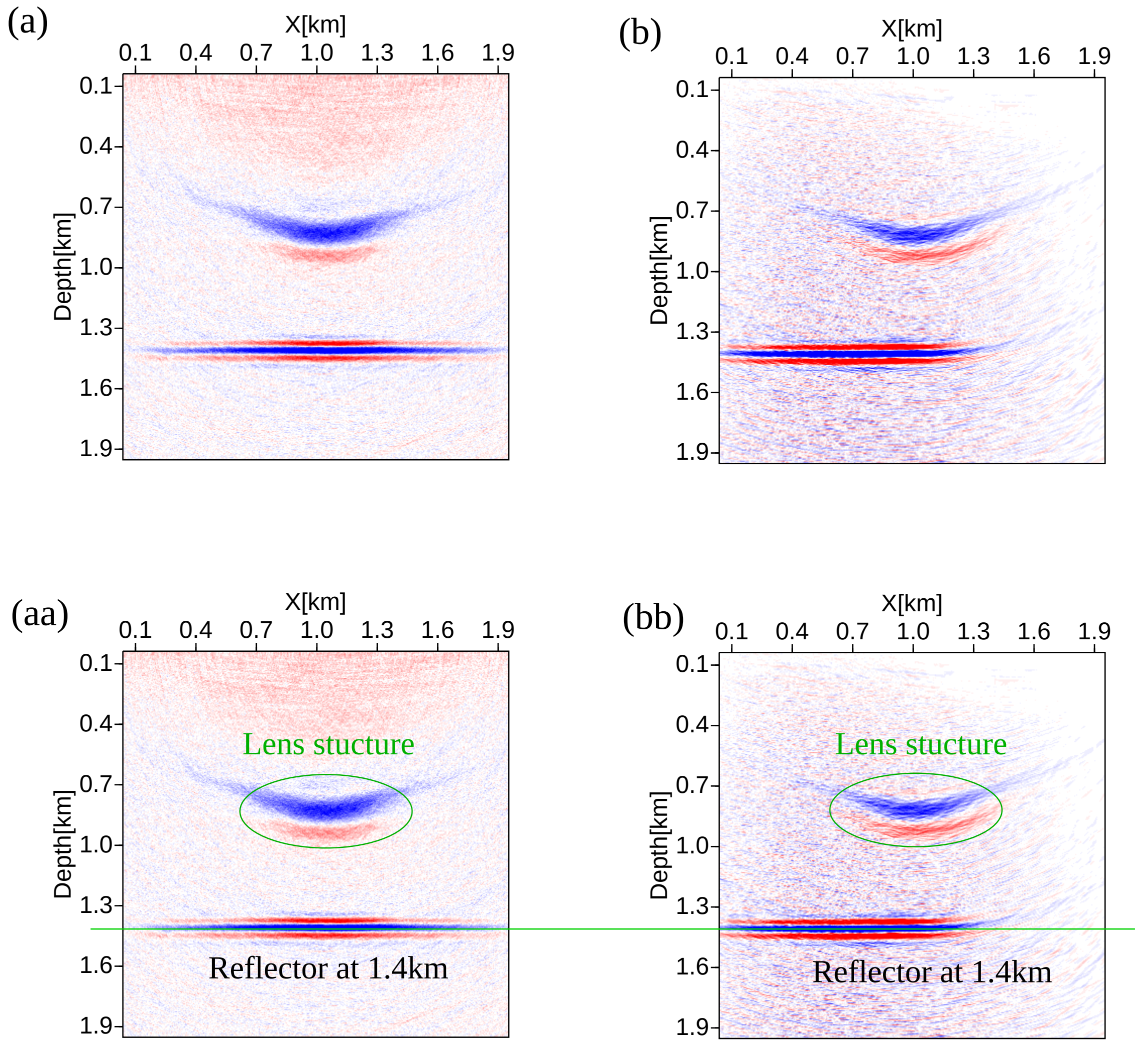

Figure 8.11: Left: Migration result of the traveltime-based migration in the angular domain (a,aa). Right: Migration result of the Seismic Unix Kirchhoff migration (b,bb). Lower: the horizontal green line indicates the position of the reflector and the green ellipses illustrate the position of the lens-shaped structure.

Chapter 9

Conclusion and outlook

For seismic imaging of complex 3-D structures by prestack Kirchhoff depth migration (PKDM) many traveltime tables have to be calculated. For the efficient computation of multivalued traveltimes in 3-D anisotropic media I have implemented an algorithm for wavefront-oriented ray tracing.

The presented wavefront-oriented ray tracing implementation for anisotropic media is based on the already existing algorithm for the isotropic case (Coman, 2003). The classical wavefront construction (Vinje et al., 1993a; Lambaré et al., 1996) was modified by introducing new insertion criteria and a new strategy for the interpolation of traveltimes to grid points.

The initial model, e.g. velocities or elastic parameters are given on the discrete input model. During the propagation of wavefronts these quantities are needed at arbitrary positions. This requires an interpolation. Instead of the trilinear interpolation used by Coman (2003), I have implemented a Cardinal spline interpolation. This method preserve all advantages of the classical spline interpolation, e.g. accuracy, continuity of the derivatives, but is also an efficient implementation. In the anisotropic case, we have 21 elastic parameters instead of one velocity at each grid point, therefore a fast interpolation is essential if anisotropy is present.

The accuracy of the implementation was demonstrated for an elliptically anisotropic medium. The observed errors are negligible. To show the high potential of the wavefront-oriented ray tracing I presented several models with more complex subsurface structures and compared the results to an alternative technique, the finite differences perturbation method by (Soukina, 2004).
Not only the traveltime tables for the qP-waves are computed, for all presented anisotropic media the qS-waves are presented. As discussed in this work if the model comprises shear wave singularities the actual implementation of the wavefront-oriented ray tracing technique fails. However, if the algorithm a priori knows that the medium is assumed to be transversely isotropic it is possible to formulate two different eikonal equations, one for

the SH-wave and one for the qP- and the qSV-wave (personal discussion Einar Iversen). If we observe a shear wave singularity the slowness vector for both shear waves are equal and cannot be used to distinguish between them. If the phase velocity surfaces crosse each other, the direction of the group velocity vector differs and can be used to distinguish between both shear waves. If the two phase velocity surfaces are tangent to each other in some cases the polarization vector can be used to distinguish between both shear wave modes. Sometimes numerical problems occur in the vicinity of caustics. Nevertheless, all observed problems in the implementation are due to the traveltime interpolation from wavefronts to grid points or are due restrictions due to the basic theory.
The traveltime calculation by the wavefront-oriented ray tracing requires several input quantities, e.g. the model dimension or the ray tracing parameters (e.g., traveltime step). Therefore, I have enhanced the user-friendly graphical interface for the wavefront-oriented ray tracing to the anisotropic case.

In the second part, I have presented a traveltime-based implementation for the migration with angular parametrisation. The traveltimes are computed on coarse grids, leading to considerable savings in storage. Subsequent hyperbolic interpolation leads to the traveltimes on the required fine migration grid. Numerical examples confirm the quality of the traveltime interpolation. Applications of angle-based migration to a relatively simple anisotropic model resulted in a kinematically correct image of the subsurface where the reflector depth was successfully reconstructed.

The rayshooting technique is one of the fastest methods to calculate traveltimes. The time consuming part is to get the traveltime from a certain source to a predefined receiver position, because this requires a large number of iterations for rays with slightly different directions until the desired ray connecting source and receiver is found. To overcome this disadvantage I have modified the hyperbolic traveltime expansion to an irregular grid and applied this technique to calculate the traveltimes from any subsurface point to any receiver position.

The main advantage of the migration with angular parametrisation in comparison to conventional migration is that it leads to an even illumination at the image point. This is especially important for media with a complex subsurface structure. Therefore, a comparison of the migration results between traveltime-based migration and angular parametrisation with conventional Kirchhoff migration for heterogeneous complex 2-D models was performed. For both presented examples we achieve a kinematically correct image of the subsurface where the reflector depth is successfully reconstructed. The results of both models are auspicious to apply the method to more complex subsurface structures, especially a model with a low-velocity anomaly, because then multi arrival traveltimes will be registered at the receivers.

Furthermore, the consideration of migration amplitudes is an important future aspect. The output of a true-amplitude migration serves as input for AVO analysis, a key technique for reservoir characterization. True-amplitude Kirchhoff migration in 2.5-D media additionally requires maps of amplitudes, out-of-plane spreading factors, and takeoff angles; these quantities are necessary for calculating the true-amplitude weight term in the summation.

Future work will therefore be addressed to the extension of the angle-based implementation to true-amplitude migration in anisotropic media. This implementation will also be based on traveltimes as the only input information that is needed for the determination of the true-amplitude weights. Vanelle and Gajewski (2002b) introduced a strategy to calculate the migration weight alone from traveltimes and therefore significantly reduce the requirements in computational time and particularly storage.

Bibliography

Åstebøl, K. (1994). Easy-to-use modeling - 3d ray field propagation in open ray models. *EAGE/SEG summer workshop, Extended Abstracts, paper G015.*

Beydoun, W., Harnitzsch, C., and Jin, S. (1993). Why migrate before AVO? A simple example. *Ann. Mtg., Eur. Assn. Expl. Geophys., Extended Abstracts*, B044.

Bleistein, N. (1987). On imaging of reflectors in the earth. *Geophysics*, 52:931–942.

Bortfeld, R. (1989). Geometrical ray theory: rays and traveltimes in seismic systems (second-order approximations of traveltimes). *Geophysics*, 54:342–349.

Brandsberg-Dahl, S., de Hoop, M., and Ursin, B. (2001). Imaging-inversion with focusing in dip. *63th Ann. Mtg., Eur. Assn. Expl. Geophys.*, page Session: P079.

Brandsberg-Dahl, S., de Hoop, M., and Ursin, B. (2003). Focusing in dip and AVA compensation on scattering-angle/azimuth common image gathers. *Geophysics*, 68:232–254.

Castagna, J. P. and Backus, M. (1993). *Offset-Dependent Reflectivity - Theory and Practice of AVO Analysis*. Society of Exploration Geophysicists.

Červený, V. (1972). Seismic Rays and Ray Intensities in Inhomogeneous Anisotropic Media. *The Geophysical Journal of the Royal Astronomical Society*, 29:1–13.

Červený, V. (1985). *The application of ray tracing to the numerical modelling of seismic wavefields in complex structures*. Geophysical Press.

Červený, V. (1989). Ray tracing in factorized anisotropic inhomogeneous media . *Geophysical Journal International*, 99:91–100.

Červený, V. (2001). *Seismic Ray Theory*. Cambridge University Press.

Červený, V. and Hron, F. (1980). The ray series method and dynamic ray-tracing system for three-dimensional inhomogeneous media. *Bulletin of the Seismological Society of America*, 70:47–77.

Chapman, C. and Shearer, P. (1989). Ray tracing in azimuthally anisotropic media - 2.quasi-shear wave coupling. *Geophysical Journal*, 96:65–83.

Cholet, J. and Richard, H. (1954). A test on elastic anisotropy measurement at berraine. *Geophysical Prospecting*, 2:232–246.

Coman, R. (2003). *Computation of multivalued traveltimes in three-dimensional heterogeneous media, PhD thesis.* University of Hamburg.

Daley, P. and Hron, F. (1979). Reflection and transmission coefficients for seismic waves in ellipsoidally anisotropic media. *Geophysics*, 44:27–38.

deHoop, M., Spencer, C., and Burridge, R. (1999). The resolving power of seismic amplitude data: An anisotropic inversion/migration approach. *Geophysics*, 64:852–873.

Ettrich, N. and Gajewski, D. (1996). Wavefront construction in smooth media for prestack depth migration. *Pure Appl. Geophys.*, 148:481–502.

Ettrich, N. and Gajewski, D. (1998). Traveltime computation by perturbation with FD-eikonal solvers in isotropic and weakly anisotropic media. *Geophysics*, 63:1066–1078.

Gajewski, D. (1998). Determining the ray propagator from traveltimes. *68th Ann. Internat. Mtg., Soc. Expl. Geophys, Expanded Abstracts*, pages 1900–1903.

Gajewski, D., Coman, R., and Vanelle, C. (2002). Amplitude preserving Kirchhoff migration: a traveltime based strategy. *Stud. geophys. geod.*, 46:193–211.

Gajewski, D. and Pšenčik, I. (1987). Computation of high-frequency seismic wavefields in 3-D laterally inhomogeneous anisotropic media. *The Geophysical Journal of the Royal Astronomical Society*, 91:383–411.

Gajewski, D. and Pšenčik, I. (1990). Vertical seismic profile synthetics by dynamic ray tracing in laterally varying layered anisotropic structures. *Journal of Geophysical Research*, 95:11301–11315.

Gassman, F. (1964). Introduction to seismic travel time methods in anisotropic media. *Pure Appl. Geophys.*, 58:53–112.

Gjøystdal, H., Reinhardsen, J., and Ursin, B. (1984). Traveltime and wavefront curvature calculations in three dimensional inhomogeneous layred media with curved interfaces. *Geophysics*, 49:1466–1494.

Gray, S., Etgen, J., Dellinger, J., and Whitmore, D. (2001). Seismic migration problems and solutions. *Geophysics*, 66:1622–1640.

Hawkins, K., Leggot, R., and Williams, G. (2002). More accurate reservoir imaging through anisotropic pre-sdm. *CSEG Converence.*

Helbig, K. (1956). Die Ausbreitung elastischer Wellen in anisotropen Medien. *Geophysical Prospecting*, 4:70–81.

Helbig, K. (1983). Elliptical anisotropy - its significance and meaning. *Geophysics*, 48:825–832.

Helbig, K. and Treitel, S., editor (1994). *Foundations of Anisotropy for Exploration Seismics*. Pergamon.

Julian, B. and Gubbins, D. (1977). Three-dimensional seismic ray tracing. *Journal of Geophysics*, 43:1065–1073.

Kosloff, D. and Baysal, E. (1982). Forward modeling by a fourier method. *Geophysics*, 47:1402–1412.

Kravtsov, Y. and Orlov, Y. (1990). *Geometrical optics of inhomogeneous media*. Springer Verlag.

Lambaré, G., Lucio, P., and Hanyga, A. (1996). Two-dimensional multivalued traveltime and amplitude maps by uniform sampling of a ray field. *Geophysical Journal International*, 125:584–598.

Lambaré, G., Virieux, J., Madariaga, S., and Jin, S. (1992). Iterative asymptotic inversion in the acoustic approximation. *Geophysics*, 57:1138–1154.

Larner, K. and Tsvankin, I. (1995). P-wave anisotropy: Its practical estimation and importance in processing and interpretation of seismic data. *65th Ann. Internat. Mtg., Soc. Expl. Geophys, Expanded Abstracts*, pages 1502–1505.

Laurain, R., Vinje, V., and Strand, C. (2003). Simulated migration amplitude: modeling amplitude anomalies of psdm in a real north sea case. *Expanded Abstracts, SEG 73rd Annual Meeting, Dallas*, pages 917–920.

Lecomte, I. (1993). Finite difference calculation of first traveltimes in anisotropic media. *Geophysical Journal International*, 113:318–342.

Leidenfrost, A., Ettrich, N., Gajewski, D., and Kosloff, D. (1999). Comparison of six different methods for calculating traveltimes. *Geophysical Prospecting*, 47:269–297.

Lucio, P., Lambaré, G., and Hanyga, A. (1996). 3d multivalued travel time and amplitude maps. *Pure and Applied Geophysics*, 148:449–479.

Mensch, T. and Rasolofosaon, P. (1997). Elastic-wave velocities in anisotropic media of arbitrary symmetry - generalization of Thomsen's parameters ϵ, δ, γ. *Geophysical Journal International*, 128:43–64.

Moser, T. (1991). Shortest path calculation of seismic rays. *Geophysics*, 56:59–67.

Mufti, I., Pita, J., and Huntley, A. (1991). Finite-difference depth migration of exploration-scale 3-d seismic data. *Geophysics*, 61:776–794.

Press, W., Teukolsky, S., Vettering, W., and Flannery, B. (1992). *Numerical recipes in C: the art of scientific computing*. Cambridge University Press.

Reshef, M. (1991). Prestack depth imaging of three-dimensional shot gathers. *Geophysics*, 56:1158–1163.

Reshef, M. and Kosloff, D. (1986). Migration of common shot gathers. *Geophysics*, 51:324–331.

Richards, T. C. (1960). Wide angle reflections and their applications to finding limestone structures in the foolhills of western canada. *Geophysics*, 25:385–407.

Rössl, C., Kobbelt, L., and Seidel, H. (2000). Extraction of feature lines on triangulated surfaces using morphological operators. *Smart Graphics 2000, AAAI Spring Symposium. Stanford University*, pages p.71–75.

Saito, H. (1989). Traveltimes and raypaths of first-arrival seismic waves: Computation method based on huygens' principle. *59th SEG meeting, Dallas, Expanded Abstracts*, pages 1024–1027.

Sayers, C. (1994). The elastic anisotropy of shales. *Journal of Geophysical Research*, 116:799–805.

Schleicher, J., Tygel, M., Hubral, P., and Jaya, M. (1993). Parabolic and hyperbolic paraxial two-point traveltimes in 3D media. *Geophysical Prospecting*, 41:495–513.

Schultz, M. (1973). *Spline Analysis zur Konstruktion glatter Kurven und Flächen.* Prentice-Hall Series in Automatic Computation.

Soukina, S.M. Gajewski, D. and Kashtan, B. (2001). Determination of weak anisotropy parameters using traveltimes and polarisations. *65th EAGE Meeting and Technical Exhibition, Expanded Abstracts, P-003*, pages 254–267.

Soukina, S. (2004). *Modeling and inversion in weakly anisotropic media.* Universität Hamburg, PhD thesis.

Soukina, S. and Gajewski, D. (2003). A traveltime computation in 3-D anisotropic media by a finite-difference perturbation method. *65th EAGE Meeting and Technical Exhibition, Expanded Abstracts,*.

Spitz, S. (1991). Seismic trace interpolation in the f-x domain. *Geophysics*, pages 785–794.

Thomsen, L. (1986). Weak elastic anisotropy. *Geophysics*, 51:1954–1966.

Thomsen, L., editor (2002). *Understanding Seismic Anisotropy in Exploration and Exploitation.* EAGE.

Thomson, C. and Gubbins, D. (1982). Three-dimensional lithospheric modelling at NORSAR: linearity of the method and amplitude variations from the anomalies. *The Geophysical Journal of the Royal Astronomical Society*, 71:1–36.

Tsvankin, I. (2001). *Seismic Signatures and Analysis of Reflection Data in Anisotropic Media.* Pergamon.

Tura, A., Hanitzsch, C., and Calandra, H. (1997). 3-D AVO migration/inversion of field data. *Journal of Seismic Exploration*, 6:117–125.

Ursin, B. (1982). Quadratic wavefront and traveltime approximations in inhomogeneous layered media with curved interfaces. *Geophysics*, 47:1012–1021.

Vanelle, C. (2002a). *Traveltime-based true-amplitude migration, PhD thesis*. University of Hamburg.

Vanelle, C. (2002b). A tutorial on elliptical anisotropy. *6th Annual WIT report*.

Vanelle, C. (2005). Short note filling the gaps in ray traveltime maps. *submitted in Geophysics*.

Vanelle, C. and Gajewski, D. (2002a). Second-order interpolation of traveltimes. *Geophysical Prospecting*, 50:73–83.

Vanelle, C. and Gajewski, D. (2002b). True-amplitude migration weights from traveltimes. *Pure and Applied Geophysics*, 159.

Vidale, J. (1988). Finite-difference calculation of traveltimes. 78:6:2062–2076.

Vinje, V., Iversen, E., Åstebøl, K., and Gjøystdal, H. (1996). Estimation of multivalued arrivals in 3D models using wavefront construction- Part I. *Geophysical Prospecting*, 44:819–842.

Vinje, V., Iversen, E., and Gjøystdal, H. (1993a). Estimation of multivalued arrivals in 3d models using wavefront construction. *55th EAGE meeting, Stavanger, Norway, Expanded Abstracts*, paper B019.

Vinje, V., Iversen, E., and Gjøystdal, H. (1993b). Traveltime and amplitude estimation using wavefront construction. *Geophysics*, 58:8:1157–1166.

Winterstein, D. (1986). Anisotropy effects in p-wave and sh-wave stacking velocities contain information on lithology. *Geophysics*, 51:661–672.

Winterstein, D. and Meadows, M. (1991). Shear-wave polarisations and subsurface stress directions at lost hills filed. *Geophysics*, 56:1331–1348.

Xu, S., Chauris, H., Lambaré, G., and Noble, M. (1998). Common angle image gather: a strategy for imaging complex media. *Ann. Internat. Mtg., Soc. Expl. Geophys., Expanded Abstract*, pages 1704–1707.

Xu, S., Chauris, H., Lambaré, G., and Noble, M. (2001). Common angle image gather: a strategy for imaging complex media. *Geophysics*, Vol. 66:1877–1894.

Appendix A

Hermite and Cubic spline interpolation

The Cardinal splines used in this work to interpolate the model parameters are based on the general Hermite interpolation combined with the Cubic splines. A more detailed overview of the theory of the Cubic Hermite interpolation can be found in Schultz (1973). To explain the basic principles of the interpolation algorithm the formulas are shown only for a one-dimensional function, but the extension to the 3D case is straight forward.
The function values f_i and the corresponding derivatives $f_i^{'}$ are known at a set of points $x_i = x_1, x_2, \dots x_N$. Here, an equidistant spacing Δx is assumed with $[x_i = \Delta x(i-1), i = 1, N]$. Moreover, the second-order derivatives need to be continuous.
Then, the Hermite interpolation reads (Schultz, 1973):

$$f(x) = \sum_{i=1}^{N} f_i H(\frac{x}{\Delta x} - i - 1) + f_i^{'} \Delta x \, H_1(\frac{x}{\Delta x} - i - 1), \tag{A.1}$$

where $H(x)$ is given by (see also Figure A.1):

$$H(x) = \begin{cases} -x^3 - 4x^2 + 1 & \text{if} \quad -1 \le x \le 0, \\ 2x^3 - 3x^2 + 1 & \text{if} \quad 0 \le x \le 1, \\ 0 & \text{else}, \end{cases} \tag{A.2}$$

and $H_1(x)$

$$H_1(x) = \begin{cases} x(x+1)^2 & \text{if} \quad -1 \le x \le 0, \\ x(1-x)^2 & \text{if} \quad 0 \le x \le 1, \\ 0 & \text{else}. \end{cases} \tag{A.3}$$

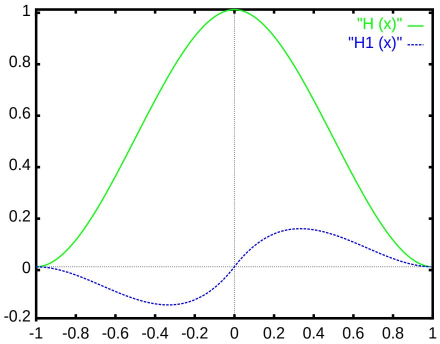

Figure A.1: The figure shows the two functions $H(x)$ and $H_1(x)$ used for the Hermite interpolation.

The Hermite interpolation is local, because for x within the interval defined by $\Delta x\ (i-1) \leq x \leq \Delta x\ i$ only $f_i, f_i^{'}, f_{i+1}$ and $f_{i+1}^{'}$ are taken into account for the interpolation. If the derivatives are unknown the following relation can be used:

$$f_{i-1}^{'} + 4f_i^{'} + f_{i+1}^{'} = 3(\Delta x)^{-1}(f_{i+1} - f_{i-1}) \tag{A.4}$$

This relation is valid because of the continuity of the second derivatives. After the definition of the boundary values at $i = 1$ and $i = N$ the equation system (A.4) can be solved. For x within the interval $\Delta x(i-1) \leq x \leq \Delta x$ the four surrounding function values are given by

$$F_k = f_{i-3+k}; \quad k = 1, 2, 3, 4. \tag{A.5}$$

The Hermite interpolation formula (A.1) than reads:

$$f(x) = \sum_{k=1}^{4} F_k H(\frac{x}{\Delta x} - i + 3 - k) + F_k^{'} \Delta x\ H_1(\frac{x}{\Delta x} - i + 3 - k). \tag{A.6}$$

The relation (A.4) between the function values and the derivatives in this case leads to:

$$\begin{aligned} F_1^{'} + 4F_2^{'} + F_3^{'} &= 3(\Delta x)^{-1}(F_3 - F_1), \\ F_2^{'} + 4F_3^{'} + F_4^{'} &= 3(\Delta x)^{-1}(F_4 - F_2). \end{aligned} \tag{A.7}$$

A linear extrapolation of the interior values gives the expressions for the boundary values:

$$\begin{aligned} F_1^{'} &= 2F_2^{'} - F_3^{'}, \\ F_4^{'} &= 2F_3^{'} - F_2^{'}. \end{aligned} \tag{A.8}$$

The derivatives $F^{'}$ now can be expressed by:

$$F_k^{'} = G_{kl}\ F_l = \frac{1}{2\Delta x} \begin{pmatrix} -2 & 1 & 2 & -1 \\ -1 & 0 & 1 & 0 \\ 0 & -1 & 0 & 1 \\ 1 & -2 & -1 & 2 \end{pmatrix} F_l. \tag{A.9}$$

By applying equation (A.9) the Hermite interpolation can be rewritten as follows:

$$f(x) = \sum_{k=1}^{4} F_k H(\frac{x}{\Delta x} - i + 3 - k) + \sum_{l=1}^{4} G_{kl} F_l \Delta x \; H_1(\frac{x}{\Delta x} - i + 3 - k). \tag{A.10}$$

The Cardinal spline function is derived by the substitution $y = (\Delta x)^{-1}\; x - i + 3$ and by changing the order of summation:

$$f(x) = \sum_{l=1}^{4} F_l C_l(y). \tag{A.11}$$

To obtained the corresponding derivatives Thomson and Gubbins (1982) suggest an equivalent procedure as for the function values. Here, the derivatives of the Cardinal splines are used. Thus, we have to calculate the derivatives of the functions H and H_1:

$$H^{'}(x) = \begin{cases} -6x^2 - 6x & \text{falls} \quad -1 \leq x \leq 0, \\ 6x^2 - 6x & \text{falls} \quad 0 \leq x \leq 1, \\ 0 & \text{sonst}, \end{cases} \tag{A.12}$$

and

$$H_1^{'}(x) = \begin{cases} 3x^2 + 4x + 1 & \text{falls} \quad -1 \leq x \leq 0, \\ 3x^2 - 4x + 1 & \text{falls} \quad 0 \leq x \leq 1, \\ 0 & \text{sonst}. \end{cases} \tag{A.13}$$

Similar to (A.11) the derivative of $f(x)$ can be calculated by

$$f^{'}(x) = \sum_{l=1}^{4} F_l C_l^{'}(y), \tag{A.14}$$

with the “Cardinal Splines” given by:

$$C_l^{'}(y) = H^{'}(y-l) + \Delta x \sum_{k=1}^{4} G_{kl} H_1^{'}(y-k); \quad l = 1, 2, 3, 4. \tag{A.15}$$

Equation (A.14) shows that no derivatives at grid points have to be stored, since only the function values are used for the interpolation.

Appendix B

Graphical user interface

To run the program of wavefront-oriented ray tracing for anisotropic media a graphical user interfacewas designed. The user interfacewas programmed in Perl Tk and the preparatory work was achieved by the diploma student Jan Dettmer at the University of Hamburg. His work included the development of a graphical user interfacefor the 2-D and 3-D wavefront-oriented ray tracing for isotropic media. This was the foundation for the interface, which is presented in this appendix.
The wavefront-oriented ray-tracing user interfaceis divided in several parts. The "input" sections includes the representation of the model and the definition of the source location. The "run" section comprises all information to solve the kinematic ray-tracing system and the output quantities. The last two parts are designed for the visualisation and a first quality check of the calculated traveltime table.

"Model"

The first decision the user has to make, is what kind of model he wants to calculate (see Figure B.1).

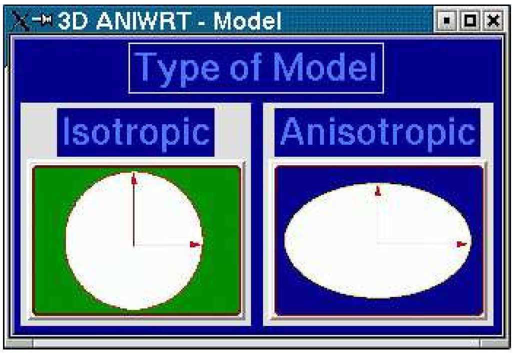

Figure B.1: The user interfaceworks for both types of models, isotropic and anisotropic media, which requires two sub-interfaces necessary.

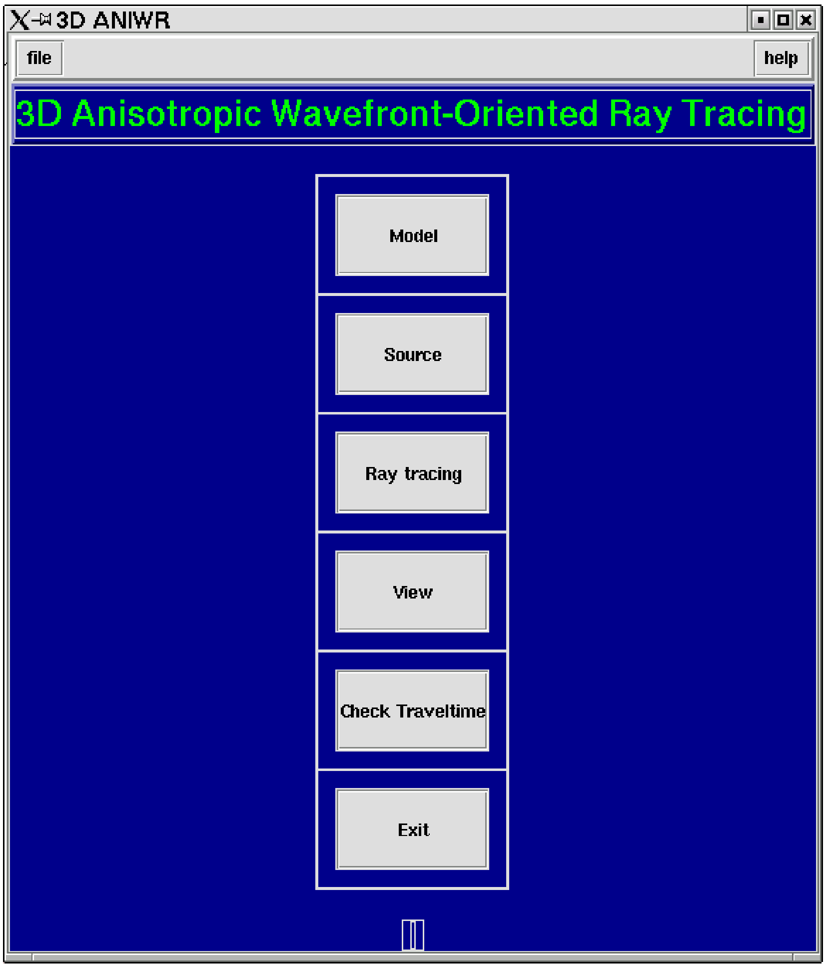

Figure B.2: The figure shows the main menu of the interface. The input sections “model” and “source”, include the model representation, i.e. in terms of the velocities or elastic parameters and the source location. All informations necessary to solve the KRT system are defined in the “run” section. The last two menu items comprehend the visualisation and a first quality check of the calculated traveltimes.

For each model type the user interface has a different appearance. In the isotropic case the velocities at grid points, the number of grid points and the distance between grid points are needed (see Figure B.3).
The program expects an anisotropic model in one of the three following forms (see Figure B.3):

- **homogeneous**: here only the 21 elastic parameters have to be defined.
- **inhomogeneous**: the discretized model with all individual elastic parameters is stored in a file
- **factorised**: the 21 elastic parameters and the 3-D factor-field have to be defined.

The density can be constant for all grid points or a user-defined density field can be used. As for the isotropic case the number of grid points and the distances between them have to be given.

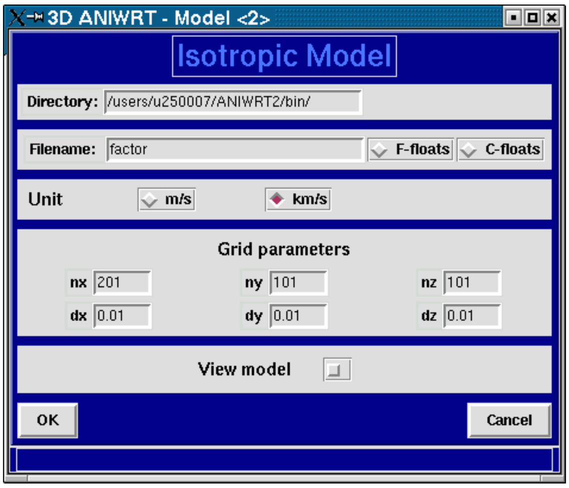

Directory: /users/u250007/ANIWRT2/bin/
Filename: factor ○ F-floats ○ C-floats
Unit ○ m/s ● km/s
nx 201 ny 101 nz 101
dx 0.01 dy 0.01 dz 0.01
View model ☐

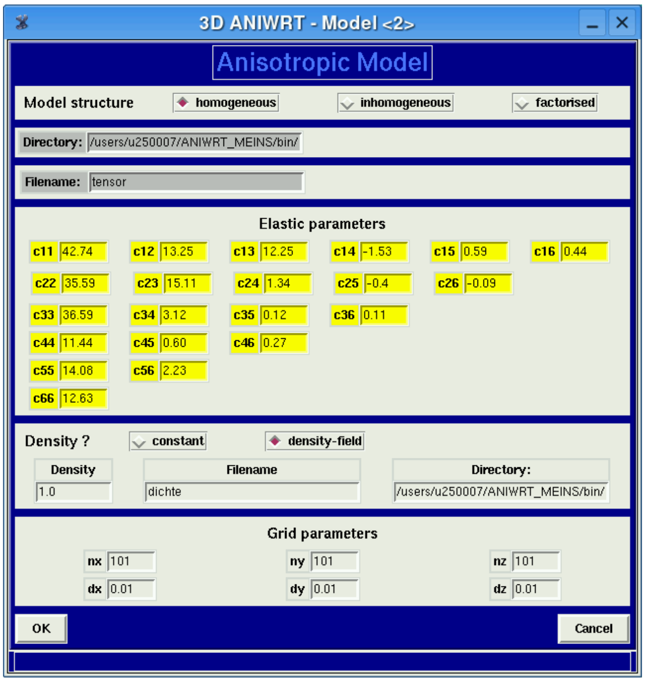

Model structure ● homogeneous ○ inhomogeneous ○ factorised
Directory: /users/u250007/ANIWRT_MEINS/bin/
Filename: tensor

c11 42.74 c12 13.25 c13 12.25 c14 -1.53 c15 0.59 c16 0.44
c22 35.59 c23 15.11 c24 1.34 c25 -0.4 c26 -0.09
c33 36.59 c34 3.12 c35 0.12 c36 0.11
c44 11.44 c45 0.60 c46 0.27
c55 14.08 c56 2.23
c66 12.63

Density ? ○ constant ● density-field
Density 1.0
Filename dichte
Directory: /users/u250007/ANIWRT_MEINS/bin/
nx 101 ny 101 nz 101
dx 0.01 dy 0.01 dz 0.01

Figure B.3: The sub-menus for both types of model, a more detailed description is given in the text.

“Source”

For some applications, e.g., migration, traveltimes for many source receiver combinations are needed. In the user interface three arrangements of source positions are available:

- **Single shot**: only one source location will be calculated.
- **Equidistant sources**: traveltimes for a number of sources with equidistant spacing will be determined.
- **Arbitrary source locations**: defined in an input-file.

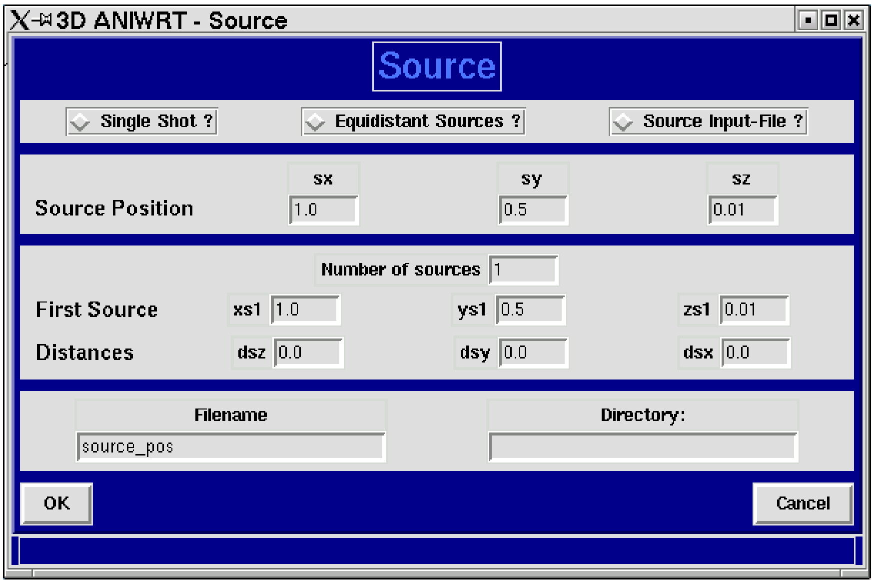

Source Position sx 1.0 sy 0.5 sz 0.01

Number of sources 1

First Source xs1 1.0 ys1 0.5 zs1 0.01

Distances dsz 0.0 dsy 0.0 dsx 0.0

Filename source_pos

Directory:

Figure B.4: In one run it is possible to calculate traveltimes for a number of source positions. In this input user interface the arrangement and the number of sources have to be specified.

“Ray tracing”

The time step for the Runge-Kutta method is preassigned by the “traveltime step” (see section 4.4). In contrast the parameter “draw wavefront”, specifies the time step after which all quantities, e.g., traveltimes at grid points, are calculated and stored. The insertion criteria are controlled by the parameters “maximum traveltime error” and the “maximum distance” between rays.

To control the spacing of the output grid the user interface provides two possibilities: a constant scaling factor with respect to the input grid or the explicit definition of the distances between grid points.

For some applications, e.g., Kirchhoff migration the traveltimes are required only in a restricted target zone. Thus, the target zone can be selected by “interpolation area”.

The implementation calculates multi-arrival traveltimes. The number of arrivals can be

selected by the user. Not only traveltimes, but also the components of slowness at the source or at each image point can be stored after running the program.
Additionally, the program allows to store, e.g. the wavefronts themselves or the ray cells, these are information for the visualisation of the propagating wave.

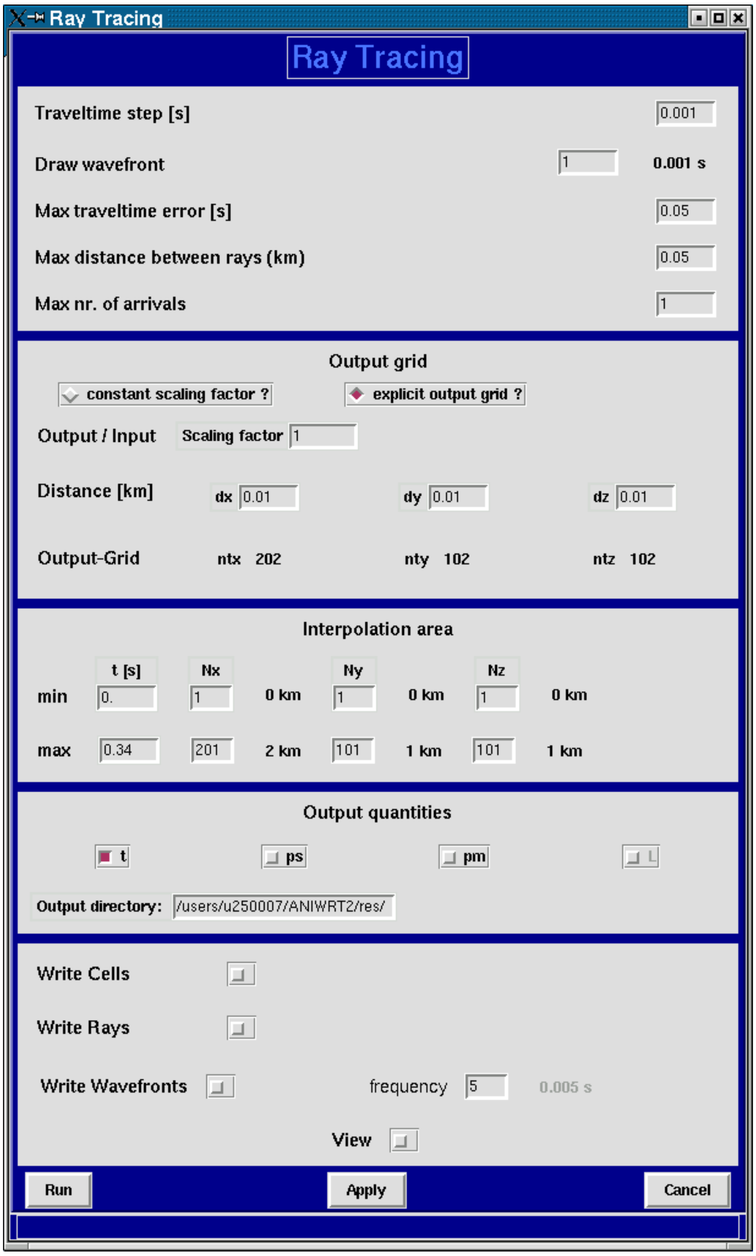

Ray Tracing

Traveltime step [s] 0.001

Draw wavefront 1 0.001 s

Max traveltime error [s] 0.05

Max distance between rays (km) 0.05

Max nr. of arrivals 1

Output grid

○ constant scaling factor ? ● explicit output grid ?

Output / Input Scaling factor 1

Distance [km] dx 0.01 dy 0.01 dz 0.01

Output-Grid ntx 202 nty 102 ntz 102

Interpolation area

	t [s]	Nx		Ny		Nz	
min	0.	1	0 km	1	0 km	1	0 km
max	0.34	201	2 km	101	1 km	101	1 km

Output quantities

☒ t ☐ ps ☐ pm ☐ L

Output directory: /users/u250007/ANIWRT2/res/

Write Cells ☐

Write Rays ☐

Write Wavefronts ☐ frequency 5 0.005 s

View ☐

Figure B.5: This user interface includes all information for the intrinsic ray tracing and the information about the output quantities.

"View" and quality check

The menu item "view" allows the visualisation of a 2-D slice (in x,z) of the calculated traveltimes through the 3-D model (see Figure B.6).

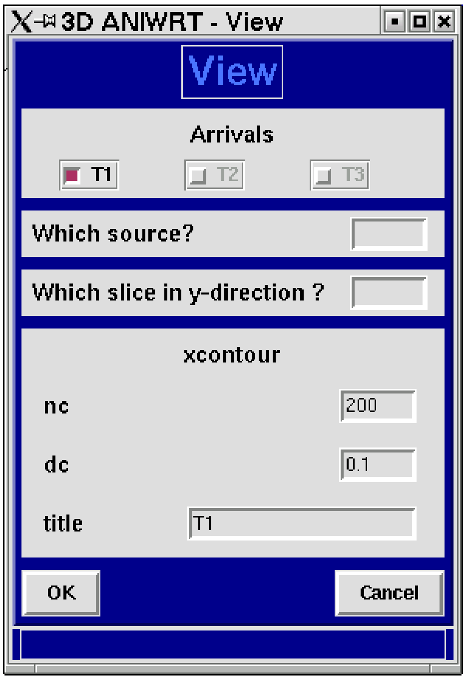

Which source?

Which slice in y-direction ?

xcontour

nc 200

dc 0.1

title T1

Figure B.6: This user interface manages a 2-D visualisation of the results.

If the traveltime tables are intended to be used for, e.g. migration, the applications need traveltime tables where all grid points are determined. If the calculation of traveltimes fails at more than a few (more than five associated points excepting the boundary region) grid points, the input quantities for the ray tracing should be chosen accordingly or maybe the input model is not smooth enough. Both makes a new run of the wavefront-oriented ray tracing necessary. If only isolated grid points are not computed, an interpolation of the missed values is recommended Vanelle (2005). The "check traveltime" user interface starts an external program, that searches in the calculated traveltime tables for empty points.

Appendix C

Elliptical anisotropy

For elliptically anisotropic media most quantities can be calculated analytically. Thus, in this work, this type of medium is used to verify the accuracy of e.g. traveltimes. The aim of this appendix is to summarise the basic formulas for the elliptically anisotropic case. A more detailed description can be found in Vanelle (2002b).

For a medium with elliptical anisotropy and a vertical symmetry axis the matrix of the density-normalised elastic parameters ($A_{pq} = C_{pq}/\rho$) has the following form:

$$A_{pq} = \begin{pmatrix} A_{11} & A_{12} & A_{13} & & & \\ & A_{11} & A_{13} & & & \\ & & A_{33} & & & \\ & & & A_{44} & & \\ & & & & A_{44} & \\ & & & & & A_{66} \end{pmatrix}, \tag{C.1}$$

with the additional constraints:

$$\begin{aligned} A_{12} &= A_{11} - 2A_{66} \\ (A_{13} + A_{44})^2 &= (A_{11} - A_{44})(A_{33} - A_{44}). \end{aligned} \tag{C.2}$$

A basic role in the ray method in anisotropic media play the 3 × 3 Christoffel matrix $\Gamma_{ik} = a_{ijkl} p_j p_l$, where $a_{ijkl} = c_{ijkl}/\rho$. The solution of the Christoffel equation,

$$(\Gamma_{ik} - G_m \delta_{ik}) g_k^{(m)} = 0, \quad m = 1, 2, 3, \tag{C.3}$$

where δ_{ik} is the Kronecker symbol, requires

$$|\Gamma_{ik} - G_m \delta_{ik}| = 0, \quad m = 1, 2, 3. \tag{C.4}$$

This determinant leads to the characteristic polynomial of third order, whose three solutions are the eigenvalues $G_m = 1$. The index m specifies the type of elementary wave under consideration. Since the matrix A_{pq} displays rotational symmetry with respect to the vertical axis, the slowness $\vec{p}$

$$\vec{p} = \frac{\vec{n}}{V^{(m)}}, \tag{C.5}$$

can be chosen in the way that $p_y = 0$. By defining the normal vector $\vec{n}$

$$\vec{n} = \left(\sin\phi^{(m)},\ 0,\ \cos\phi^{(m)}\right), \tag{C.6}$$

the slowness vector $\vec{p}$ is given by:

$$\vec{p} = \left(\frac{\sin\phi^{(m)}}{V^{(m)}},\ 0,\ \frac{\cos\phi^{(m)}}{V^{(m)}}\right), \tag{C.7}$$

where ϕ is the phase angle made by $\vec{p}$ and the vertical axis, and $V^{(m)}$ is the phase velocity for direction ϕ. The insertion of the elliptical elastic elements (C.2) into the formula of the Christoffel matrix (2.11) leads to:

$$\begin{aligned}
\Gamma_{11} &= A_{11}p_1^2 + A_{44}p_3^2 = A_{11}\frac{\sin^2\phi^{(m)}}{(V^{(m)})^2} + A_{44}\frac{\cos^2\phi^{(m)}}{(V^{(m)})^2},\\
\Gamma_{22} &= A_{66}p_1^2 + A_{44}p_3^2 = A_{66}\frac{\sin^2\phi^{(m)}}{(V^{(m)})^2} + A_{44}\frac{\cos^2\phi^{(m)}}{(V^{(m)})^2},\\
\Gamma_{33} &= A_{44}p_1^2 + A_{33}p_3^2 = A_{44}\frac{\sin^2\phi^{(m)}}{(V^{(m)})^2} + A_{33}\frac{\cos^2\phi^{(m)}}{(V^{(m)})^2},\\
\Gamma_{13} &= (A_{13} + A_{44})p_1p_3 = \sqrt{(A_{11} - A_{44})(A_{33} - A_{44})}\,\frac{\sin\phi^{(m)}\cos\phi^{(m)}}{(V(m))^2}.
\end{aligned} \tag{C.8}$$

Insertion of the Christoffel matrix (C.8) for the elliptical case into the characteristic polynomial (C.4) yields three **phase velocities** $V^{(m)}$:

$$\begin{aligned}
V^{qSV} &= \sqrt{A_{44}},\\
V^{SH} &= \sqrt{A_{66}\sin^2\phi^{SH} + A_{44}\cos^2\phi^{SH}},\\
V^{qP} &= \sqrt{A_{11}\sin^2\phi^{qP} + A_{33}\cos^2\phi^{qP}}.
\end{aligned} \tag{C.9}$$

The components of the eigenvector $g_k^{(m)}$ of the Christoffel matrix Γ can be obtained as the solutions of the equations:

$$\Gamma_{ik}g_i^{(m)}g_k^{(m)} = 1. \tag{C.10}$$

By using the abbreviations $n^{(m)}$ and $l^{(m)}$

$$\begin{aligned}
l^{(m)} &= \sqrt{\frac{A_{11} - A_{44}}{(A_{11} - A_{44})\sin^2\phi^{(m)} + (A_{33} - A_{44})\cos^2\phi^{(m)}}},\\
n^{(m)} &= \sqrt{\frac{A_{33} - A_{44}}{(A_{11} - A_{44})\sin^2\phi^{(m)} + (A_{33} - A_{44})\cos^2\phi^{(m)}}},
\end{aligned} \tag{C.11}$$

the polarisations for the elliptical case are given by:

$$\begin{aligned}\vec{g}^{\,qSV} &= (n^{qSV}\cos\phi^{qSV}, 0, -l^{qSV}\sin\phi^{\phi^{qSV}}),\\ \vec{g}^{\,SH} &= (0,1,0),\\ \vec{g}^{\,qP} &= (l^{qP}\sin\phi^{qP}, 0, m^{qP}\cos\phi^{\phi^{qP}}).\end{aligned} \tag{C.12}$$

The ray velocity vector $v_i^{(m)}$ determines the direction and speed of energy propagation, and is therefore of primary importance in seismic traveltime modelling and inversion methods. As illustrated by the sketch in Figure C.1, the group velocity vector in a homogeneous medium is aligned with the source-receiver direction (angle θ), while the phase velocity (or slowness) vector is orthogonal to the wavefront (angle ϕ).

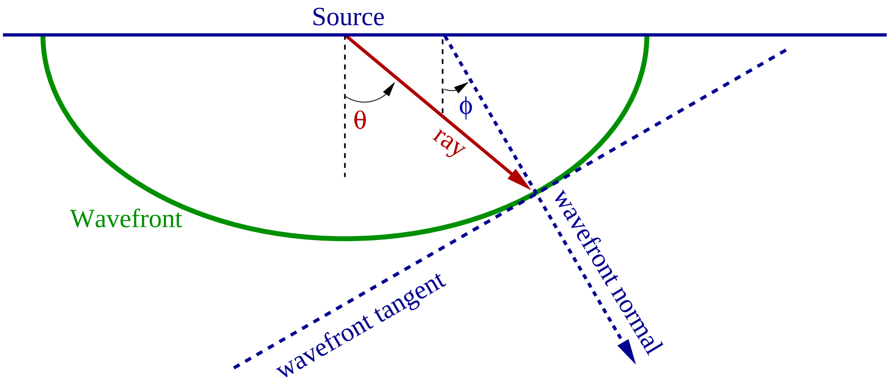

Figure C.1: Wavefront in a homogeneous model with elliptical symmetry with the associated angles. The ray angle is denoted by θ, and ϕ is the phase angle.

The three components of the ray velocity vector are given by:

$$v_i^{(m)} = a_{ijkl} g_j^{(m)} g_k^{(m)} p_l. \tag{C.13}$$

For the elliptically anisotropic media the relation (C.13) leads to:

$$\begin{aligned}\vec{v}^{\,qSV} &= \left(\sqrt{A_{44}}\sin\phi^{qSV}, 0, \sqrt{A_{44}}\cos\phi^{qSV}\right),\\ \vec{v}^{\,SH} &= \left(\frac{A_{66}}{V^{SH}}\sin\phi^{SH}, 0, \frac{A_{44}}{V^{SH}}\cos\phi^{SH}\right),\\ \vec{v}^{\,qP} &= \left(\frac{A_{11}}{V^{qP}}\sin\phi^{qP}, 0, \frac{A_{33}}{V^{qP}}\cos\phi^{qP}\right).\end{aligned} \tag{C.14}$$

Introducing the ray angle $\theta^{(m)}$ (see Figure C.1) the **ray velocities** can be described as:

$$\begin{aligned}
v^{qSV} &= \sqrt{A_{44}} & &= V^{qSV}, \\
v^{SH} &= \sqrt{\frac{A_{66}^2 \sin^2\phi^{SH} + A_{44}\cos^2\phi^{SH}}{V^{SH}}} & &= \left[\frac{\sin^2\theta^{SH}}{A_{66}} + \frac{\cos^2\theta^{SH}}{A_{44}}\right]^{-\frac{1}{2}}, \\
v^{qP} &= \sqrt{\frac{A_{11}\sin^2\phi^{qP} + A_{33}\cos^2\phi^{qP}}{V^{qP}}} & &= \left[\frac{\sin^2\theta^{qP}}{A_{11}} + \frac{\cos^2\theta^{qP}}{A_{33}}\right]^{-\frac{1}{2}}.
\end{aligned} \tag{C.15}$$

Considering a homogeneous elliptical medium, the traveltime can be calculated analytically. The vector $\vec{r} = (x, y, z) = (g_x - s_x, g_y - s_y, g_z - s_z)$ describes the distance between source and receiver positions, and its modulus is $r = \sqrt{x^2 + y^2 + z^2}$. The traveltime $\tau^{(m)}$ of the wave type m propagating from the source to the receiver is given by Daley and Hron (1979):

$$\tau^{(m)} = \sqrt{\frac{x^2}{\left(v_x^{(m)}\right)^2} + \frac{y^2}{\left(v_x^{(m)}\right)^2} + \frac{z^2}{\left(v_z^{(m)}\right)^2}}. \tag{C.16}$$

The velocity $v_z^{(m)}$ is the ray velocity of a wave traveling in z direction, and $v_x^{(m)}$ describes the ray velocity of a wave traveling in the x-y plane, since the medium shows rotational symmetry with respect to the z axis. In the case of a qSV-wave the velocities are equal:

$$v_x^{qSV} = v_z^{qSV} = \sqrt{A_{44}}. \tag{C.17}$$

For a SH wave the velocities are:

$$v_x^{SH} = \sqrt{A_{66}} \quad \text{and} \quad v_z^{SH} = \sqrt{A_{44}}. \tag{C.18}$$

For a qP-wave they are given by:

$$v_x^{qP} = \sqrt{A_{11}} \quad \text{and} \quad v_z^{qP} = \sqrt{A_{33}}. \tag{C.19}$$

This results in the following traveltimes:

$$\begin{aligned}
\tau^{qSV} &= \sqrt{\frac{x^2 + y^2 + z^2}{A_{44}}}, \\
\tau^{SH} &= \sqrt{\frac{x^2 + y^2}{A_{66}} + \frac{z^2}{A_{44}}}, \\
\tau^{qP} &= \sqrt{\frac{x^2 + y^2}{A_{11}} + \frac{z^2}{A_{33}}},
\end{aligned} \tag{C.20}$$

In section 7.4, the accuracy of the coefficients for the hyperbolic traveltime interpolation (see section 7.1) are tested. The components of the slowness $\vec{p}$ at for the elliptically anisotropic homogeneous model are needed (Vanelle, 2002a):

$$\begin{aligned}
p_{x0}^{(m)} &= q_{x0} = \frac{x}{\left(v_x^{(m)}\right)^2 \tau^{(m)}}, \\
p_{y0}^{(m)} &= q_{y0} = \frac{y}{\left(v_x^{(m)}\right)^2 \tau^{(m)}}, \\
p_{z0}^{(m)} &= q_{z0} = \frac{z}{\left(v_z^{(m)}\right)^2 \tau^{(m)}}.
\end{aligned} \tag{C.21}$$

Also the coefficients, which are given by the second-order derivatives (7.3) can be calculated analytically for the homogeneous case:

$$\begin{aligned}
-S_{xx} = G_{xx} = N_{xx} &= \frac{\left(v_x^{(m)}\right)^2 \left(\tau^{(m)}\right)^2 - x^2}{\left(v_x^{(m)}\right)^4 \left(\tau^{(m)}\right)^3}, \\
-S_{yy} = G_{yy} = N_{yy} &= \frac{\left(v_x^{(m)}\right)^2 \left(\tau^{(m)}\right)^2 - y^2}{\left(v_x^{(m)}\right)^4 \left(\tau^{(m)}\right)^3}, \\
-S_{zz} = G_{zz} = N_{zz} &= \frac{\left(v_z^{(m)}\right)^2 \left(\tau^{(m)}\right)^2 - z^2}{\left(v_z^{(m)}\right)^4 \left(\tau^{(m)}\right)^3}, \\
-S_{xy} = G_{xy} = N_{xy} = N_{yx} &= -\frac{xy}{\left(v_x^{(m)}\right)^4 \left(\tau^{(m)}\right)^3}, \\
-S_{yz} = G_{yz} = N_{yz} = N_{zy} &= -\frac{yz}{\left(v_x^{(m)}\right)^2 \left(v_z^{(m)}\right)^2 \left(\tau^{(m)}\right)^3}, \\
-S_{zx} = G_{zx} = N_{zx} = N_{xz} &= -\frac{zx}{\left(v_z^{(m)}\right)^2 \left(v_x^{(m)}\right)^2 \left(\tau^{(m)}\right)^3}.
\end{aligned} \tag{C.22}$$

Appendix D

Hyperbolic coefficients for the irregular grid configuration

In this appendix the remaining coefficients which are needed for the traveltime-based migration in the angle domain are given. In comparison to the coefficients for regular grids Vanelle and Gajewski (2002a), here the source is at the image point in the subsurface and the receivers are located at the surface (see also Figure D.1). For simplicity only a 3-D situation is considered, where we have no variations in the third (y) direction. In this case the following coefficients are needed:

q_x	horizontal slowness at the receiver,
G_{xx}	second-order traveltime derivative at the receiver,
p_x p_z	horizontal and vertical slowness at the image point,
S_{xx}, S_{zz} S_{xz}	second-order traveltime derivative at the image point,
N_{xx}, N_{zx}	second-order mixed traveltime derivative,
$\sigma = N_{yy}^{-2}$	for the computation of the out-of-plane spreading.

The coefficients q_x and G_{xx} are given by:

$$\begin{aligned} q_x &= \frac{T_p^2 \Delta g_m^2 - T_m^2 \Delta g_p^2 - T_0^2(\Delta g_m^2 - \Delta g_p^2)}{2T_0(\Delta g_m^2 \Delta g_p + \Delta g_m \Delta g_p^2)}, \\ G_{xx} &= \frac{T_m^2 \Delta g_p + T_p^2 \Delta g_m - T_0^2(\Delta g_m + \Delta g_p)}{T_0(\Delta g_m^2 \Delta g_p + \Delta g_m \Delta g_p^2)} + \frac{q_x^2}{T_0}. \end{aligned} \tag{D.1}$$

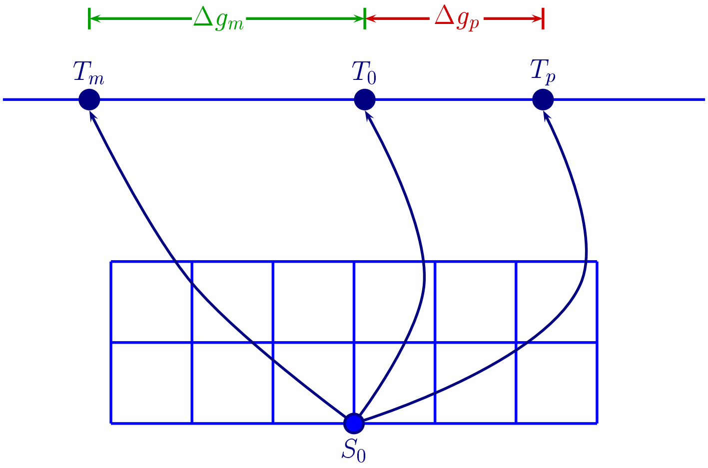

Figure D.1: Determination of the slowness at the receiver q_x and the second-derivative G_{xx}: the traveltimes T_0 from $\vec{s}_0$ and $\vec{g}_0$, T_m from $\vec{s}_0$ and $\vec{g}_0 - \Delta g_m$ and T_p from $\vec{s}_0$ and $\vec{g}_0 + \Delta g_p$.

The slowness p_x, p_z and the second derivatives S_{xx}, S_{zz} and S_{xz} at the image points are given by:

$$\begin{aligned}
p_x &= \frac{(T^{mo})^2 - (T^{po})^2}{4T_0 \Delta s_x}, \\
p_z &= \frac{(T^{om})^2 - (T^{op})^2}{4T_0 \Delta s_z}, \\
S_{xx} &= \frac{2T_0^2 - (T^{po})^2 - (T^{mo})^2}{4T_0 (\Delta s_x)^2} - \frac{p_x^2}{T_0}, \\
S_{zz} &= \frac{2T_0^2 - (T^{op})^2 - (T^{om})^2}{4T_0 (\Delta s_z)^2} - \frac{p_z^2}{T_0}, \\
S_{xz} &= \frac{(T^{mm})^2 + (T^{pp})^2 - (T^{pm})^2 - (T^{mp})^2}{8T_0 \Delta s_x \Delta s_z} - \frac{p_x p_z}{T_0},
\end{aligned} \tag{D.2}$$

For example, to determine the coefficients p_x and S_{xx} corresponding to the source-receiver combination g_0 and s_0 the three traveltimes T^{mo}, T_0 and T^{po} are needed (see Figure D.2). After the ray shooting from the three subsurface points s_{mo}, s_0 and s_{po}, however, the traveltimes T_0^{mo}, T_0 and T_0^{po} are known (see left side in Figure D.3). Using these traveltimes and applying the hyperbolic traveltime interpolation leads to the remaining traveltimes.

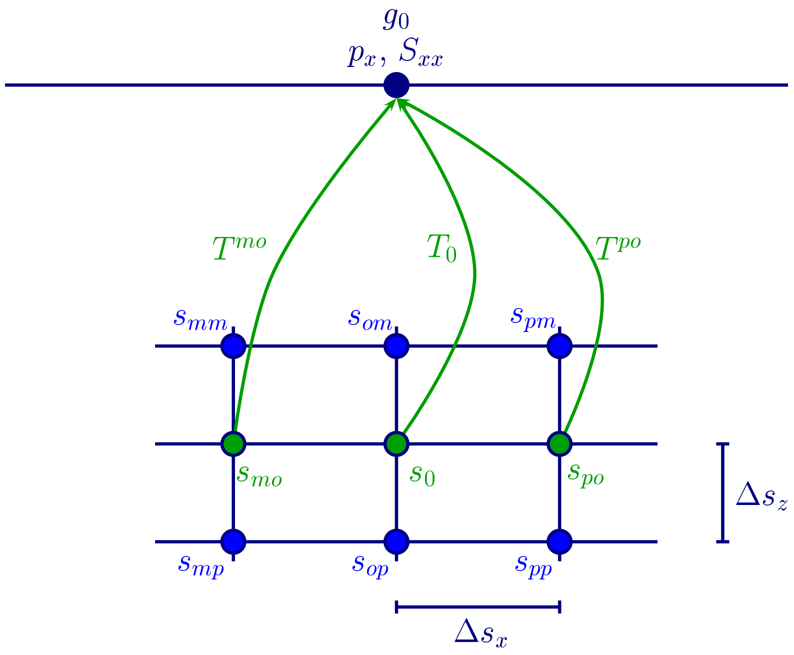

Figure D.2: Determination of the slowness p_x and the second-derivative S_{xx} at the image point s_0: the traveltimes T_0 from $\vec{s}_0$ and $\vec{g}_0$, T^{mo} from s_{mo} to $\vec{g}_0$ and T^{po} from s_{po} and $\vec{g}_0$.

The traveltimes T^{po}, T^{mo}, T^{pm}, T^{mp}, T^{mm}, T^{pp}, T^{op} and T^{om} are calculated by

$$\begin{aligned}
(T^{mo})^2 &= (T_0^{mo} - q_{mo}\Delta g_{mo})^2 + T_0^{mo} G_{mo} \Delta g_{mo}^2, \\
(T^{po})^2 &= (T_0^{po} + q_{po}\Delta g_{po})^2 + T_0^{po} G_{po} \Delta g_{po}^2, \\
(T^{om})^2 &= (T_0^{om} - q_{om}\Delta g_{om})^2 + T_0^{om} G_{om} \Delta g_{om}^2, \\
(T^{po})^2 &= (T_0^{op} + q_{op}\Delta g_{op})^2 + T_0^{op} G_{op} \Delta g_{op}^2, \\
(T^{mp})^2 &= (T_0^{mp} - q_{mp}\Delta g_{mp})^2 + T_0^{mp} G_{mp} \Delta g_{mp}^2, \\
(T^{pm})^2 &= (T_0^{pm} + q_{pm}\Delta g_{pm})^2 + T_0^{pm} G_{pm} \Delta g_{pm}^2, \\
(T^{mm})^2 &= (T_0^{mm} - q_{mm}\Delta g_{mm})^2 + T_0^{mm} G_{mm} \Delta g_{mm}^2, \\
(T^{pp})^2 &= (T_0^{pp} + q_{pp}\Delta g_{pp})^2 + T_0^{pp} G_{pp} \Delta g_{pp}^2,
\end{aligned} \tag{D.3}$$

where the coefficient q_{ij} and G_{ij} $(i,\ j = 1, 2)$ correspond to the source-receiver pair (g_{ij}, s_{ij}) and Δg_{ij} defines to the distance to the expansion point g_0 ($\Delta g_{ij} = g_0 - g_{ij}$).

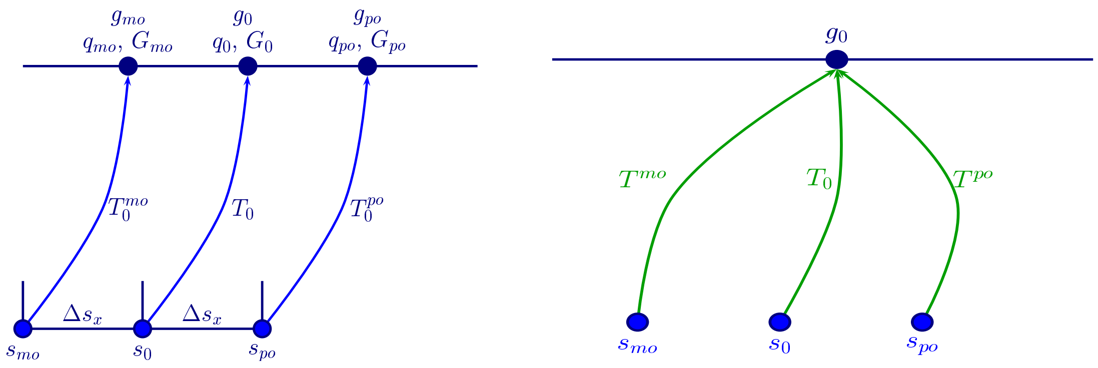

Figure D.3: In the first step rays are shot from each subsurface point s_{mo}, s_0 and s_{po} (left side) to the surface. The corresponding traveltimes are given by T_0^{mo}, T_0 and T_0^{po}. To obtain the traveltimes T^{mo}, T_0 and T^{po} in the second step the hyperbolic traveltime interpolation is applied.

The second-order mixed derivative matrix elements, N_{xx} and N_{zx}, are:

$$\begin{aligned} N_{xx} &= \frac{(T^{mp})^2 + (T^{pm})^2 - (T^{pp})^2 - (T^{mm})^2}{4T_0 \Delta s_x (\Delta g_m + \Delta g_p)} - \frac{q_x p_x}{T_0}, \\ N_{zx} &= \frac{(T^{pm})^2 + (T^{mp})^2 - (T^{pp})^2 - (T^{mm})^2}{4T_0 \Delta s_z (\Delta g_m + \Delta g_p)} - \frac{q_x p_z}{T_0}, \end{aligned} \tag{D.4}$$

Acknowledgments

Prof. Dr. Dirk Gajewski danke ich für die interessante Aufgabenstellung und die von ihm gewährten Freiheiten in Bezug auf meine Forschungsarbeit.

Für die lehrreichen Diskussionen, die Übernahme des Korreferats und die unerschöpfliche Hilfsbereitschaft mit dem unbekanntem Wesen Computer danke ich **Dr. Ekkehart Tessmer** .

Dr. Claudia Vanelle danke ich für das Korrekturlesen, die fruchtbaren fachlichen Diskussionen und die anregenden Gespräche über Gott und die Welt.

Diese Arbeit profitiert zu grossen Teilen von bereits geleisteten Arbeiten von **Dr. Radu Coman**, dessen Hilfe bei den Tücken der Umsetzung theoretischer Überlegungen äusserst wertvoll war.

Für die Bereitstellung von Vergleichslaufzeiten und ihrer Hilfe beim allgemeinen Verständnis des Phänomens Anisotropie danke ich **Dr. Svetlana Golovnina**.

Ich danke **Jan Dettmer**, daßich seine graphische Benutzeroberfläche im Sinne der Anisotropie verkomplizieren durfte.

Bedanken möchte ich mich ebenfalls bei **Dr. Einar Iversen** für die interessanten fachlichen Gespräche.

Für ihre herzlichen Aufmunterungen und ihre Hilfsbereitschaft, möchte ich **Christel Mynarik**, der “Guten Seele” des geophysikalischen Instituts, danken.

Ich danke der Deutsche Forschungsgesellschaft und den Sponsoren des Wave Inversion Technology (WIT) Konsortiums, die diese Arbeit finanziell unterstützt haben.

Für die freundschaftliche und produktive Atmosphäre danke ich allen Mitarbeitern des Instituts für Geophysik. Besonders hervorheben möchte ich:.

Gesa Netzeband heutzutage wäre es mir eine Ehre mit Dir eine $5m^2$ Kajüte zu teilen!

Stefan Dümmong darf hier natürlich nicht unerwähnt bleiben. Was wäre ein Tag ohne die Suche nach dem perfektem Tagescredo oder dem pausefüllendem sarkasmus-geprägtem Geplänkel.

Dr. Daniela Kühn danke ich für die Hilfsbereitschaft, die Gastfreundschaft in Norwegen und dafür, dass wir Freunde werden konnten.

Dr. Elive Menyoli danke ich für sein sonniges Gemüt!

Martin Bak-Hansen: Danke!

Ebenfalls bedanken möchte ich mich bei **Axel Ehrhardt**, der es mit mir in einem Büro ausgehalten hat.

Dr. Mi-Kyung Yoon danke ich für ihr sorgfälltiges Korrekturlesen einiger Teile dieser

Arbeit.
Und da es auch noch ein Leben ausserhalb der Geophysik gibt, möchte ich an dieser Stelle auch noch folgenden Personen danken:
Binaca von Scheidt und Dr. Thorsten Prüstel die besten Freunde der Welt.
Maximilian Krüger, der mich mein gesamtes Studium begleitet und mich und mein Leben außerordentlich geprägt hat.
Brigitte, Laura und Jan möchte ich hier ebenfalls erwähnen, denn ohne familiäre Unterstützung wäre weder Studium noch Doktorarbeit möglich gewesen.

Schließlich möchte ich mich bei meinem lieben Freund **Malte Vöge** bedanken, dessen Geduld des öfteren auf eine harte Probe gestellt wurde.